UNIVERSITÀ DELLA CALABRIA

**UNIVERSITA' DELLA CALABRIA**

Dipartimento di Fisica

**Dottorato di Ricerca in**

SCIENZE E TECNOLOGIE FISICHE, CHIMICHE E DEI MATERIALI

**CICLO**

XXIX

**TITOLO TESI**

***MATERIALS AND PROCESSES FOR ORGANIC PHOTOVOLTAIC DEVICES***

**Settore Scientifico Disciplinare** CHIM/02

**Coordinatore:** Ch.mo Prof. Vincenzo Carbone

Firma Vincenzo Carbone

**Supervisore/Tutor**: Ch.mo Prof. Attilio Golemme

Firma Attilio Golemme

**Dottorando**: Dott.ssa Raffaella Lento

Firma Raffaella Lento

# Contents

# Abstract

Conversion of solar energy into electricity is a promising alternative to the use of conventional energy resources. In this context, organic solar cells (OSCs) can offer an interesting alternative to wafer-sized and inorganic thin films technology, due to the solution and low-temperature processability of organic semiconductors and to the possibility of using flexible substrates. All these features contribute to decrease the costs of production of solar devices, although their power conversion efficiency is still low.

The studies in this thesis intend to investigate several effects on the efficiency of polymeric solar cells. In particular, I focused my attention on a well-studied bulk heterojunction (BHJ) constituted of regio-regular poly(3-hexylthiophene) - P3HT - as a donor and the fullerene soluble derivate [6,6]-Phenyl C61 butyric acid methyl ester - $PC_{60}BM$ - as an acceptor. In this way, the effect of materials, innovative processing and device architecture could be explored for this optimized reference system.

The first part of this dissertation discusses the preparation and characterization of novel electropolymerized and photoconductive thin films of cyclo-metallated complexes, with the aim to employ an intrinsic photoconductor as an anode buffer layer (ABL) between the P3HT:$PC_{60}BM$ active layer and the ITO electrode. A photoconductive compound could represent an appealing alternative to conventional semiconductors due to the improving of its electrical conductivity upon light absorption, *i.e*. during the working condition of a solar cell, for enhancing charge transport to the electrodes. The studied complexes contain Pd(II) or Pt(II) as a metal center, 2-phenylpyridine as cyclo-metallated ligand and a triphenylamino-substituted (TPA) electropolymerizable Shiff base as an ancillary ligand. Optimization of the electro-deposition conditions (on ITO) and studies on dynamics, morphology, stability, photoconducting and hole transport properties on the obtained thin films were conducted. Results on their application as ABL are presented.

The second part of this thesis explores the possibility of exciting plasmonic responses in a multilayer hyperbolic metamaterial (HMM) structure, consisting of alternating layers of BHJ and aluminum. Indeed, one approach for improving the power conversion efficiency in these BHJ solar cells is based on improving the light absorption of the device. Novel HMM plasmonic configurations offer the possibility of engineering the

absorption band of the resulting structure to achieve the desired absorption performances over a broad wavelength range. A complete characterization of the optical properties of the engineered one-bilayer structure is given, together with the analysis of the J-V characteristics curves of the plasmonic solar devices studied. The beneficial contribution of plasmonic designed metal thin layers is evident even with a single BHJ/Al bilayer that shows enhanced conversion performances with respect to the control devices. Preliminary results based on experimental and simulated data on the two-bilayer system are presented.

While working on the photovoltaic applications of HMMs, a series of experimental observations on silver-based HMM were performed, which offered the opportunity to investigate other several interesting phenomena. Ag-based HMMs have been constructed with both BHJ and $TiO_2$ as the dielectric. In the first case, the excitation of the so-called Ferrell-Berreman modes were observed. These modes are characterized by a high absorption at a specific wavelength and could be used in solar cell technology for improving absorption and, thus, efficiency. In the latter case, a specifically conceived dielectric layer based on unsintered $TiO_2$, poly(vinylpyrrolidone) and a dye, led to a thermally-tunable HMM, a highly relevant result for practical applications of HMMs.

# Sintesi

Al giorno d'oggi, i problemi relativi allo sfruttamento delle risorse naturali, dovuto alla dipendenza delle nostre infrastrutture energetiche dai combustibili fossili e dal petrolio, stanno facendo affiorare con sempre più prepotenza la necessità di utilizzare fonti pulite e rinnovabili, come il sole, per la produzione di energia. Tuttavia, la capacità di penetrazione della tecnologia solare nella vita reale ha subito dei limiti, imposti soprattutto dagli elevati costi di produzione dei pannelli attualmente commercializzati. Le celle solari organiche (OSCs) e ibride possono rappresentare un'interessante alternativa (nonostante le loro efficienze di conversione ancora relativamente basse) ai semiconduttori inorganici utilizzati per a produzione di pannelli fotovoltaici (Si, CdTe, CIGS) in quanto offrono la possibilità di abbassare i costi di produzione – grazie a tecniche di processo da soluzione e a bassa temperatura – e di poter essere integrate in sistemi flessibili, garantendo anche così un minor impatto ambientale.

Questo lavoro di tesi si propone di studiare come l'introduzione di diversi materiali, l'utilizzo di tecniche di deposizione elettrochimiche e la variazione nell'architettura del dispositivo, possano influenzare l'efficienza di conversione di celle solari ad eterogiunzione diffusa (BHJ), aventi come strato attivo il sistema donatore/accettore ampiamente studiato in letteratura P3HT:$PC_{60}BM$. In particolare:

Nella prima parte della tesi, viene esplorata la possibilità di utilizzare film polimerici fotoconduttori come materiale trasportatore di buche tra lo strato attivo e l'elettrodo di ITO. Questi film polimerici sono stati ottenuti attraverso polimerizzazione elettrochimica a partire dai corrispondenti monomeri, costituiti da due complessi organometallici contenenti Pd(II) o Pt(II), la 2-fenil-piridina come legante ciclometallante e una base di Shiff contenente l'unità elettropolimerizzabile tri-fenil-ammina, per completare la sfera di coordinazione dei metalli. Dopo aver condotto una procedura di ottimizzazione necessaria ad ottenere spessore e morfologia controllati, questi film sono stati caratterizzati per le loro proprietà di fotoconduzione e di trasporto di buche, prima di essere impiegati nella cella solare standard in sostituzione del PEDOT:PSS, usato come riferimento.

La seconda parte della discussione si propone di sfruttare le caratteristiche ottiche razionalmente progettate in un *metamateriale iperbolico* (HMM) per aumentare

l'assorbimento della radiazione solare a lunghezze d'onda tipiche del vicino IR, in cui i materiali organici solitamente non mostrano assorbimento. In particolare, il HMM proposto è costituito da un'alternanza di layers (con spessori nanometrici) di materiali tipicamente impiegati nella costruzione di celle solari standard quali l'alluminio e la BHJ P3HT:$PC_{60}BM$; in questo modo si vuole verificare se questo diverso tipo di arrangiamento strutturale (avente particolari proprietà di assorbimento non riconducibili ai singoli materiali di cui è composto) possa portare ad un miglioramento nell'efficienza di conversione dell'energia solare. La caratterizzazione completa dal punto di vista ottico ed elettrico è stata condotta per un singolo bilayer iperbolico, mentre verranno presentate le prime simulazioni in supporto alla realizzazione del HMM.

Altri effetti dovuti alla geometria multilayers tipica di un HMM sono stati osservati sperimentalmente in particolari campioni realizzati:

- Nel HMM BHJ/Ag è stato possibile osservare la presenza dei modi di Ferrell-Berreman caratterizzati da un alto assorbimento della radiazione a particolari lunghezze d'onda. Sono in corso esperimenti volti a capire se la luce assorbita grazie alla risonanza di questo tipo di polaritoni di volume possa essere utilizzata per aumentare l'efficienza di celle solari;
- Sfruttando la sensibilità termica di un film sottile di $TiO_2$ (preparato da tecniche in soluzione e non sinterizzato) drogato con PVP e con una Cumarina - TPD -, è stato possibile ottenere un HMM Ag/TPD che avesse proprietà ottiche dipendenti dalla temperatura nel range spettrale del visibile. Questo aspetto innovativo per un HMM è stato analizzato attraverso simulazioni, misure ellissometriche e di caratterizzazione fotofisica.

# CHAPTER 1:
# INTRODUCTION TO PHOTOVOLTAIC AND AIM OF THIS WORK

## 1.1 INTRODUCTION

The energy problem is amongst the biggest challenges of this century. The energy demand, consumption and production are continuously growing, together with the world population (especially in the developing countries) and the living standards in developed countries. (Figures 1.1 and 1.2)

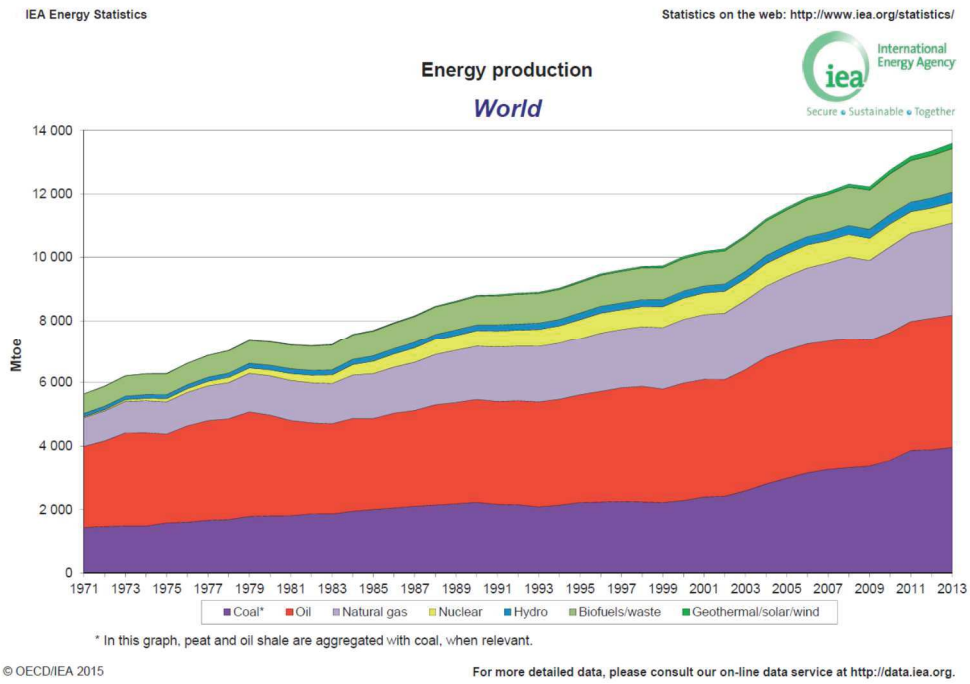


*Figure 1.1- Representation of the World Energy Production over the last forty years.*

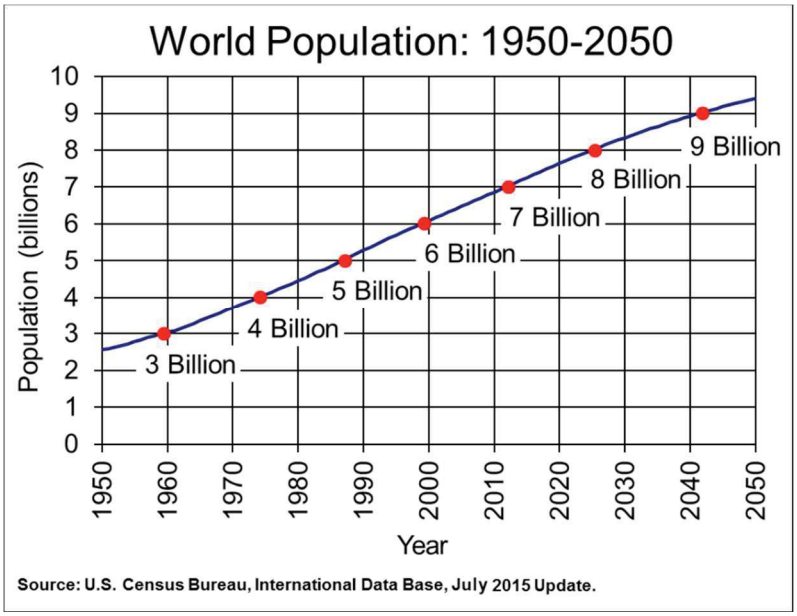


*Figure 1.2- Estimated world population growth.*

At present, our energy infrastructures heavily depend on fossil fuels like oil, coal and natural gas. However, these traditional energy sources are not unlimited and sustainable and their exploitation can have long-term negative results on health and environment, such as those related to the excessive production of $CO_2$, which contributes to the so-called greenhouse effect and to the global warming and climate change. This scenario suggests the urgent need of using alternative approaches for energy production.

As a renewable energy source, solar energy can play a dominant role because it is abundant, environmentally friendly and ideal for distributed power generation and for remote locations. In fact, in spite of its temporal and spatial variability, the sun delivers about 174000 TW of energy to the upper level Earth's atmosphere[1]. This value is reduced to around 1000 $Wm^{-1}$ by atmospheric absorption and scattering but, even so, this energy is thousands of times larger than what needed to meet the world's yearly energy needs. The "PhotoVoltaic effect" (PV), the process through which a material can transform sunlight photons into electricity (*i.e.* mobile charge carriers) was observed for the first time by Alexandre E. Becquerel in 1839[2] with an electrolytic cell. Since then, this effect has been systematically studied, even in solid-state devices, and finally theoretically explained by Einstein in 1921[3]. These findings, together with the development of manufacturing systems for high quality silicon wafers, led to the first efficient (6%) solar device based on silicon[4] in 1954. Since then, we have assisted to huge improvements in the field of (inorganic) PV

technology and, at the same time, to the emerging of new, interesting device concepts based on organic and hybrid materials, leading to the first Organic Solar Cell (OSC), obtained by Tang[5]. In spite of all the progresses in PV technologies, crystalline silicon wafer devices (c-Si)are still leading the market because of their high Power Conversion Efficiency (PCE or η), the abundance of raw materials on earth's crust, the well-understood physical mechanisms involved in power generation and the proven *know-how* about the manufacturing processes. However, these devices have some intrinsic limitations to further scale-up due to the very low cost-effective processing of silicon wafers; for this reason scientists and researchers are trying to develop new efficient devices with low production cost, in terms of both materials and manufacturing processes.

In this contest, organic and hybrid materials are a very promising alternative for PV technology due to a combination of factors such as the availability of materials, flexibility, low-temperature and solution-based fabrication processes.

## 1.2 HISTORY OF PHOTOVOLTAIC

Generally speaking, solar cells can be classified into wafer-based and thin-film technologies. Wafer-based cells are fabricated on a semiconducting wafer and, for this reason, they do not need any other substrate; for thin-film cells instead, a semiconducting material is deposited onto a conductive glass, plastic or metal substrate. According to the historical classification, the development of solar devices can be divided in three generations:

- The First-Generation includes wafer-based cells of crystalline silicon (c-Si), Gallium Arsenide (GaAs) and other III-V multijunction solar cells. These are the most mature of all PV technologies and represent about the 90% of the global production[6];
- The Second-Generation consists of commercialized thin-film solar cells based on a-Si:H, CdTe and CIGS; these technologies are the alternative to those based on c-Si but with a lower cost[1], because they do not require the use of silicon wafers;

- The Third-Generation consists of emerging thin-film devices that do not require the presence of a traditional p-n junction to separate photogenerated charges. Dye-Sensitized Solar Cells (DSSC), Organic PhotoVolatics (OPV - both polymers and small molecules -), Quantum-Dot Solar Cells (QDSC) belong to this class[7].

However, this traditional classification does not seem to be complete in the description of the modern PV landscape, due to the multitude of device concepts based on new materials (like hybrid Perovskites Solar Cells[8]), new structures (like ThermoPhotoVoltaics[9]) or on light management phenomena (like in Plasmonic Solar Cells[10]) and Hot-Electron Solar Cells[11], that are known as "Advanced Thin Film PVs"[12].

The improvements of the efficiency of all types of solar cells over the years are summarized in Figure 1.3[13].

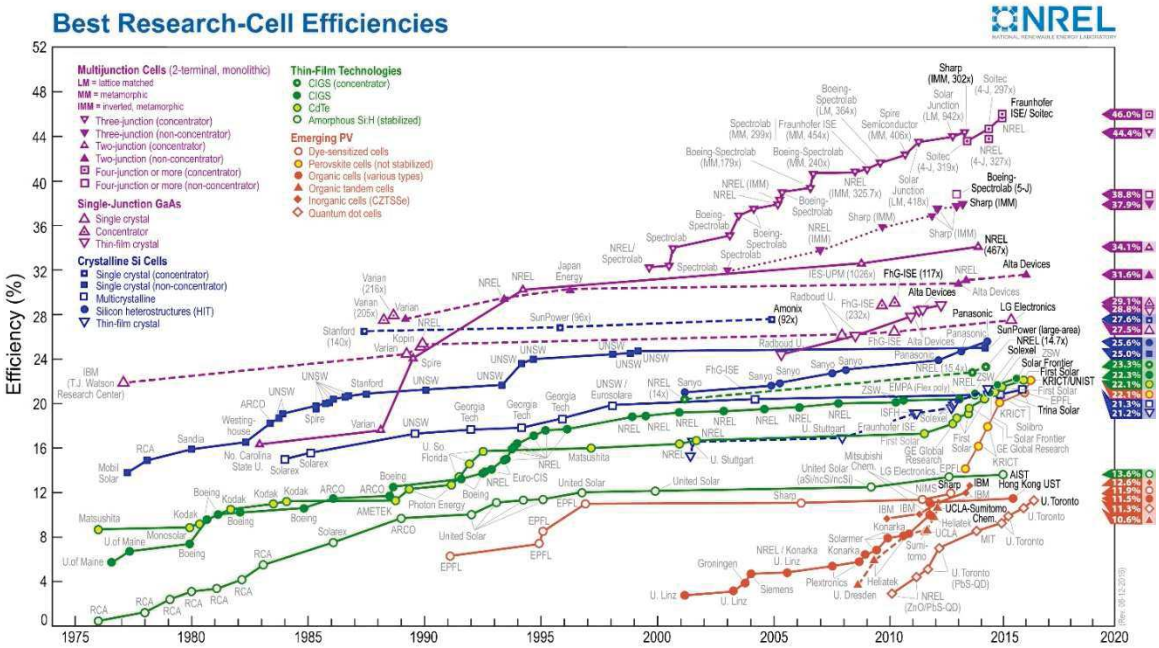


*Figure 1.3- Solar Cells efficiency Chart over years.*

As mentioned above, first and second generation cells show higher performances but organic photovoltaic technology can provide an alternative route to sunlight power conversion in relation to the cost, fabrication simplicity and application where specific mechanical properties (such as flexibility) are required.

### 1.2.1 Inorganic and organic semiconductors

The main differences between organics and inorganics in cell's performances lie in their different electronic structures. In an inorganic semiconductor, the periodic and covalent-bonded arrangement of atoms results into the spatial delocalization of electrons (*i.e.* wave-functions), leading to the formation of continuous bands of energy, including the valence and the conduction bands (VB and CB). Transitions among these bands control light absorption and transport of charges occurs within the bands (band transport), leading to high charge-carrier mobility.

Organic semiconductors present strong (covalent) chemical bonds at the molecular level only, while weak Van der Waals forces dominate intermolecular interactions. Consequently, these materials present weaker delocalization of electronic wave-functions among neighbouring molecules and a narrower bandwidth distribution, causing the HOMO (Highest Occupied Molecular Orbital) and LUMO (Lowest Unoccupied Molecular Orbital) – similar to VB and CB in crystalline inorganic system – levels to be discrete and not continuous. For this reason, charge hopping between localized energy states is the mechanism of transport in organic solids that, being less efficient than band transport, leads to lower mobility.

Another significant difference between the two classes of materials lies on their dielectric constant; the very different values ($\varepsilon_r > 10$ for inorganic compound and $\varepsilon_r \approx 3\text{-}4$ for amorphous organic solids[14]) imply the formation of Wannier-like excitons in the former case and Frenkel-type excitons in the latter. Therefore, optically generated excitons are essentially free at room temperature for inorganic crystals while, in organic compounds, absorption of a photon generates an electron-hole pair localized on individual molecules; their dissociation into free carriers requires additional energy. A hetero-interface can supply this energy (due to the different chemical potential between different materials) to overcome the columbic interaction which binds the electron-hole pair.

Because of electronic structures, the absorption properties of organic and inorganic materials are very different also. Generally, organic compounds have higher absorption coefficients ($\alpha$) in the visible range and present the possibility of molecular design and

engineering for tuning their "band-gap" (and so the absorption and other optical properties).

## 1.3 WORKING PRINCIPLES

In a solar cell, the production of a photocurrent starts with the absorption of a photon and concludes with the extraction of an electron (at one electrode) and a hole (at the other electrode). As already mentioned, comparing to inorganics, in organic solar cells light absorption does not lead instantaneously to free charges but to highly bounded excitons (Frenkel-type) that have to be separated in subsequent steps. The working principles for converting solar energy into electricity by OSCs can be summarized in five step: absorption of photons with exciton generation, excitons diffusion to an interface between different materials named Donor (D) and Acceptor (A), exciton dissociation with the formation of free charge carriers, charge transport into the D or A phases to the electrodes and, finally, charge collection at the electrodes. Each of these steps (illustrated in Figure 1.4) is critical and has to be optimized in order to obtain a high conversion efficiency.

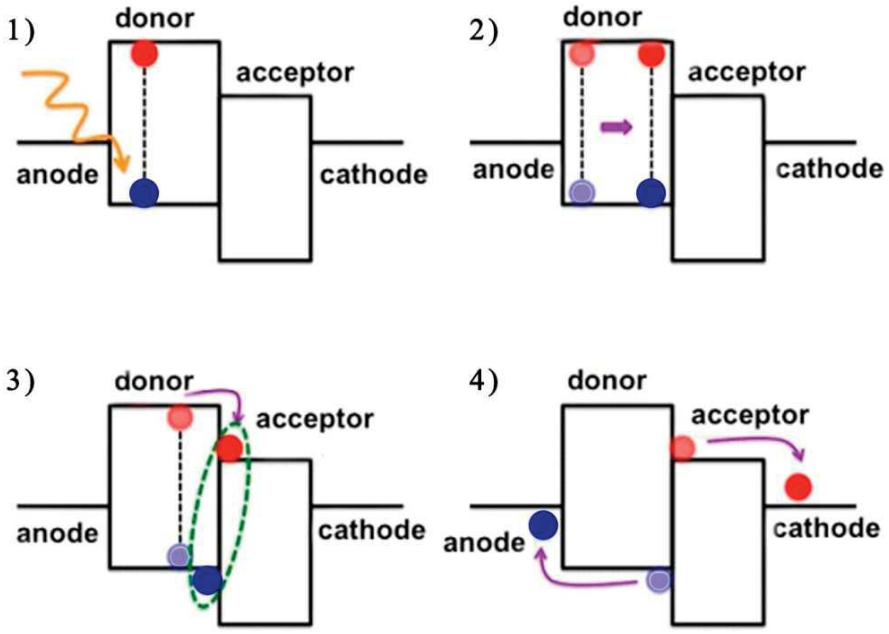


*Figure 1.4- Schematic representation of an OPV working principles.*

### 1.3.1 Light absorption and exciton generation

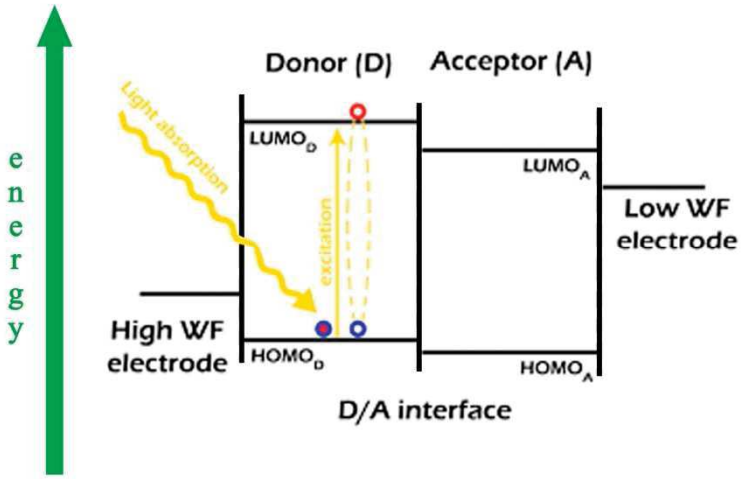


*Figure 1.5- Absorption of light and exciton generation.*

Light absorption in organic materials generates an electron-hole pair usually due to the electron transition from HOMO to LUMO of donor material, as shown in Figure 1.5. Usually, in Bulk HeteroJunction (BHJ) OPV devices, the main light absorber is the D material, since the absorption coefficient and spectral coverage of traditional electron-accepting organic materials is usually much lower than those of their electron donor counterpart. However, the following considerations apply in both cases. The efficiency of light absorption depends on the following factors:

- Optical absorption coefficient.

The absorption coefficient (α) of a compound depends both on molecular properties (*i.e.* molar extinction coefficient, which is the intrinsic capability of light absorption by a single molecule) and on how these molecules are arranged in the solid-state film (*i.e.* their density, the number of molecules for volume unit). Energetic levels of disordered organic materials are usually described by their density of states (DOS) distribution and absorption of light promotes transitions between HOMO and LUMO levels within these distributions (referred as “band-gap”). At the maximum of the absorption spectrum (usually in the

UV/Vis spectral range), the absorption coefficient of organic materials is often high, in the order of $10^5$ $cm^{-1}$.[15] Hence, although the thickness of the active layer of OSCs is limited by electrical conduction (*i.e.* mobility), a few hundreds of nanometers are enough to absorb between 60% and 95% of the incident light[16]. Moreover, to obtain a high absorption of light, it is important to match the absorption spectrum of materials (*i.e*. the band-gap) with the solar radiation. The spectral distribution (or the flux of photons as a function of the wavelength λ) of sunlight outside the Earth's atmosphere (Air Mass 0 or AM 0) follows approximately the blackbody emission at 5800 K. At the Earth level, this spectrum is filtered and attenuated by absorption and/or scattering due to atmospheric gases (like oxygen, water, ozone and carbon dioxide - AM > 0) as shown in Figure 1.6.

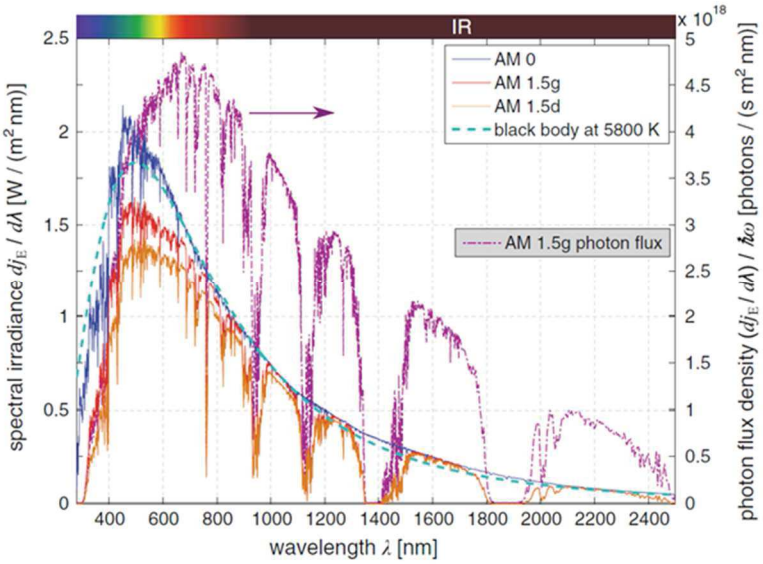


*Figure 1.6- Solar spectrum and photon flux density as a function of wavelength, at different AM values.*

The AM index is a parameter used to indicate the amount of atmosphere that the sunlight has to pass before reaching the Earth surface; AM 1 corresponds to the perpendicular incidence of light at the equator, that is the shorter distance. At any other place on the Earth surface, sunlight has to travel a longer distance. AM 1.5, corresponding to an angle

of incidence of 48.2°, has been chosen as a standard spectrum for solar cell characterization (Figure 1.7).

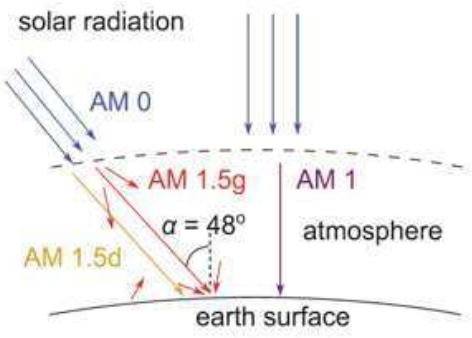


*Figure 1.7- Illustration of the definition of air mass spectra.*

When the AM 1.5 solar spectrum is used, the overall radiant energy flux density is reduced from 1353 W/m$^2$ (the solar constant at AM 0) to about 1000 W/m$^2$. The AM 1.5 spectrum can be further specified in AM 1.5D and AM 1.5G. In the first case, the spectrum includes only the direct light form the sun, in the latter the spectrum includes the direct light form the sun and the back-diffuse light due to the reflection and scattering by the Earth surface. As we can see from Figure 1.6, much of the total solar energy lies in the infrared (IR) region of the spectrum, *i.e.* in the low energy range. This implies that the smaller the semiconductor band-gap, the broader will be the solar spectrum that organic materials can absorb. Different chemical approaches have been used for lowering the band-gap in organic materials, from the synthesis of D-A co-polymers to the substitution of carbon with more electron-rich species like S, N and Si[17].

- Light pathway inside the semiconductor layer;

Of course, the amount of light a material can absorb depends on the light penetration length inside the material itself. This is mainly determined by the thickness of the photoactive film (limited, as mentioned before, by the low charge mobility and low exciton diffusion length in organic materials) and by other factors like reflection, refraction and

scattering at all the interfaces that appear in the device. Other than synthetic approach for trying to obtain new compounds with higher charge mobility, not much can be done for using physically thicker photoactive films. On the other hand, different strategies for light management can be used to obtain an optically thick photovoltaic absorber and to trap or tune the light inside the device[10].

### 1.3.2 Exciton diffusion

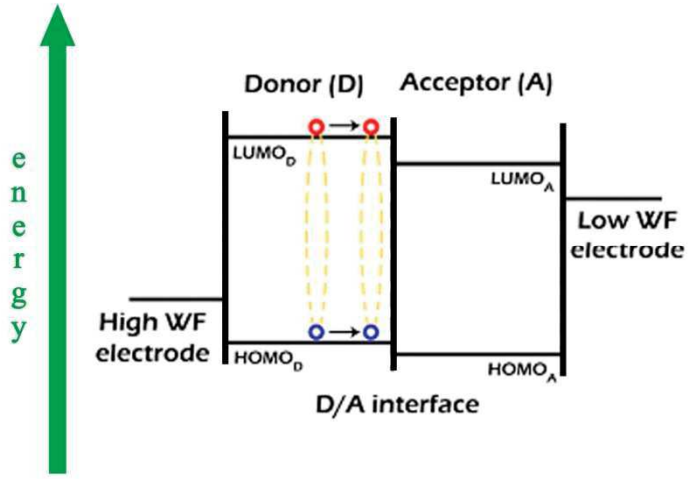


*Figure 1.8-Exciton diffusion.*

Once the light has been absorbed, a Frenkel-exciton is formed due to the promotion of one electron from the ground state to one of the available excited states for the absorbing material; this exciton needs additional energy (in addition to the thermal energy) to overcome its Coulombic binding energy and generate free charge carriers. For this reason, excitons can efficiently dissociate into free carriers only at an interface between donor and acceptor materials (Figure 1.8). Photogenerated excitons have to diffuse towards these interfaces as long as geminate recombination processes (*i.e*. recombination between the hole and electron that make up the exciton) do not happen[18]. Excitons are excited but neutral species and their diffusion can be considered as an energy transfer between a molecule (considered the excitation donor specie) and another molecule

(considered the energy acceptor), that can be described by two different mechanisms, as shown in Figure 1.9. A Förster (long-range) or a Dexter (short-range) energy transfer mechanism. The Förster energy transfer occurs via an electrostatic dipole-dipole interaction between the excited-donor molecule and the energy-acceptor molecule; this process usually occurs within a distance of the order of 100 Å. The Dexter energy transfer mechanism, instead, occurs only between adjacent molecules (distance in the order of 10 Å); in this case, an overlap between the frontier orbitals for the neighbouring molecules is necessary, allowing a direct "double electronic transfer", which results in the energy transfer between the molecules. Exciton diffusion lengths in organic donor phases are usually in the range between 5 nm and 100 nm[19], while in some hybrid perovskite structures, employed for construction of solar cells, it can even reach 1 µm[20].

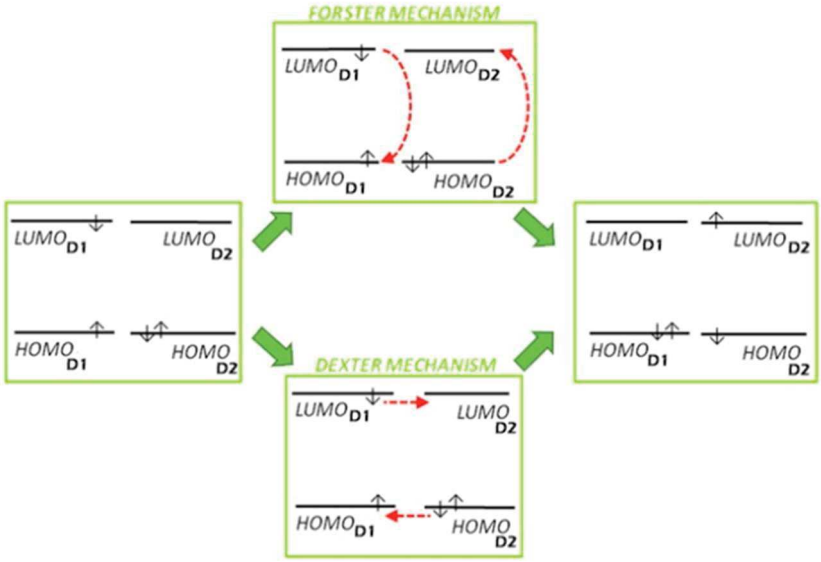


*Figure 1.9- Schematic representation of the Förster and Dexter energy transfer mechanism within two donor molecules.*

### 1.3.3 Exciton separation and generation of free charges

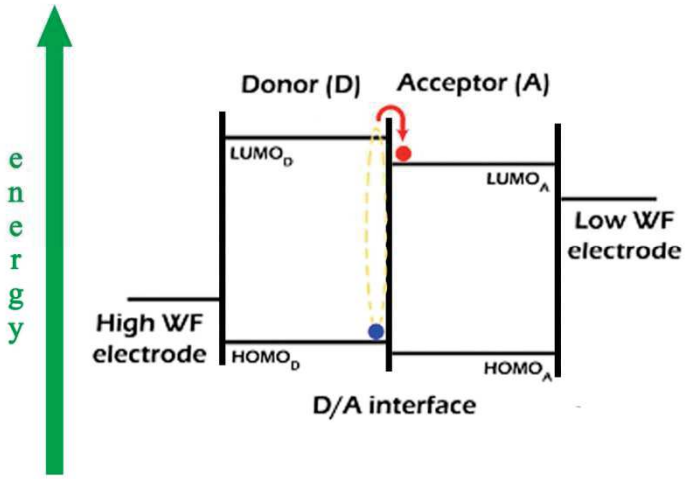


*Figure 1.10- Exciton separation at D/A interface.*

Excitons that survive to recombination processes can reach an interface between donor and acceptor materials. In these spatial regions, the presence of a strong internal field due to the different chemical potentials between the two materials is the driving force required to split the excitons into free carriers, in a very fast process (of the order of tens of fs[21]). As a result, a hole will appear on the donor molecule and an additional electron on the acceptor molecule (Figure 1.10). The most likely and accepted mechanism for this electron transfer consists in a transition from the exciton state to the lowest charge transfer state (CT)[22]. At this point, charge carriers are spatially more separated, residing on two different molecules, but are still bound to each other by Coulombic attractive forces. To overcome this binding energy, an electric built-in field is created by using electrodes with different work-functions at the two sides of the device. In this way, the presence of this field supports charge carrier separation and electrons and holes can diffuse towards their respective contacts, in order to generate a photocurrent.

### 1.3.4 Charge transport to the electrodes

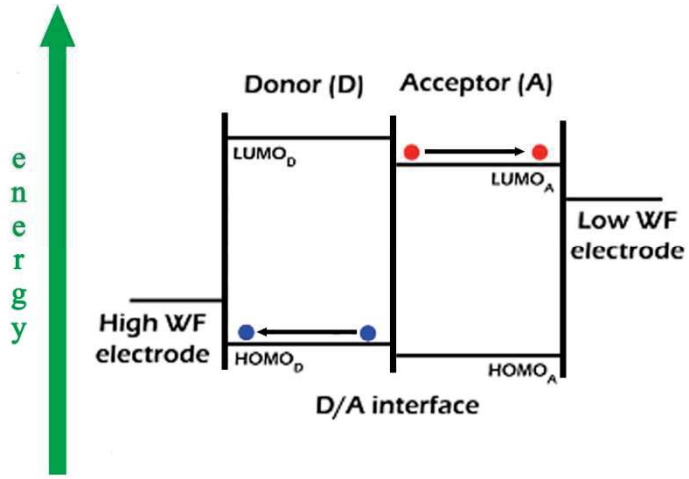


*Figure 1.11- Charge transport to the electrodes.*

The separated charges need to be transported to the electrodes before they recombine. As discussed above, the main mechanism of charge carrier transport in organic semiconductors is the hopping between adjacent molecules. Within this model, holes and electrons move in a drift motion to the respective electrodes thanks to electrical driving forces due to the asymmetrical electrodes chosen for charge collection. Moreover, the concentration gradients of the respective charges can lead to diffusion currents. Indeed, as charges are generated around a hetero-junction, the concentration of electrons and holes are higher around these interfaces and so carriers diffuse along the concentration gradient away from these points. This diffusion current mainly dominates when the applied external bias modifies the internal electric field to nearly zero, while the drift current dominates when the internal electric field is large. It is clear that the mobilities in the donor and acceptor materials are the limiting factors for charge carrier transport; being the hopping mechanism less efficient than band transport, mobilities of organic compounds are usually low, leading to the use of thinner active layers to allow charges to reach the electrodes within their lifetime. Moreover, unbalanced values of hole and electron mobilities in the D

and A phases can have negative effects of charge transport, leading to the build-up of a Space Charge Limited Current (SCLC) regime[23].

### 1.3.5 Charge collection at the electrodes

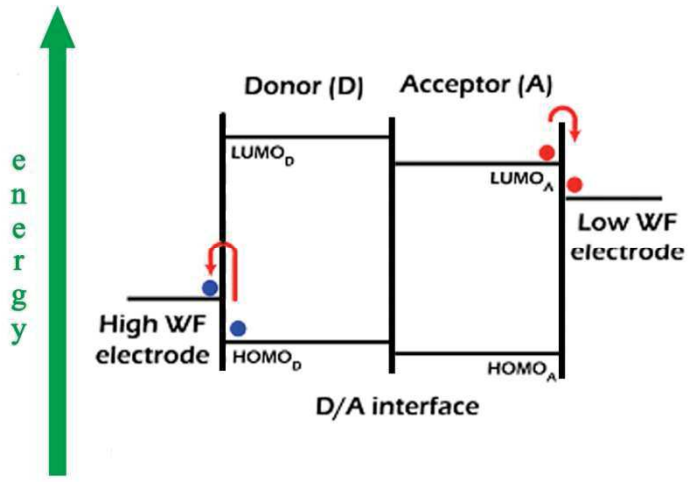


*Figure 1.12- Charge collection to the electrodes.*

After charge carriers reach the active layer/electrode interface, they are extracted from the active layer to the electrodes. To have a high efficient process, the potential barriers at these interfaces have to be minimized, creating Ohmic contacts. This condition is obtained when the work function (WF) of the anode matches the donor HOMO level and the work function of the cathode matches the acceptor LUMO energy, within a difference of ~0.3eV, as indicated by theoretical calculations and experimental evidences[24]. In the case of Ohmic contacts, the open-circuit voltage correlates positively with the difference between the acceptor LUMO and the donor HOMO[25], otherwise the energy level mismatch between the organic frontier orbitals and the WF of the contacts could cause electrical losses for the device. The nature of organic layer/electrode interface is very complex because of several interactions that could occur during the deposition of electrodes on the organic layer (or *vice versa*); interfacial charge-density redistribution, modification of

surface roughness, chemical reactions and physical intermixing are some of the effects that can be relevant. Therefore, it is not always possible to correlate the efficiency of charge collection with the difference between the energies of frontier orbitals of donor and acceptor materials and the WFs of electrodes. Moreover, the selectivity of the electrodes towards only positive or negative charges should be guaranteed in order to minimize the non-geminate recombination of charges due to non-selective charge extraction at the organic layer/electrode interface. The main operational processes to improve charge extraction through manipulation of the contacts consist in[26]:

- Pretreatments of bottom electrodes before deposition of the organic layer; these could improve the alignment of the WF with the charge transport level of donor/acceptor materials, modifying either the electrode WF or its surface chemistry and/or physics[27];
- Improvement of charge carrier selectivity using interlayers. Carrier selective contacts could be obtained either increasing the rate of preferred charge extraction or by decreasing the rate of the recombination process through the blocking of the undesired carriers with an energetic barrier. Depending on their main action mechanism, these interlayers can be known as buffer or blocking layers. Usually a buffer layer consists in an organic or inorganic (oxides) material forming a selective Ohmic contact with the acceptor LUMO (to one side of the cell) or with the donor HOMO (to the opposite one) and with appropriate charge transport properties. Blocking layers instead, in addition to the creation of a better contact for charges as discussed above, have to be characterized by a large band gap, so that injection of electrons from the acceptor LUMO into the conduction band of these interlayers is very unlikely, and *vice versa* for injection of holes from the donor material. Another useful effect can be obtained by using interlayers as optical spacers between organic semiconductors and the reflecting back electrodes, enabling a more favorable redistribution of light into the device. Indeed, an optically transparent thin spacer can lead to an improvement of light harvesting and so to an increase of photogenerated charges and photocurrent[28]. In addition, compared to their inorganic counterpart, organic semiconductors are much more susceptible to chemical degradation in the presence of oxygen, water and under ultraviolet illumination. The insertion of these interlayers can lead to a better stability, by preventing chemical reactions and the diffusion of “hot” metal atoms into the active layer during the deposition of the top metallic contact, which can lead

to shunting or electrical shorting of the organic devices and limit their lifetime[29]. Finally, these interlayers can be used to determine the polarity of the device. For example, Indium Tin Oxide (ITO), a semiconductor made of $In_2O_3$ (90%) and $SnO_2$ (10%), is a common transparent electrode for OPVs and, in combination with a low-work function metal (such as Al), it is used to collect holes (*i.e.* anode). This device polarity is indicated as "standard device configuration" (Figure 1.13 A). Nevertheless, ITO could also be used as cathode to collect electrons; its work function should be tuned in order to increase its electron affinity, and this is achieved by using an appropriate buffer layer (like ZnO or $TiO_2$ for example) and a metal such as Ag or Au as top contact. The device geometry in which the ITO is used as cathode and the metal electrode as anode is called "inverted device configuration" (Figure 1.13 B).

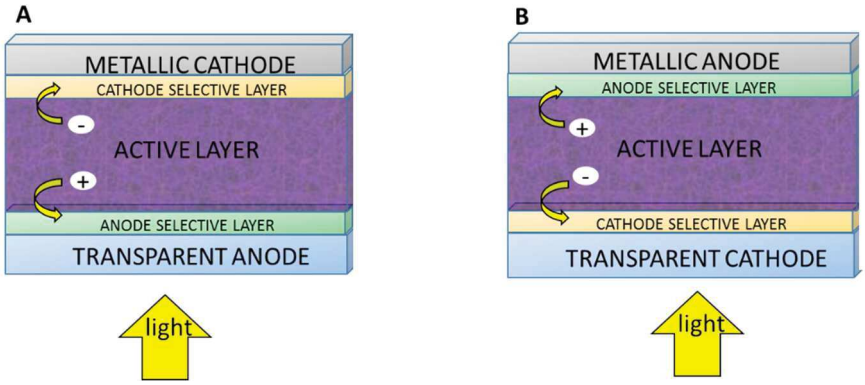


*Figure 1.13- Schematic representation of: (A) standard configuration solar cell and (B) inverted configuration solar cell.*

## 1.4 DEVELOPTMENT OF ORGANIC SOLAR CELLS

### 1.4.1 Single layer OSCs

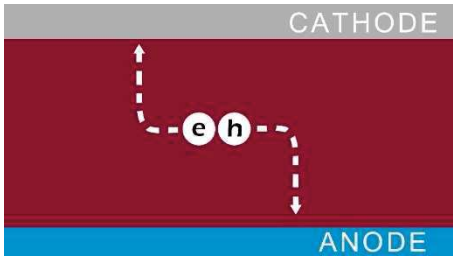


*Figure 1.14- Schematic representation of a single layer OSC.*

In the simplest configuration for an organic photovoltaic device, a photoactive organic material (usually a p-type or a hole transporting material) is sandwiched between two metallic electrodes (one of these has to be transparent), acting as anode and cathode, with different work-function, as illustrated in Figures 1.14 and 1.15.

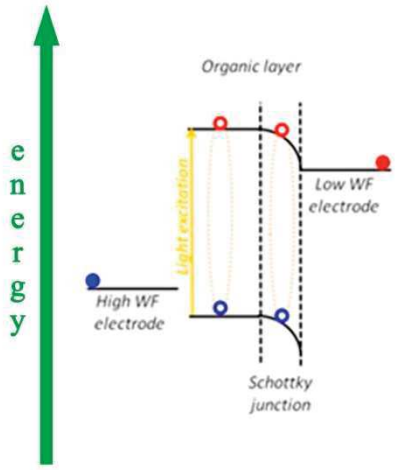


*Figure 1.15- Process and energetics for a single layer OSC.*

This type of structure is kwon as Schottky Junction. From a physical point of view, a Schottky barrier and a depletion region are formed between the organic material and the low WF

electrode; the presence of the electric field leads to the HOMO and LUMO band-bending inside the depletion region. This effect makes the dissociation of excitons, formed or diffused in the depletion region, easier, so the low WF metals can collect the electrons while holes can reach the high WF electrode through the organic material itself. However, the efficiencies of these device are very low (about $10^{-3}$ and $10^{-1}$ %)[30] because of the poor charge mobility, the short exciton diffusion length and the low interfacial area between the organic active layer and the electrodes. Indeed, excitons generated far away from the depletion region can recombine to the ground state before dissociation, and so they do not contribute to the photocurrent.

### 1.4.2 Planar donor/acceptor bilayer hetero-junction OSCs

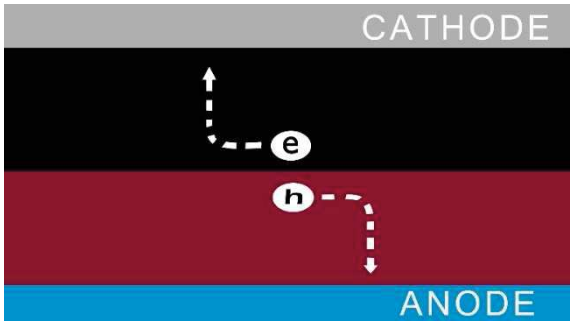


*Figure 1.16- Schematic representation of a planar OSC.*

The first efficient planar bilayer hetero-junction organic solar cell was developed by Tang in 1986[5] and was based on copper phthalocyanine (CuPc) and a perilene-tetracarboxylic derivative (PTCBI), as donor (D) and acceptor (A) materials, sandwiched between two electrodes, as shown in Figures 1.16 and 1.17.

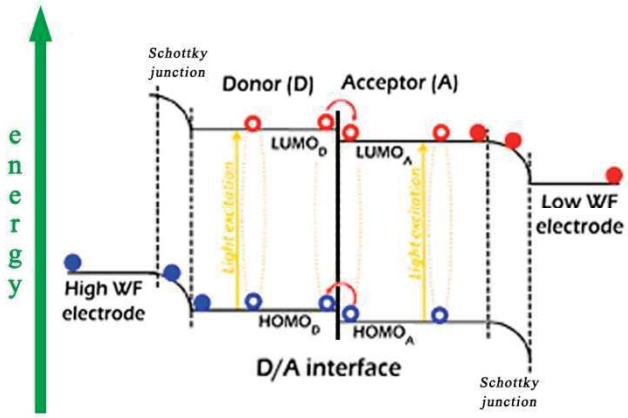


*Figure 1.17- Process and energetics for a bilayer OSC.*

In this structure, the presence of an interface between two different materials - with appropriate frontier energy level offset -is the driving force for exciton dissociation into free charges. It is necessary to have a sufficiently large energy offset at the D/A interface to overcome the exciton binding energy, which is generally considered to be in the range of a few tenths of eV[31]. In this device, once a photogenerated exciton (usually formed in the donor phase) reaches the D/A interface, the electron can be transferred to the acceptor's LUMO ($LUMO_A$) and the hole can remain in the donor's HOMO ($HOMO_D$). Due to both the internal field created by the different electrodes and the chemical potential difference between D and A, the electrons and holes can diffuse towards the respective electrodes more easily than in single layer devices. In addition, the possibility of charge recombination is reduced thanks to the diffusion of electrons and holes in two separated phases. However, the efficiency of these bilayer devices is still limited by both the short exciton diffusion length ($L_d$) and the low D/A interfacial area available for exciton dissociation. Indeed, due to the $L_d$ values of about tens of nanometers[32],the thickness of the active layer should be very low for an efficient charge generation; however, higher thicknesses are required to harvest most of the incident solar light. In planar hetero-junction devices, however, about the 90% of the resulting excitons can be created more

than an $L_d$ far away from the D/A interface. All these excitons are likely to decay to the ground state, without a significant contribution to the photogeneration process.

### 1.4.3 Donor/Acceptor Bulk Hetero-Junction OSCs

A logical and natural way to overcome the problems related to a D/A planar hetero-junction structure consists into maximizing the D/A interfacial area - where excitons can dissociate into free charges - and, at the same time, decreasing the exciton diffusion pathway to the D/A interface - to avoid decay and geminate recombination of these excited species. This can be done by blending the donor and acceptor materials to form a so-called Bulk Hetero-Junction (BHJ) active layer. This revolutionary concept was first introduced by Heeger[33] and Friend[34] in 1995 and it resulted in an impressive increase of cell efficiency, when comparing to the planar bilayer hetero-junction devices[35]. A BHJ is a solid-state mixture of donor and acceptor materials with nanostructured morphology, formed by spontaneous phase separation which is often induced by using, as one of the components, a polymer that tend to separate due to its tendency to crystallize and to its low entropy of mixing[36]. In this structure, the two components create an interpenetrating network with nano-scale domains, in which each of the two materials is fully percolated, forming connected pathways for charges to the electrodes, as illustrated in Figure 1.18.

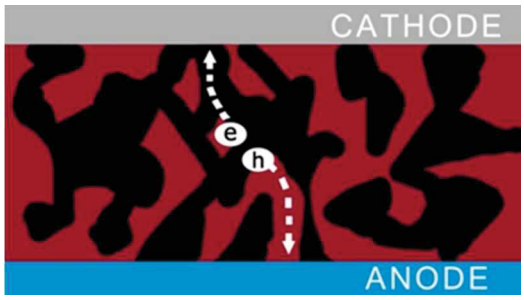


*Figure 1.18- Schematic representation of a BHJ solar cell composed by two intermixed phases of a D (purple) and A (black) material.*

By controlling the phase separation within the active layer, in order to obtain domains of the same length scale of the exciton diffusion length ($L_d$), the efficiency of these devices has been greatly improved because of:

- most of photogenerated excitons can diffuse to the D/A interface and generate free charges upon dissociation;
- these charge carriers can easily reach the electrodes thank to the continuous pathway formed for both materials in the bulk;
- It is possible to use thicker photoactive films, comparing to single or planar bilayer devices, in order to maximize light harvesting.

From these considerations, it becomes clear that the formation of an appropriate nanomorphology is critical to BHJ solar cell performance. The fine-tuning of the morphology of a BHJ can be achieved through the addition of processing additives[37] but, even without using any other compound and/or solvent additive, there are several experimental parameters with a significant influence on the morphology. Molecular structures of the materials, D/A ratios and concentrations of the final solution (% solids) - for solution processed BHJ - and co-evaporation parameters for small molecules OPV, thermal or solvent annealing and post-treatments are just some examples of experimental parameters that can affect phase separation in different ways. The molecular structure controls the solubility and miscibility of D and A in the organic solvents; the solvent governs the drying time during film formation[38]; thermal or solvent annealing influences the domains dimensions, the crystallization degree of the polymer-rich phase and promotes the diffusion of one or both components in the blend, leading to de-mixing and phase segregation[39]. In BHJ devices, both the D and the A phases could contact the electrodes simultaneously. Usually, to avoid the unfavorable contact between one of these materials and the electrodes, that leads to the possibility of charge recombination, interfacial layers used as electron transport layer and hole transport layer are inserted between the active layer and the electrodes[26,40] (Figure 1.19). These interfacial layers can provide significant efficiency enhancements in organic solar cells, via different mechanisms. Two fundamental mechanisms consist in: (a) increasing the photocurrents by reducing extraction barrier heights, *i.e.* acting as ‘‘transport’’ layers, and (b) reducing recombination at the electrodes, acting as ‘‘blocking’’ layers.

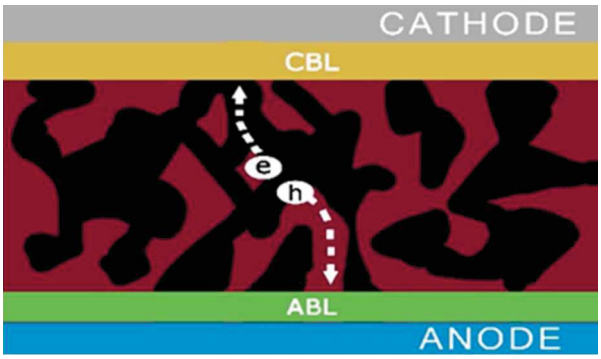


*Figure 1.19- Schematic representation of a BHJ solar cell with a anode buffer layer and a cathode buffer layer.*

## 1.5 SOLAR CELL PARAMETERS AND EQUIVALENT CIRCUITS

### 1.5.1 Equivalent circuits for OSCs

A photovoltaic cell can be described from an electrical point of view using the concept of equivalent circuit (EC). In the simplest case, the EC is constituted by a current generator in parallel with a diode, as shown in Figure 1.20.

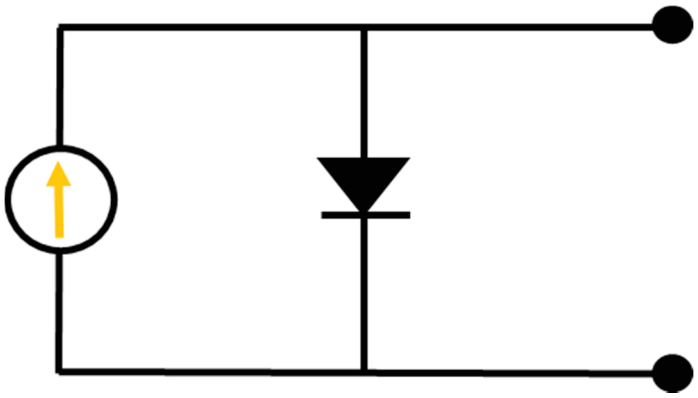

*Figure 1.20- More simple EC for a solar cell.*

Using the Kirchhoff's laws, it is possible to describe the characteristics of a solar cell in terms of current and operating voltage. When not illuminated, the cell behaves like a diode in the dark, with a current that flows under an applied voltage, as shown in Figure 1.21.

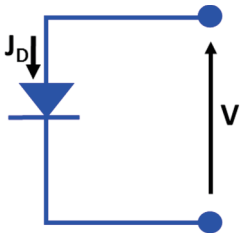


*Figure 1.21- EC for a solar cell in the dark.*

This current is known as $I_{dark}(V)$ or $J_{dark}(V)$ if considering the current density and, for an ideal diode, it can be expressed by the following Equation 1[41]:

$$J_{dark} = J_0\left(e^{eV/K_BT} - 1\right) \quad (1)$$

where $J_0$ is the reverse saturation current of a diode, e is the elementary charge, $K_B$ is the Boltzmann constant, T is the temperature and V is the applied voltage. Consequently, the current-voltage curve for a solar cell in the dark is the exponential characteristic curve of a diode, shown in Figure 1.22.

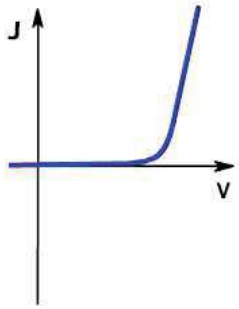


*Figure 1.22- Dark J-V curve for a solar cell.*

Under illumination, the solar cell absorbs photons and generates a photocurrent ($J_{ph}$ – proportional to light intensity) acting in the opposite direction of the diode current, as shown in Figures 1.23 and 1.24.

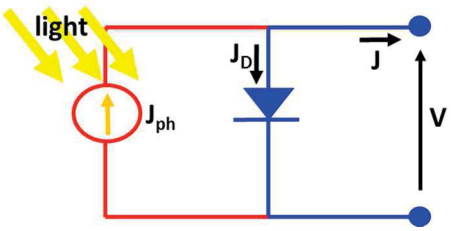


*Figure 1.23- EC for an illuminated solar cell.*

Although the diode current under illumination is not formally equal to $J_{dark}$, this approximation is reasonable for many photovoltaic materials. The net current which flows across an ideal OSC under illumination can be described by Equation 2, known as superposition approximation:

$$J(V) = J_{ph} - J_{dark}(V) = J_{ph} - J_0\left(e^{eV/K_BT} - 1\right) \quad (2)$$

The light has the effect of shifting the J-V curve by $J_{ph}$ in the fourth quadrant, where power can be extracted from the cell.

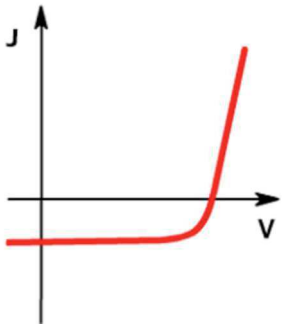


*Figure 1.24- Effect of light on J-V curve for a solar cell.*

A real organic solar cell never reaches these theoretical performances because of its deviation from ideality leading to power dissipation through internal resistance and current leakage. The simplest way to improve Equation 2 for a more accurate description of a real OPV device consists in introducing electrical losses through two parasitic resistances: a series ($R_s$) and a parallel, or Shunt, ($R_p$ or $R_{SH}$) resistance. The more complete EC is shown

in Figure 1.25 and the corresponding equation for describing the current flowing in the cell becomes:

$$J(V) = J_{ph} - J_0\left(e^{\frac{e(V+IR_s)}{\zeta K_B T}} - 1\right) - \frac{V + IR_s}{R_p} \quad (3)$$

Where ζ is the diode ideality factor (usually 1 <ζ< 2 for silicon solar cells). The effect of these two resistors is illustrated in Figure 1.26. The ideality factor is a parameter used to describe how the solar cell slope differs from an ideal diode slope, described by the Shockley diode Equations 1 and 2, and takes account for all the possible recombination mechanisms occurring in a real solar device not explicitly included in the ideal diode equation.

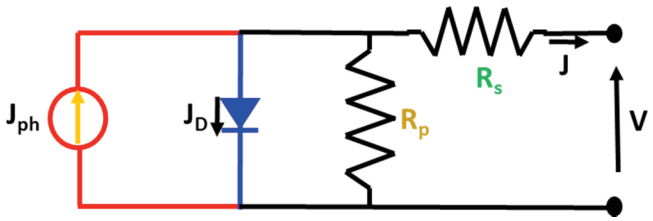


*Figure 1.25- Parasitic Series and Shunt resistances in a solar cell circuit.*

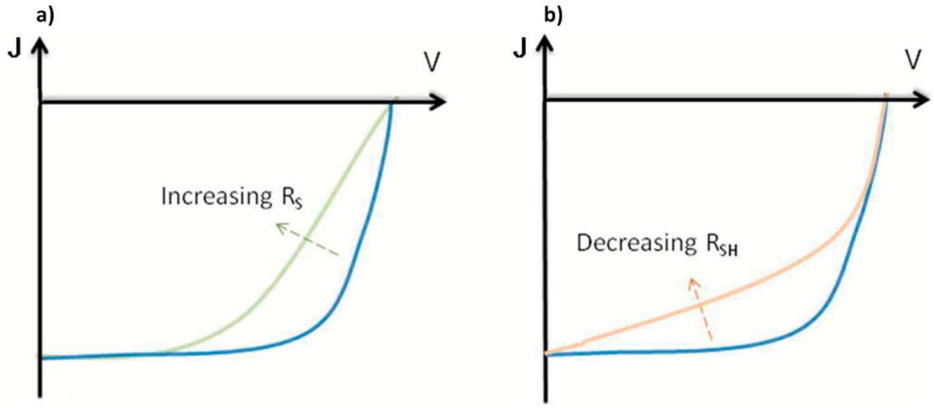


*Figure 1.26- Evolution of the J-V curves of solar cells with a) increase of $R_s$ and b) decrease of $R_p$ or $R_{SH}$.*

The series resistance ($R_s$) arises both from the active materials intrinsic resistivity to charge flow and from all the contact resistances between the different materials composing the solar cell (*i.e*. interlayers, electrodes, all the interconnections). Ideally, its value should be

zero but, in real cases, $R_s$ must be as low as possible. The shunt resistance considers the current leakage due to all possible dispersion mechanisms in the cell (defects, impurities and so on) and its value should be as large as possible, tending towards infinity (no current leakage) for the ideal solar cell.

### 1.5.2 J-V Curves: $V_{oc}$, $J_{sc}$, FF and PCE

The most important parameters for the description of a solar cell are directly available from the current-voltage characteristics, registered under illumination, and are: the short-circuit current ($J_{sc}$), the open-circuit voltage ($V_{oc}$), the fill factor (FF) and the power conversion efficiency (PCE or η). An example of such curve is shown in Figure 1.27, together with the described parameters.

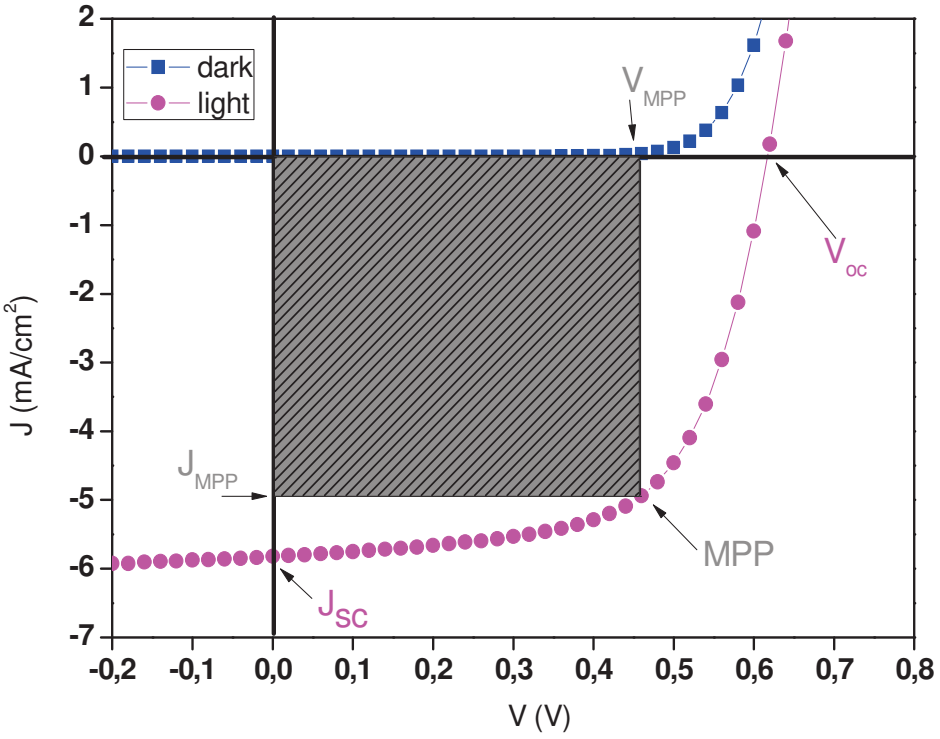


*Figure 1.27- Typical J-V characteristic of a solar cell.*

When the cell is illuminated, it develops a potential difference. If the terminals are isolated, the cell produces an open-circuit voltage; it is the applied bias at which no current flows and the photogenerated current cancels the dark current. If the terminals are connected and the circuit is closed, the current can flow: such current is called short-circuit current in case of a zero bias voltage. The operating region, where the solar cell generates power, is in the range from 0 V to $V_{oc}$, with a power density given by Equation 4:

$$P = J \cdot V \tag{4}$$

- $V_{oc}$ is the maximum voltage available from a solar cell. For inorganic solar cells, this depends mainly on the band-gap of the absorbing materials, although it is limited by charge recombination via radiative decay, as calculated by Shockley and Queisser in 1961[42]. On the other hand, in OSCs $V_{oc}$ is governed by the energy difference between the HOMO of the donor and the LUMO of the acceptor rather than by the band-gap of the absorbing medium (usually the donor), as demonstrated by several studies[43]. Experimental values of $V_{oc}$ can differ from those calculated from this consideration because a lot of other factors can affect the measured $V_{oc}$, either directly or indirectly via interrelated dependencies: among them the morphology of the active layer[44], the electrode work-function[45], the carrier concentration, the density of states and the energetic disorder[46].
- $J_{sc}$ is the current flowing through the solar cell when the voltage across it is zero and it is the largest current that may be drawn from a solar cell. The short-circuit current is due to the generation and collection of light-generated carriers so that $J_{sc}$ mainly depends on the absorption of the donor material (determined by the material absorption coefficient and band-gap) and on the exciton diffusion at the donor/acceptor interface. Moreover, $J_{sc}$ depends on the carrier mobility in the D and A phases, on the morphology in the BHJ layer and on the efficiency of exciton dissociation. However, the most important parameter for increasing $J_{sc}$ is the absorption of light. At first glance, the simplest way to achieve the absorption of more photons consists in increasing the active layer thickness. However, this is prevented by intrinsic material limiting factors, such as low charge mobility. Indeed, if the mobility is too low and/or the active layer too thick, the transit time for the photogenerated charges in the device becomes longer than their lifetime. Consequently, for these devices, there has to be an optimum thickness, depending mainly on the transport

properties of the organic semiconductors. For enhancing the absorption of light, the spectral mismatch between the organic materials and the solar spectrum should also be considered. The absorption of the most used active materials spans the wavelength range from Ultra-Violet (UV) up to 600-650 nm (Vis). The solar spectrum in photon flux as a function of wavelength of Figure 1.6shows that more photons are available for absorption in the Infra-Red (IR) spectral region. From this point of view, it is of great interest to harvest photons at wavelengths longer than 600 nm[47]. To this aim, semiconducting polymers with band-gap from 1.2 eV (absorption onset ~1000 nm) to 1.6 eV (absorption onset ~800 nm) are desired, and different synthetic approaches have been proposed[48].

- As mentioned above, the short-circuit current and the open-circuit voltage are the maximum current and voltage that can be obtained from a solar cell. However, at both of these operating points, the power produced by the solar cell is zero (see Equation 4). In the voltage range between 0 V and $V_{oc}$ the cell generates power; the maximum electric power produced by the OPV cell under illumination corresponds to the Maximum Power Point (MPP) in the J(V) curve, as shown in Figure 1.27. At this point, the solar cell produces a current $J_{mpp}$ under an applied voltage of $V_{mpp}$. In formula:

$$P_{\max} = J_{MPP} \cdot V_{MPP} \tag{5}$$

The ratio between the maximum power obtained by the cell ($J_{MPP} \cdot V_{MPP}$) and the theoretical maximum power that could be obtained from the cell ($I_{sc} \cdot V_{oc}$) is called the fill factor (FF) and it is calculated as in Equation 6:

$$FF = {J_{MPP} V_{MPP}} \Big/ {J_{sc} V_{oc}} \tag{6}$$

The FF gives information about the quality of a photovoltaic cell, representing the deviation of the J(V) behavior of the cell from ideality. Graphically, the FF is a measure of the "squareness" of the solar cell characteristic. The shape of J-V curve, and consequently the FF, are significantly affected both by the ideality factor (ζ) of the cell and by its electrical resistances ($R_s$ and $R_p$). OPVs usually have an ideality factors in the range 1.5–2 due to their inherent disorder. A deviation from unity degrades the FF and it is attributed to various recombination mechanisms (radiative band-to-band transitions, recombination *via* impurities with energy states within the band-gap)[25], which reduce carrier lifetime and,

therefore, the current obtained from the device[49]. Furthermore, the FF could be limited by the set-up of a space charge regime, due to a large difference in the hole and electron mobilities[50]. Moreover, the FF of a device also depends on the series and parallel resistances of the cell. Both decreasing $R_s$ and increasing $R_p$ lead to a higher FF and higher efficiency. Strategies to decrease the contact resistances and the shunt currents include: improvement of the BHJ morphology leading to enhanced charge separation process, use of interlayers, improving mobility of both charge carriers.

- The power conversion efficiency (PCE or η) is the most commonly used parameter to compare the performances of solar cells. Efficiency is defined as the ratio of the maximum power obtained from the solar cell to the incident light irradiance and it is calculated as in Equation 7:

$$PCE = \eta = \frac{P_{out}\left(W/m^2\right)}{P_{in}\left(W/m^2\right)} = \frac{P_{\max}}{P_{in}} = \frac{J_{MPP}\cdot V_{MPP}}{P_{in}} = \frac{FF\cdot J_{SC}\cdot V_{OC}}{P_{in}} \quad (7)$$

The solar cell efficiency depends on the spectrum and intensity of incident light and on the temperature of the device. Therefore, conditions under which efficiency is measured must be controlled in order to compare the different solar cells performances.Standard condition for photovoltaic measurements consists in: temperature of solar cell of 25°C and incident radiation $P_{in}$ of 1000 W/m$^2$ with AM 1.5 spectral shape.

### 1.5.3 Quantum Efficiency

A J-V curve is not sufficient to fully characterize a solar cell. Another important photovoltaic parameter is the External Quantum Efficiency (EQE), also called Incident-Photon-to-Current Efficiency (IPCE). EQE is defined by the ratio between the number of charges extracted out of the solar cell ($N_e$), under short-circuit condition, and the number of incident photons ($N_{ph}$), for each wavelength, as in Equation 8:

$$EQE(\lambda) = IPCE = {}^{N_e}\!/_{N_{ph}} \quad (8)$$

The shape of this curve is highly dependent on the absorption spectrum of the active layer. In particular, EQE is a useful tool when applying techniques to improve absorption in particular wavelength positions; in these cases, in fact, increases in absorption can be reflected as improvements in quantum efficiency at the corresponding wavelengths. If the solar cell quantum efficiency is integrated over the entire incident radiation spectrum, the total photocurrent of the cell ($J_{sc}$) can be obtained. Often, in addition to the EQE, another type of quantum efficiency is considered. This is the Internal Quantum Efficiency (IQE), which is the ratio of the number of charge carriers collected by the solar cell to the number of photons, of a given energy, absorbed by the cell itself. The IQE is always larger than the EQE because in EQE, all the possible losses due to reflection, scattering and transmission are also taken into account. The ideal quantum efficiency graph has a square shape, where the QE value is zero at longer wavelengths (because light is not absorbed below the band-gap of active material) and is constant across the entire spectrum of measured wavelengths. However, the QE for most real solar cells is reduced because of the effects of charge recombination and optical losses due to non-absorbed photons, like in Figure 1.28, as an example.

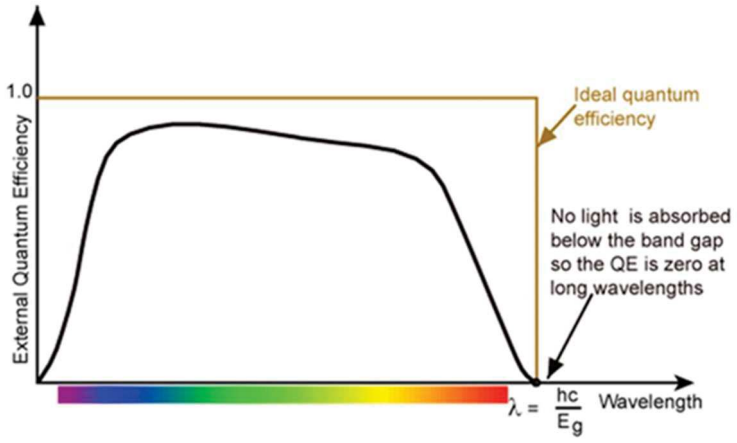


*Figure 1.28- Quantum efficiency of an ideal (Brown) and a Si (black) solar cells.*

## 1.6 FACTORS INFLUENCING THE EFFICIENCY OF BHJ OSCs

From the considerations listed above, the PCE of an OSC is the result of a combination of factors depending not only on material properties, but also on the nanoscale morphology and phase separation of the active layer. Important material properties include:

- A broad and strong absorption band in the visible and near-infrared region to match the solar spectrum (increasing $J_{sc}$) that is, smaller band-gap ($E_g$) materials are desired;
- Suitable LUMO and HOMO energy levels for guaranteeing the exciton dissociation at the D/A interface and for getting higher $V_{oc}$;
- High charge carrier mobility (both for holes in the donor and for electrons in the acceptor) to enhance the charge transport efficiency (increasing $J_{sc}$ and FF).

Regardless of the correct choice of materials, the formation of a rough, non-optimized blend morphology can lead to further losses in OSC. These losses can be divided in three groups:

- Relaxation of excitons that fail to diffuse to and separate at the D/A interface;
- Geminate recombination of electron-hole pairs formed at the D/A interface but that fail to fully dissociate into free charges;
- Non-geminate recombination between dissociated carriers generated by different absorption events (*i.e*. recombination of oppositely charged carriers diffusing through the bulk or surface recombination).

Unfortunately, these requirements are not independent. For example, tuning the LUMO and HOMO energy levels will change the energy band-gap, so influencing the absorption; improving solubility (for solution processed OSC) of the molecules by attaching alkyl side chains will also influence charge carrier mobility, band-gap and nanomorphology. Strategies for meeting all the molecular requirements, from a synthetic point of view, include[51]: D-A copolymerization for narrower $E_g$ and lower-lying HOMOs, substitution with electron-withdrawing groups for lower-lying HOMO, and two-dimensional conjugation for broad absorption and higher hole mobility. For solution processed systems, the BHJ nanoscale morphology is very sensitive to the specific solvent used,[38,52] to the evaporation time and to the annealing processes[53], as well as to the use of additives[54] and to the relative

concentration of donor and acceptor[55]. Therefore, for high photovoltaic performance, it is necessary to accurately balance all properties, optimizing not only molecular structures but also nanomorphology and phase separation in the BHJ structure.

## 1.7 AIM OF THIS WORK

This work is focused on the study of two different crucial aspects for determining the OPV efficiency: first, the opportunity to improve the charge transport to the ITO electrode with novel materials used as anode buffer layer and, second, to increase the absorption of a solar device exploiting the interesting possibilities provided by the engaging field of metamaterials. Several materials for high efficient BHJ organic photovoltaics have been investigated to date but, since ultrafast photoinduced electron transfer from a conjugated polymer to buckminsterfullerene ($C_{60}$) or its derivatives was first observed in 1992 by Sariciftci et al.,[56] this material combination has been the most extensively studied in OPV cells. For this reason, the type of organic photovoltaic active layer studied in this thesis is the polymer:fullerene bulk heterojunction blend made by regio-regular poly(3-hexylthiofene) (P3HT) as a donor and the fullerene soluble derivate $PC_{60}BM$ as an acceptor, deeply studied in the literature. In this way, the effect of different aspects in determining the OPV performances, such as materials, innovative processing and device architecture can be explored using an optimized and well-studied BHJ system as a reference standard. The dissertation consists of 3 chapters:

Chapter 2 is focused on the study of novel materials employed as anode buffer layers (ABL) between the P3HT:$PC_{60}BM$ active layer and the ITO electrode. These consist of photoconductive polymeric thin films obtained from two novel cyclo-metallated complexes containing Pd(II) or Pt(II) as a metal center, 2-phenylpyridine as cyclo-metallated ligand and a triphenylamino-substituted electropolymerizable Shiff base as ancillary ligand. The deposition of these materials onto the ITO electrode was performed through an optimized electropolymerization process. The electropolymerization dynamics and the morphological and electrical properties (photoconductivity and hole mobility) of the resulting thin films

were investigated. Their performance as ABL's in standard configuration solar cells was investigated.

In Chapter 3, an innovative way of enhancing solar cell absorption is described. Based on the excitation of Surface Plasmons in multilayer system, a new concept Hyberbolic MetaMaterial (HMM)-solar device embedding sub-wavelength-sized layers of the P3HT/$PC_{60}BM$ BHJ (as a dielectric) and of Al (as a metal and electrode) with enhanced absorption properties in the near-IR spectral range is presented. A complete characterization of the optical properties of the engineered one-hyperbolic-bilayer structures is given, together with the analysis of the J-V characteristics curves of the plasmonic solar devices studied. Preliminary results based on experimental and simulated data on the two-bilayer system are presented.

In Chapter 4, additional HMM systems based on silver as a plasmonic metal have been prepared and proposed for several applications due to their intriguing features, from the high absorption caused by the excitation of Bulk Plasmon Polaritons to the tuning of the optical properties of HMMs due to a specifically conceived dielectric layer.
Experimental techniques for the preparation and characterization of materials and devices are presented in Chapter 5, while general conclusions of this thesis work and future perspectives are given in Chapter 6.

## 1.8 BIBLIOGRAPHY

[**1**] J. Jean, P.R. Brown, R.L. Jaffe, T. Buonassisi, V. Bulovic, *Ener. Environ. Sci*., **2015**, 8, 1200.
[**2**] A.E. Bequerel, *ComptesRendus de l'Academie des Sciences*, **1939**, 9, 561.
[**3**] A. Einstein, *Annalen der Physik*, **1905**, 322, 132.
[**4**] D.M. Chapin, C.S. Fuller, G.L. Pearson, *J. Appl. Phys*., **1954**, 25, 676.
[**5**] C.W. Tang, *Appl. Phys. Lett.*, **1986**, 48, 183.
[**6**] **a)** International Technology Roadmap for Photovoltaic, seventh edition, **2016**www.itrpv.net/Reports/Downloads/ ;
**b)** M.A. Green, K. Emery, Y. Hishikawa, W. Warta, E.D. Dunlop, *Prog. Photovolt.: Res. Appl.*, **2015**, 23, 1;
**c)** P.T. Chiu, D.C. Law, R.L. Woo, S.B. Singer, D. Bhusari, W.D. Hong, A. Zakaria, J. Boisvert, S. Mesropian, R.R. Karam, *J. Photovolt.*, **2014**, 4, 493.
[**7**] **a)** V. Sagathan, E. John, K. Sudhakar, *Renew. Sust. Ener. Rev.*, **2015**, 52, 54;
**b)** L. Lu, T. Zheng, Q. Wu, A.M. Schneider, D. Zhao, L. Yu, *Chem. Rev.*, **2015**, 115, 12666;
**c)** Y. Lin, Y. Li, X. Zhan, *Chem. Soc. Rev*., **2012**, 41, 4245;
**d)** G.H. Carey, A.L. Abdelhady, Z. Ning, S.M. Than, O.M. Bakr, E.H. Sargent, *Chem. Rev*., **2015**, 115, 12732.
[**8**] Z. Song, S.C. Watthage, A.B. Phillips, M.J. Heben, *J. Photon Ener*., **2016**, 6, 022001.
[**9**] C. Ferrari, F. Melino, M. Pinelli, P.R. Spina, M. Venturini, *Ener.Procedia*, **2014**, 45, 160.
[**10**] H.A. Atwater, A. Polman, *Nature Mater.*, **2010**, 9, 205.
[**11**] C. Clavero, *Nature Photonics*, **2014**, 8, 95.
[**12**] G. Conibeer, *Mater. Today*, **2007**, 10, 42.
[**13**] www.nrel.gov/ncpv/images/efficiency_chart.jpg
[**14**] D. Hertel, M. Bässler, *Chem. Phys. Chem*., **2008**, 9, 666.
[**15**] W. Brütting, *Introduction to the physics of organic semiconductrors in: Physics of Organic Semiconductrors*, **2006**, Wiley-VCH, Verlag GmbH & Co. KGaA, pp 1-14.
[**16**] K.M. Coakley, M.D. McGehee, *Chem. Mater*., **2004**, 16, 4533.
[**17**] **a)** A. Marrocchi, A. Facchetti, D. Lanari, C. Petrucci, L. Vaccaro, *Ener.Environ. Sci*., **2016**, 9, 763;
**b)** J.S. Wu, S.W. Cheng, Y.J. Cheng, C.S. Hsu, *Chem. Soc. Rev*., **2015**, 44, 1113.
[**18**] T.M. Clarke, J.R. Durrant, *Chem. Rev*., **2010**, 110, 6736.
[**19**] **a)** Y. Terao, H. Sasabe, C. Adechi, *Appl. Phys. Lett*., **2007**, 90, 103515;
**b)** H. Marciniak, X.Q. Li, F. Würthner, S. Lochbrunner, *J. Phys. Chem. A*, **2011**, 115, 648.
[**20**] S.D. Stranks, G.E. Eperon, G. Grancini, C. Menelaou, M.J.P. Alcocer, T. Leijtens, L.M. Herz, A. Petrozza, H.J. Snaith, *Science*, **2013**, 342, 341.
[**21**] B. Kraabel, C.H. Lee, D. McBranch, D. Moses, N.S. Sariciftci, A.J. Heeger, *Chem. Phys. Lett*., **1993**, 213, 389.
[**22**] P.B. Deotare, W. Chang, E. Hontz, D.N. Congreve, L. Shi, P.D. Reusswig, B. Modtland, M.E. Bahlke, C.K. Lee, A.P. Willard, V. Bulović, T. Von Voorhis, M.A Baldo, *Nature Mater.*, **2015**, 14, 1130.
[**23**] **a)** L.J.A. Koster, V.D. Mihailetchi, H. Xie, P.W.M. Blom, *Appl. Phys. Lett*., **2005**, 87, 203502;
**b)** B. Ecker, H.J. Egelhaaf, R. Steim, J. Parisi, E. von Hauff, *J. Phys. Chem. C*, **2012**, 16, 16333.
[**24**] A. Kokil, K. Yang, J. Kumar, *J. Polym. Sci. part B: Polym. Phys.*, **2012**, 50, 1130.

[**25**] **a)** B. Kippelen, J.L. Brédas, *Ener. Environ. Sci*., **2009**, 2, 251;
**b)** C.J. Brabec, A. Cravino, D. Meissner, N.S. Sariciftci, T. Fromherz, M.T. Rispens, L. Sanchez, J.C. Hummelen, *Adv. Funct. Mater.*, **2001**, 11, 374.
[**26**] **a)** R. Steim, F.R. Kogler, C.J. Brabec, *J. Mater, Chem*., **2010**, 20, 2499;
**b)** E.L. Ratcliff, A. Gracia, S.A. Paniagua, S.R. Cowan, A.J. Giordano, D.S. Ginley, S.R. Marder, J.J. Berry, D.C. Olson, *Adv. Funct. Mater*., **2013**, 3, 647.
[**27**] **a)** K. He, X. Yang, Z. Wu, Z. Li, S. Zhong, Q. Ou, R. Liang, *Org. Electr.*, **2014**, 15, 1731;
**b)** F. Nüesch, E.W. Forsythe, Q.T. Le, Y. Gao, L.J. Rothberg, *J. Appl. Phys*., **2000**, 87, 7973;
**c)** F. Cheng, G. Fang, X. Fan, H. Huang, Q. Zheng, P. Qin, H. Lei, Y. Li, *Sol. Ener. Mater. Sol. Cells*, **2013**, 110, 63;
**d)** S. Das, J. Joslin, T.L. Alford, *Sol. Ener. Mater. Sol. Cells*, **2014**, 124, 98;
**e)** B. Li, Y. Cheng, Z. Liang, D. Gao, W. Huang, *RCS Adv.*, **2015**, 5, 94290.
[**28**] J.K. Lee, N.E. Coates, S. Cho, N.S. cho, D. Moses, G.C. Bazan, K. Lee, A.J. Heeger, *Appl. Phys. Lett*., **2008**, 92, 243308.
[**29**] G. Williams, Q. Wang, H. Aziz, *Adv. Funct. Mater*., **2013**, 23, 2239.
[**30**] J.J. M. Halls, K. Pichler, R.H. Friend, S.C. Moratti, A.B. Holmes, *Appl. Phys. Lett*., **1996**, 68, 3120.
[**31**] I. G. Hills, A. Kahn, Z. G. Soos, R.A. Pascal Jr., *Chem. Phys. Lett*., **2000**, 327, 181.
[**32**] C.W. Schlenker, M.E. Thompson, *Chem. Commun*., **2011**, 47, 3702.
[**33**] G. Yu, J. Gao, J.C. Hummelen, F. Wudl, A.J. Heeger, *Science*, **1995**, 270, 1789.
[**34**] J.J.M. Halls, C.A. Walsh, N.G. Greenham, E.A. Marseglia, R.H. Friend, S.C. Moratti, A.B. Holmes, *Nature*, **1995**, 376,498.
[**35**] G. Yu, K. Pakbaz, A.J. Heeger, *Appl. Phys. Lett*., **1994**, 64, 3422.
[**36**] A.J. Heeger, *Adv. Mater.*, **2014**, 26, 10.
[**37**] J. K. Lee, W.L. Ma, C.J. Brabec, J. Yuen, J.S. Moon, J.Y. Kim, K. Lee, G.C. Bazan, A.J. Heeger, *JACS*, **2008**, 130, 3619.
[**38**] M. T. Dang, G. Wantz, H. bejbouji, M. Urien, O.J. Dautel, L. Vignau, L. Hirsch, *Sol. Ener. Mater. Sol. Cells*, **2011**, 95, 3408.
[**39**] P.G. Karagiannidis, D. Georgius, C. Pitsalidis, A. Laskarakis, S. Logothetidis, *Mater. Chem. Phys*., **2011**, 129, 1207.
[**40**] J.D. Servaites, M.A. Ratner, T.J. Marks, *Ener. Environ. Sci*., **2011**, 4, 4410.
[**41**] J. Nelson, *The Physics of Solar Cells*, Imperial College Press, First ed., **2003**.
[**42**] W. Shockley, H.J. Queisser, *J.Appl. Phys*., **1961**, 32, 510.
[**43**] D.B. Staple, P.A.K. Oliver, I.G. Hill, *Phys. Rev. B*, **2014**, 89, 205313.
[**44**] N.K. Elumelai, A. Uddin, *Ener.Environ. Sci*., **2016**, 9, 391.
[**45**] A. Zampetti, A.H. Fallahpour, M. Dianetti, L. Salamandra, F. Santoni, A. Gagliardi, M. AufderMaur, F. Brunetti, A. Reale, T.M. Brown, A. Di Carlo, J*. Polym. Sci. Part B: Polym. Phys.*, **2015**, 53, 690.
[**46**] J.C. Blaksley, D. Neher, *Phys. Rev. B*, **2011**, 84, 075210.
[**47**] E. Bundgaard, F.C. Krebs, *Sol. Ener. Mater. Sol. Cells*, **2007**, 91, 954.
[**48**] L. Dou, Y. Liu, Z. Hong, G. Li, Y. Yang, *Chem. Rev.*, **2015**, 115, 12633.
[**49**] C.M. Proctor, C. Kim, D. Neher, T.Q. Nguyen, *Adv. Funct. Mater*., **2013**, 23, 3584.
[**50**] Y.H. Huh, B. Park, I. Hwang, *J. Appl. Phys*., **2014**, 115, 124504.
[**51**] Y Li, *Acc. Chem. Res*., **2012**, 45, 723.

[**52**] N. Zhou, H. Lin, S.J. Lou, X. Yu, P. Guo, E.F. Manley, S. Loser, P. Hartnett, H. Huang, M.R. Wasielewski, L.X. Chen, R.P.H. Chang, A. Facchetti, T.J. Marks, *Adv. Funct. Mater*., **2014**, 4, 1300785;

[**53**] **a)** E. Verploegen, R. Mondal, C.J. Bettinger, S. Sok, M.F. Toney, Z. Bao, *Adv. Funct. Mater*., **2010**, 20, 3519;

**b)** J.Y. Kim, S. Noh, J. Kwak, C. Lee, *J. Nanosci. Nanotech*., **2013**, 13, 3360.

[**54**] D.H. Wang, P.O. Morin, C.L. Lee, A.K.K. Kyaw, M. Leclerc, A.J. Heeger, *J. Mater. Chem. A*, **2014**, 2, 15052.

[**55**] F.C. Chen, C.J. Ko, J.L. Wu, W.C. Chen, *Sol. Ener. Mater. Sol. Cells*, **2010**, 94, 2426.

[**56**] N.S. Sariciftci, L. Smilowitz, A.J. Heeger, F. Wudl, *Science*, **1992**, 258, 1474.

# CHAPTER 2:
# ELECTROPOLYMERIZED PHOTOCONDUCTIVE THIN FILMS AS ANODE BUFFER LAYERS

## 2.1 INTRODUCTION

The constant improvement in OPV performances has been mainly due to the introduction of the BHJ concept and the consequent optimization of the nanomorphology, as well as to the synthesis of new active materials with improved electronic properties. The ideal structure for OSC consists[1] of a bicontinuous (*i.e*. both materials comprising the structure are continuously connected) and interdigitated (*i.e.* where the two materials interlock like fingers of folded hands) network of two materials. Moreover, in order to prevent current leakage, all the photogenerated charge carriers should be selectively collected at the electrodes. This can be obtained when in the structure of the device the pure donor phase is in direct contact with the hole-collecting electrode and the pure acceptor phase with the electron-collecting one. This type of structure would allow for simultaneous control of charge separation, transport (dimension of D and A domains of a few tens of nanometers) and charge-collection, as illustrated in Figure 2.1.

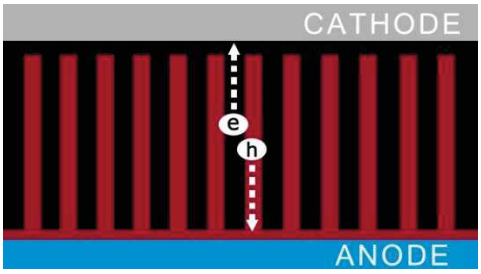


*Figure 2.1- Ideal interdigitated configuration for D/A BHJ solar cell.*

Experimentally, this ideal configuration is not easy to obtain and a more random-shaped interpenetrating network between the two materials is the common BHJ structure, as shown in Figure 2.2.

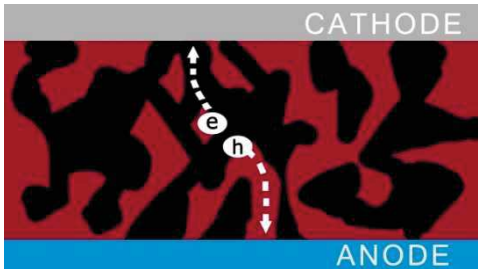


*Figure 2.2- Schematization of a real BHJ solar cell.*

In this structure, both the donor and the acceptor phases are typically in direct contact with both electrodes and non-geminate recombination of charges at the BHJ film/electrode interface can be a problem, due to non-selective charge extraction at the electrodes.

It is well-known that the nature of the electrical contact between the organic active layer and the electrodes is crucial to the overall device performance. An ideal Ohmic contact at the organic blend layer/electrodes interfaces has to be formed[2], with an energy barrier as low as possible for achieving highly efficient extraction for one type of carrier and a high energetic mismatch for blocking the other one. To meet these conditions, the structure of a BHJ solar cell usually includes functional layers interposed between the active layer and the electrodes, both to favor charge extraction and to enhance the selectivity of the electrodes towards electrons or holes. These are usually known as interfacial layers (Figure 2.3).

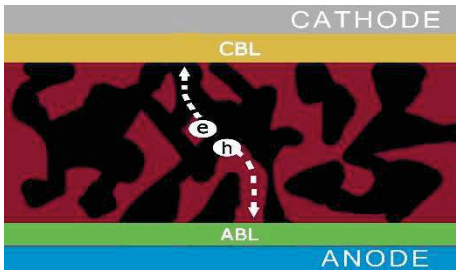


*Figure 2.3- Schematization of a real BHJ solar cell including anode and cathode buffer layers.*

An ideal interfacial or buffer layer for OSC should meet the following requirements:

- Ensure the formation of an Ohmic contact between the organic layer and the electrodes. This aspect is very important, especially for determining the $J_{sc}$ and the $V_{oc}$ of a solar cell. This type of electric contact allows the efficient charge carrier extraction, reducing the recombination losses caused by the accumulation of charges at these interfaces, so that all photogenerated carries can be collected and generate a higher current. Moreover, the Ohmic contact at the organic/electrode interface is important in maximizing the photovoltage obtained from the cell. Indeed, the maximum $V_{oc}$ for a given BHJ system is thermodynamically determined by the energy difference between the $HOMO_D$ and $LUMO_A$ levels and it is obtained only when an Ohmic contact for both the electrodes exists[3].Otherwise, several mechanisms can contribute to diminish the photovoltage of a certain D/A BHJ;
- Have suitable energy levels and a large band-gap to improve charge selectivity and to act as a blocking layer towards the undesired carriers;
- Have high mobility values for selected carriers to reduce resistive losses;
- Have high physical and chemical stability to prevent reactions between the active organic materials and the metal electrode and the diffusion of metal atoms into the organic layer. Moreover, these interlayers can act as a barrier for oxygen and water diffusion into the organic layer, improving the device stability;
- Have a low absorption in the Visible-NIR spectral region, to prevent optical losses. This implies the use of very thin layers of materials, which also meets the requirement of a very low electric resistance;
- Exhibit good film forming properties (both for solution processed and evaporated materials) and improve the surface features of the underlying materials for guaranteeing a uniform deposition and adhesion of the adjacent layers;

The introduction of proper interfacial layers can positively affect the performance of an OSC through the optimization of the electrical properties of the organic/metallic interfaces but their use can also have some additional effects. They can act as optical spacer[4] – to modulate the incident light distribution inside the device and ensure a better absorption of photons from the active layer – or control the device polarity (working in the standard or inverted configuration).

To meet all these requirements within a single material is a big challenge and the choice of a proper interlayer for a given active layer system can be reached with different approaches[5] and classes of materials, such as inorganic materials[6], metal salts[7], self-assembled monolayers[8] as well as organic and polymeric materials[9].

## 2.2 PEDOT:PSS

In a standard configuration device employing ITO as the anode, a water polymeric dispersion of Poly(3,4-ethylenedioxythiophene):Poly(styrene sulfonate) – PEDOT:PSS – is often used as a buffer with the organic layer, to improve the contact properties between the ITO and the active layer and to increase the work function of this electrode for a better hole collection and transport (being this material a hole transporting layer - HTL -[10]). Since its introduction in the '90s,[11] PEDOT:PSS is one of the most commonly employed conducting polymer for several applications[12]. Its chemical structure is illustrated in Figure 2.4.

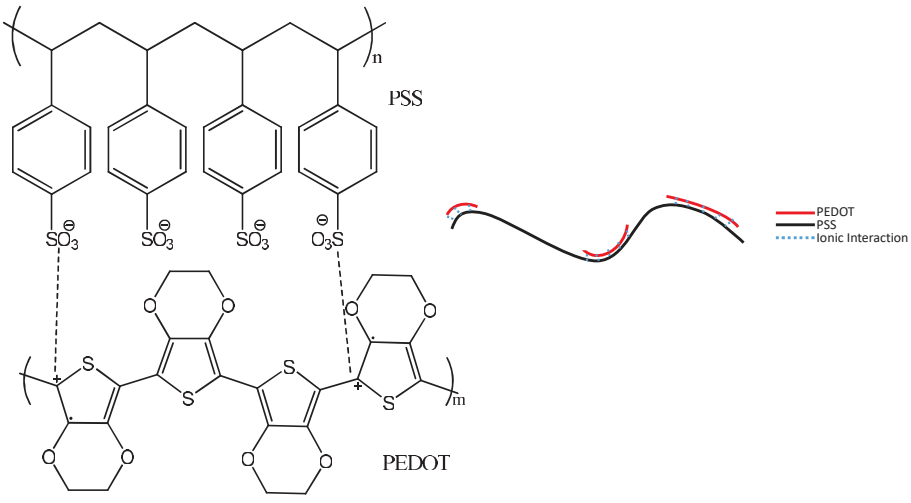


*Figure 2.4- Chemical structure of PEDOT:PSS and schematic representation of interactions between the two polymers.*

A major disadvantage of the "naked" PEDOT backbone is its insolubility in most solvents, directly affecting its solution processability. To overcome this problem, its preparation is conducted with a standard oxidative or electrochemical polymerization of the EDOT monomer in the presence of the water-soluble polyelectrolyte PSS[13].In this way, PSS is the charge-balancing anion of the positively charged PEDOT, resulting in the commercially available PEDOT:PSS. The accepted structure of this compound consists in some PEDOT-rich particles separated by PSS lamellas[10], interacting through electrostatic bounds. PEDOT:PSS presents many advantages as an HTL in OSC, including high conductivity (tuned with dopants[14] and additives acting to improve the crystallization of PEDOT chains), high transparency in the visible range[15], easy processability, non-toxicity and, most important, high robustness against several organic solvents during the deposition of the active layers[16]. Moreover, the deposition of PEDOT:PSS on ITO can lead to a flattening of the substrate surface, since the surface of ITO usually presents a relatively high roughness at the nanoscale, a consequence of the sputtering process used for its deposition onto the substrates (*i.e*. glass)[17]. Finally, as the work-function of PEDOT:PSS ranges between -5.0 and -5.2 eV[18], a good (Ohmic) contact with most of the donor photoactive materials can be achieved.

For inverted configuration solar cells, the use of PEDOT:PSS as an anode buffer layer is not so common, mainly because the high polarity and the high surface tension(*i.e.* hydrophilic nature)of its water dispersion leads to wettability problems on the underlying organic layer. To overcome this problem, the use of additives[19] or surfactants[20] is necessary, which however could cause changes in the PEDOT:PSS electrical conductivity.

### 2.2.1 Drawbacks of PEDOT:PSS

Although PEDOT:PSS is one of the most used materials for anode buffer layers in conventional solar cells on ITO electrodes, its use presents some flaws for the stability of devices. Some of the major problems are related to its hygroscopic and acidic nature. Several studies have been performed to evaluate the effect of ambient moisture on the properties of PEDOT:PSS films and on the performances of the resulting OSCs[21]. All studies

show that water absorption from PEDOT:PSS leads to an increase in resistivity, due to the structural modification of the PEDOT:PSS chains. This degradation appears to be spatially inhomogeneous and could lead to the formation of insulating islands in the PEDOT:PSS/active layer interface, hindering charge collection and lowering efficiency[22]. Moreover, it has been observed that the presence of the sulfonic group in the PSS chains makes PEDOT:PSS films acidic (pH values between 1 and 2). For this reason, PEDOT:PSS can etch the underlying ITO layer, resulting in a poor stability of ITO/PEDOT:PSS interface and in the release of Indium and/or Tin into the PEDOT:PSS film itself, as well as in the active layer, as revealed by Rutherford backscattering and XPS studies[23]. The absorption of water from PEDOT:PSS can facilitate such etching, reducing the device lifetime even further.

As already mentioned[5], these limitations have led to the investigation of the possible use as HTL of many other materials to replace PEDOT:PSS. Among the materials that can be used as anode buffer layers, inorganic transition metal oxides[6] (TMO) have been widely studied, thanks to several suitable properties, such as:

- the capability to resist to solvent erosion;
- the high transparency in the visible range;
- suitable energetic levels for matching the HOMO levels of most donor organic materials (to form ideal Ohmic contact for efficient hole extraction) and simultaneously acting as good electron-blocking layers;
- high chemical and physical stability, resulting in an improved stability for the devices.

TMO layers are usually obtained by thermal deposition (in high vacuum) onto several substrates and materials, regardless of their surface properties and compatibility, but this process prevents their commercial application in low-cost OSCs production. Indeed, for large-scale production and roll-to-roll processes, it is better to deposit these oxides from solution. For this reason, sol-gel techniques and nanoparticles (NPs) solution processes with low or moderate thermal annealing have been developed[24].

Besides TMO, organic and/or polymeric materials that can be covalently linked to the surface of several substrates (*i.e*. ITO) can be used as interlayers, providing additional stability to these interfaces and preventing possible delamination during the solution deposition of the adjacent layers. This is due to the creation of strong chemical bonds, *via*

the formation of self-assembled monolayers[8a] or by the direct deposition on the ITO surface through electropolymerization[25].

## 2.3 ELECTROPOLYMERIZATION FOR PV APPLICATIONS

Electropolymerization[26] is a very simple method for the direct preparation of conducting polymers, if compared with classical chemical reactions[27]. It presents several advantages, such as the absence of catalysts, the simultaneous formation and deposition of the polymers onto a conductive substrate (*i.e*. electrode), an easy control of the film thickness, morphology and properties (*i.e*. doped/undoped states), the opportunity of a simple preparation of copolymers with different compositions and the possibility of *in situ* characterization of the obtained film through electrochemical techniques. As with this preparation method the polymer grows directly on the surface of the electrode, the properties of this interface should be almost ideal from a chemical and physical stability point-of-view (*i.e*. it is difficult to scrape or to wash away with solvent the films electropolymerized onto the surface of an electrode). Several conductive polymers for different applications have been prepared by electrochemical methods: polyphenilenes[28], polypirroles[29], polyanilines[30] and polythiophenes[25d,31].

Electropolymerization can be carried out in galvanostatic, potentiostatic or potentiodynamic conditions, using a common three-electrode electrolytic cell[32]. The three electrodes are:

- The working electrode (WE) where the reactions take place;
- The counter electrode (CE), made up of an electrochemically inert material, used for closing the circuit and allowing the current to flow through the cell.
- The reference electrode (RE), characterized by a stable potential for a wide range of operating condition, used to keep the potential of the working electrode at the desired value.

Some of the properties of the polymers obtained by electropolymerization may be dependent on the choice of the polymerization technique. During a galvanostatic deposition, a constant current is applied between the WE and the CE and, for this reason,

this method is compatible with a two-electrode setup without a RE[33].The cell potential is gradually increased to keep the deposition current constant. Indeed, keeping a constant potential, the current would tend to decrease as a consequence of the increasing resistance due to the growth of the polymer film on the electrode surface. In potentiostatic techniques instead, a constant potential difference (positive for oxidative polymerizations / negative for reductive ones) is applied between the WE and the RE. It is important to choose the value of the working potential: it should be high enough for polymerization to proceed but at the same time, low enough to avoid undesired collateral reactions. Since the concentration of the electro-active species in solution decreases as the reaction progresses, a corresponding decrease in deposition current is usually observed[26]. Pulsed-potential protocols exist as a modification of potentiostatictechniques[32]. This method involves the use of alternating pulses, named as anodic and cathodic pulses, of constant potential for a given time. Lower/upper potential limits and pulse duration can affect polymer morphology and properties[34]. Finally, potentiodynamic electropolymerizations are usually carried out by cyclic voltammetry (CV). In this case, the electropolymerization process is achieved by continuously cycling the applied potential around the oxidation/reduction potential of the electro-active species. The most important experimental parameters that can affect film thickness, morphology and electrical and optical properties are: monomeric solution concentrations, type and concentration of supporting electrolyte, potential limits, number of cycles and potential scan rate.

Considering the mechanism of electrochemical polymerization, generally obtained via oxidative polymerization (rarely via the reductive one, usually employed with vinyl-contained monomers[26,35]), it is well accepted[36] that the first step involves the formation of a cation-radical starting from the monomer oxidation at the anode (“E”-electrochemical step). This is followed by a dimerization between two cation-radicals, with the loss of two protons, often resulting in a re-aromatization (“C”- chemical step). Dimers (and oligomers) are usually more easily oxidized than monomers (another “E” step) because of their greater conjugation, and the polymers growth is the result of subsequent chemical reactions (“C” step) between two cation-radicals or a cation-radical and a monomer. The final electropolymerization process can be described as $E(CE)_n$. Once the polymer layer starts to

form on the electrode surface, the polymerization reaction proceeds on this modified electrode. Two different models for polymer layer formation have been proposed[26,32]:

- Instantaneous nucleation;

According to this theory, the number of nucleation sites is constant and the growth progresses without further nuclei formation;

- Progressive nucleation;

In this case, new nuclei are generated at all times during electropolymerization.
Once nuclei are formed, three different growing mechanism are reported: the 1D growth takes place only in the direction perpendicular to the electrode surface, the 2D growth occurs only in the parallel plane with respect to the electrode and, finally, in the 3D growth mechanism nuclei are characterized by a similar growth rate in both perpendicular and parallel directions.

### 2.3.1 TPA electropolymerization

Among conductive polymers, derivatives of triphenylamine (TPA) are the most widely studied due to two intrinsic and useful functions[37]: the easy oxidability of the nitrogen center and the good hole-transport properties via the cation-radical species. Electrochemical anodic oxidation of TPA has been well studied[38] and its mechanism is illustrated in Figure 2.5

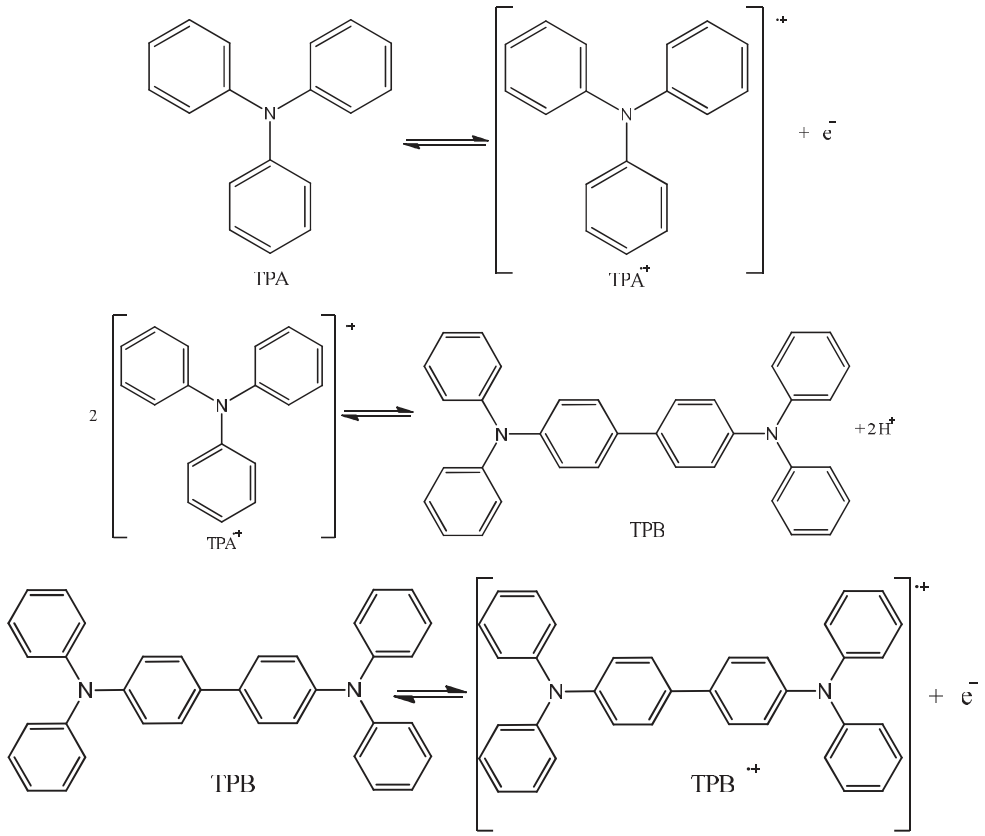


*Figure 2.5- Electrochemical synthesis of TPB dimer.*

The first step consists in the electrochemical generation of the cation-radical $TPA^{+\cdot}$ starting from the TPA monomer. This molecule dimerizes to form the tetra-N-phenylbenzidine (TPB) dimer that is, in turn, more easily oxidized than TPA. Because of the major extended conjugation in TBP, its cation-radical is very stable and this could prevent further reactions and the polymer growth. However, it is possible to control the reactivity by substituting hydrogen atoms with groups with different properties in one of the para-phenyl position, as shown in Figure 2.6. Electron-donating groups have the effect of further increasing the stability of $TPB^{+\cdot}$ making its subsequent reactions very slow and unlikely, while electron-withdrawing groups make this compound to polymerize with an enhanced rate[39], as shown is Figure 2.7.

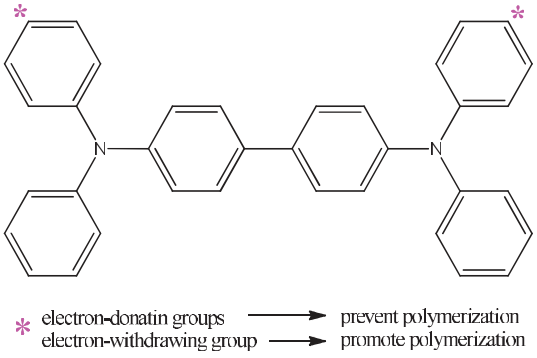


*Figure 2.6- Effect of the substituent group on the activity of TPB dimer.*

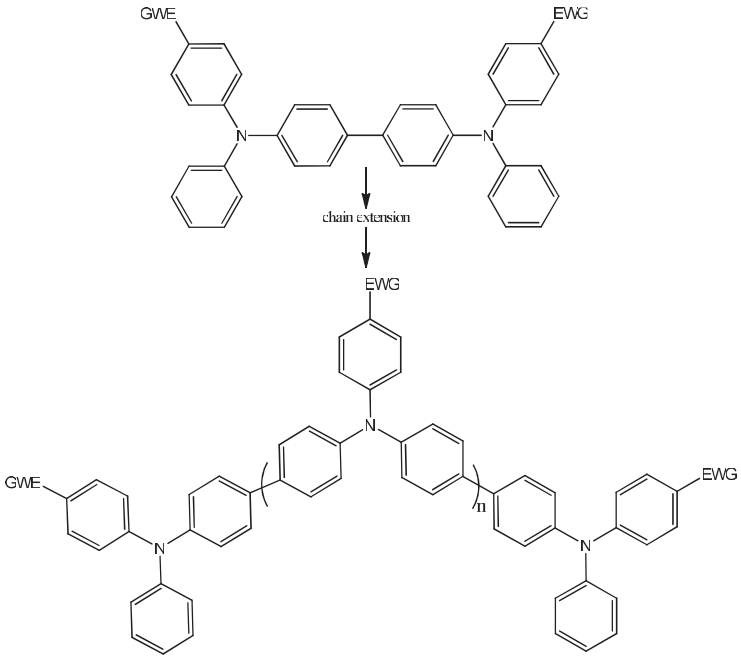


*Figure 2.7- Chain extension by electropolymerization.*

The main uses of low-molecular weight materials and polymers containing the TPA unit (both in the polymer backbone and in pendant groups) are based on their hole transporting, photoconducting and electrochromic properties[40], that make these compounds suitable of OLED (organic light emitting device) and PV applications[41].

## 2.4 PHOTOCONDUCTIVE ORGANO-METALLIC COMPLEXES FOR PV APPLICATIONS

As already mentioned, the current generation in a solar cell is a function of several factors such as absorption of light with an efficient exciton formation, exciton diffusion to a D/A interface, efficient exciton separation into free charges and effective charge transport to the electrodes. For organic semiconductors, the photogeneration of Frenkel-type excitons represents the main drawback in their use in constructing solar devices,[42] due to the need of a proper interface in the bulk of the active layer to create unbounded charges.

A way to overcome this issue could consist in using a photoconductive material. A photoconductive compound is a semiconductor that becomes more electrically conductive due to the absorption of light[43] and, for this reason, exhibits photogeneration properties in the bulk, were no interface is needed. Photoconduction is the result of two processes: photogeneration of charges (either intrinsically – when an exciton is formed and after its dissociation the resulting holes/electrons drift through the bulk material, or extrinsically – when assisted by injection at electrodes, by defect sites or induced by doping[44]) and charge transport throughout the semiconductor. For most organic compounds, the photoconduction is limited by the low photogeneration efficiency. To overcome this limitation, several approaches have been proposed, based on the incorporation of absorbers such as phthalocyanines or on a double layer architecture, where the photosensitizing layer is in contact with a transport layer[45]. Another approach consists in using metal-containing liquid-crystals[46] to combine properties of transition-metal centers (such as the metal stability and the possibility to affect the transport properties of the entire system[47], enhancing its conductivity), the self-organization characteristics of mesogenic compounds and the large extinction coefficient over a wide wavelength range, the easy processing and high flexibility of organic/polymeric materials. Among metal-organic photoconductors (both small molecules and polymers), not only liquid-crystals have attracted attention. To this regard, a series of photoconductive square planar palladium or platinum containing complexes have been intensively studied[48]. The structure of these complexes consists in a five-membered Pd(II) or Pt(II) metallacycle formed by a (C^N) cyclometallated ligand and a six-membered metallacycle, formed with an ancillary

ligand to complete the coordination sphere of the metal, obtained by deprotonation of a Shiff base H(O^N), as represented in Figure 2.8.

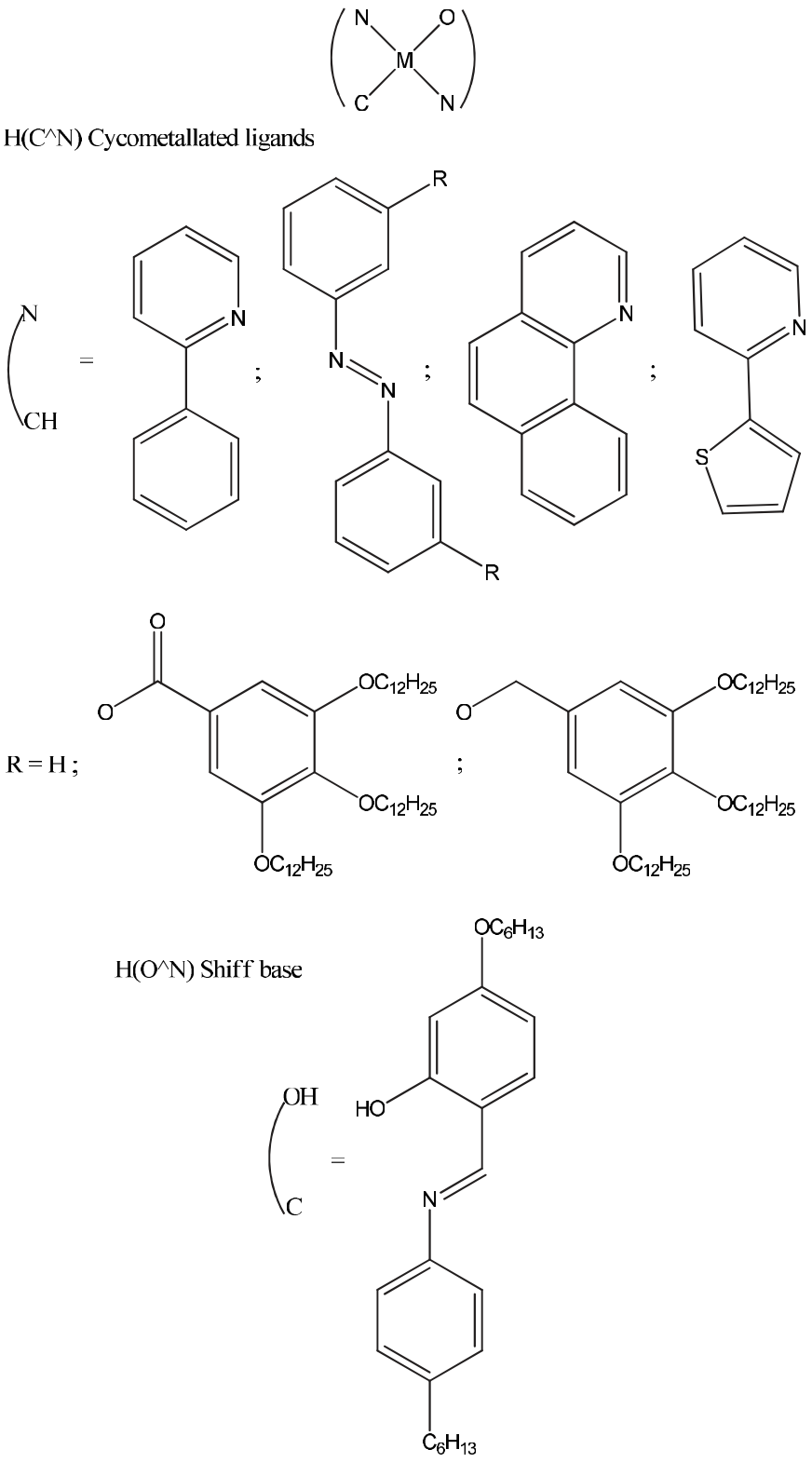


*Figure 2.8- Chemical structures of the photoconductive organometallic complexes.*

The photoconductivity of these complexes can be attributed to a favorable combination of features, as revealed by experimental and theoretical studies[49], such as:

- The square planar metal coordination geometry;
- The in-space separation of HOMO and LUMO orbitals, predominantly located on the two different ligands (LUMO on the (C^N) ligand and HOMO on the (O^N) Schiff base);
- The variation from the planar conformation upon light excitation, leading to a slower charge recombination.

The introduction of organo-metallic photoconductors in OPV devices could have a positive effect on cell performances, using photoconductors both in the active layer[50] and as buffer layers[51].

## 2.5 PHOTOCONDUCTIVE AND ELECTROPOLYMERIZABLE THIN FILMS

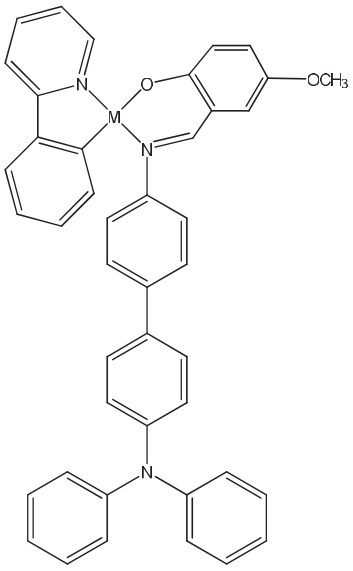


Pd-2 : M = Pd
Pt-2 : M = Pt

*Figure 2.9- Chemical structure of the electropolymerizable complexes under study.*

To combine the features of the above-mentioned photoconductive organo-metallic complexes with the easy processability and advantages deriving from electropolymerization processes, in this work the electropolymerizable TPA unit has been introduced on the ancillary Shiff base ligand while maintaining the 2-phenylpyridine as a cyclometallating ligand. The structure of the resulting complexes under study is shown in Figure 2.9. The choice of this specific molecular fragment as an electropolymerizable group has been motivated by:

- The formation of a cross-linked, highly conjugated polymeric network for isotropic charge transport within the bulk of the material[52];
- The use of a unit with well-known high hole transport properties[40i] onto the ancillary ligand (where the HOMO level is located) for improved charge separation and hole transport;
- The high electrochemical stability of the potentially resulting polymers[40a,41i,53].

## 2.6 EXPERIMENTAL SECTION AND DATA DISCUSSION

### 2.6.1 Synthetic procedures and electrochemical characterization

All the syntheses have been carried out in the Chemistry and Chemical Technology Department (CTC) of the University of Calabria. This particular Shiff base was synthesized through the condensation reaction of 5-methoxy-2-hydroxybenzaldehyde with the properly substituted triphenylamino derivative. Synthetic procedures to obtain Pd-2 and Pt-2 complexes included two steps. The Pd-2 complex was obtained through the formation of its corresponding cyclopalladate acetate-bridged binuclear intermediate A; this was obtained, in turn, by cyclometallation of the H(PPy) ligand with palladium acetate[54].The Pt-2 synthesis, instead, was performed starting from a cycloplatinated mononuclear intermediate B, synthesized by microwave-assisted synthesis[55]. Schemes 2.1 and 2.2 illustrate the followed procedure.

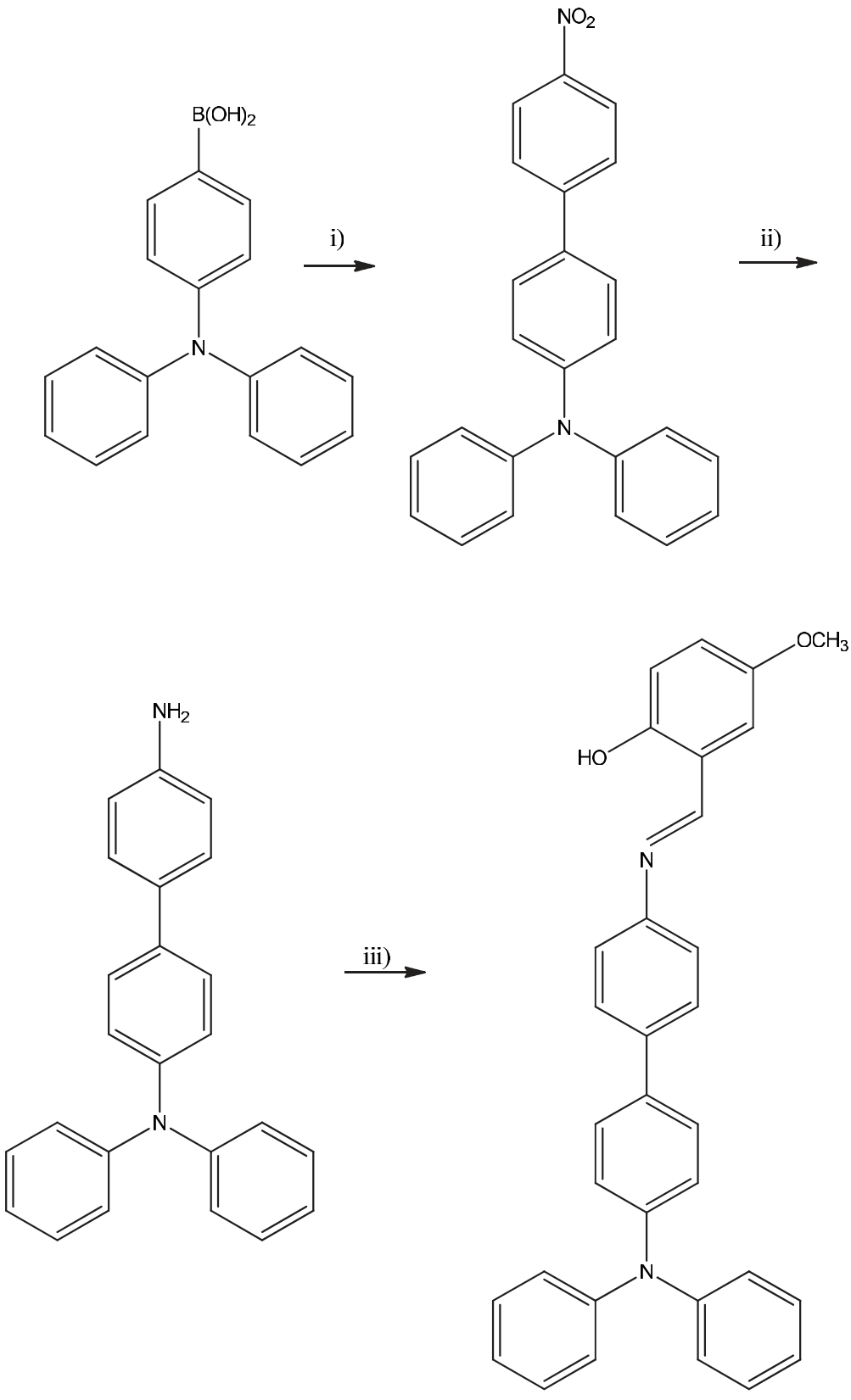


*Scheme 2.1- Synthesis of the TPA-containing Shiff base;*
*i) $Pd(PPh_3)_4$ cat., $Na_2CO_3$ (2M), ethanol/water/toluene 36 h, $N_2$;*
*ii) $NaBH_4$, $NiCl_2$, methanol/dichloromethane, overnight;*
*iii) 5-methoxy-2-hydroxybenzaldehyde, ethanol, reflux, 3 h.*

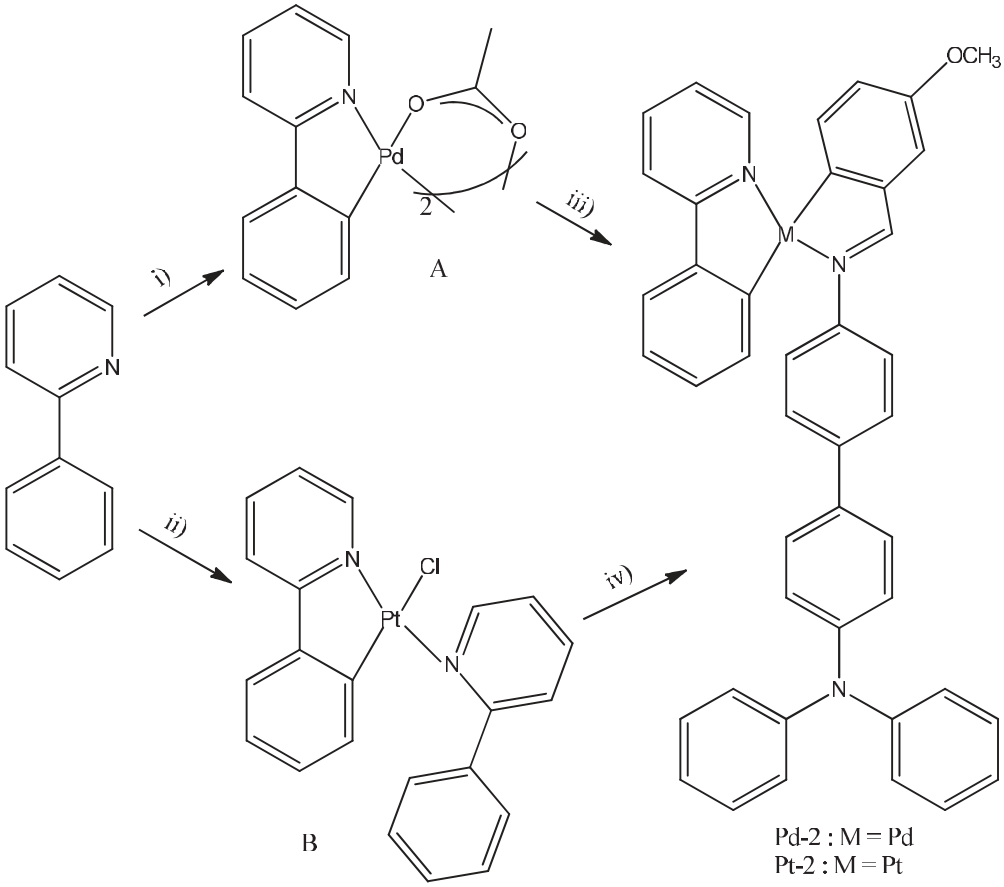


*Scheme 2.2- Synthesis of eletropolymerizable cyclometallated complexes;*
*i) $Pd(CH_3COO)_2$, ethanol, 50°C, 3.5h;*
*ii) $K_2PtCl_4$, 2-$CH_3CH_2OCH_2CH_2OH$:$H_2O$ 3:1 v/v; microwave irradiation (3 cycles, 2 min, 250 W);*
*iii) H(O^N), ethanol, 24h, rt;*
*iv) H(O^N), 2- $CH_3CH_2OCH_2CH_2OH$, $Na_2CO_3$, 80°C, overnight.*

The electrochemical characterization of the synthesized complexes was carried out in the CTC department to estimate their energetic levels. Solution (about $10^{-3}$ M complex concentration) electrochemistry was performed through oxidative cyclic voltammetry using freshly distilled and degassed (with Argon) dichloromethane - DCM - solution with 0.1 M of tetrabutylammoniumhexafluorophosphate - $N(C_4H_9)_4PF_6$ - as a supporting electrolyte. The three electrodes were: a Pt-disk WE, a Pt wire as CE and an Ag wire as a pseudo-reference RE. The data obtained for the two complexes are reported in Table 2.1, with the corresponding estimated HOMO energy values. No reduction wave was recorded in the solvent used and for the potential window investigated (DCM, from - 0.2 to + 1.6 V). LUMO levels were around -2.1 eV for both the complexes and were determined through

reductive cyclic voltammetry experiment in dimethylformamide (DMF). Considering the HOMO/LUMO separation on the molecular scale for this class of complexes[49], this reduction process should be associated with the 2-phenylpyridine ligand.

| *Complex* | *$E^{ox}_1$(V)* | *$E^{ox}_2$(V)* | *HOMO(eV)* | *LUMO (eV)** |
|---|---|---|---|---|
| *Pd-2* | **+ 0.34 (Irrev)** | **+ 0.52 (Rev)** | **- 5.2** | **- 2.1** |
| *Pt-2* | **0.35 (Rev)** | **+ 0.51 (Rev)** | **- 5.2** | **- 2.1** |
| Potential are given versus ferrocene/ferrocinium ($Fc/Fc^+$) couple. Rev = reversible wave; Irrev = irreversible wave. Measurements performed in ~ $10^{-3}$ M DCM solution at 100 $mVs^{-1}$ scan rate.<br>* Measured in ~ $10^{-3}$ M DMF solution at 100 $mVs^{-1}$ scan rate. | | | | |

*Table 2.1- Cyclic voltammetry data for Pd-2 and Pt-2 complexes.*

Two one-electron consecutive oxidation waves were observed for both complexes. This is a characteristic feature of the triphenylamino fragment grafted onto the ancillary ligand[37]. From the reported data, the type of metal center (Pd(II) or Pt(II)) has no influence of the oxidation potentials and, consequently, on the HOMO level energies, estimated at -5.2 eV for both complexes.

### 2.6.2 Electropolymerization on Pt-disk and ITO working electrodes

Upon repetitive oxidation scans, an increase in the WE current is recorded. Such behavior is a clear indication of the polymerization of these compounds on the surface of Pt-disk working electrode. Cyclic voltammograms of the electropolymerization process of Pd-2 (a) and Pt-2 (b) complexes on a Pt-disk are shown in Figure 2.10

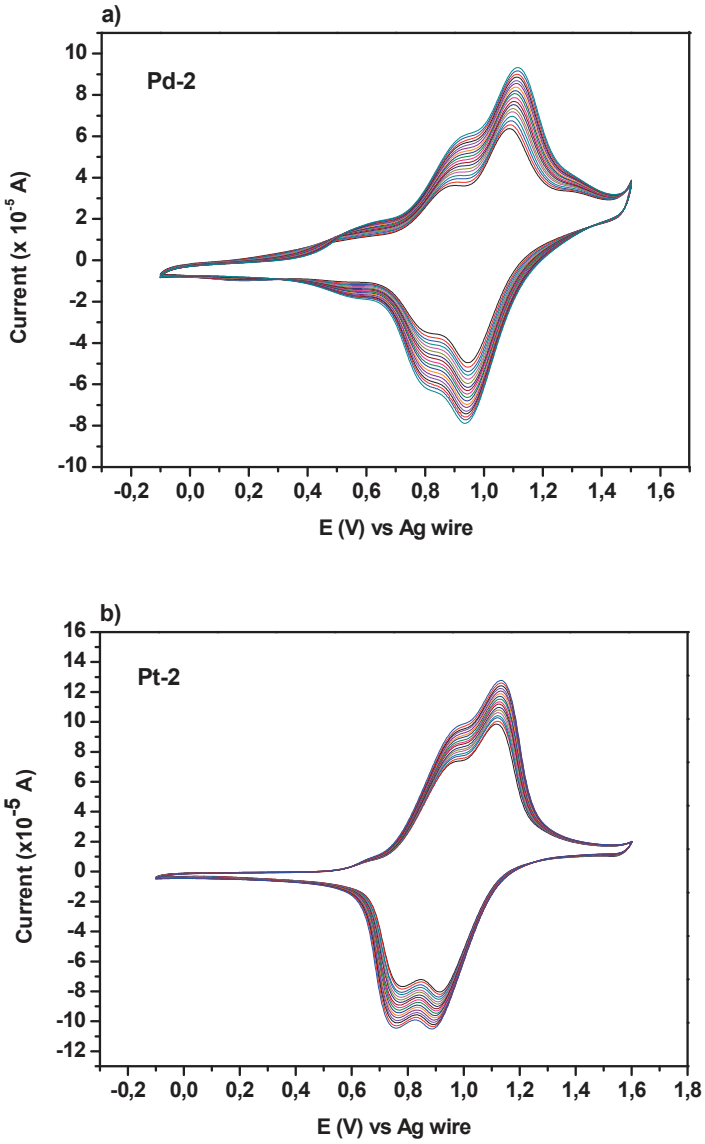


*Figure 2.10- Cyclic voltammograms of a) Pd-2 and b) Pt-2 on a Pt-WE; ca. $10^{-4}$ M DCM solutions for both the complexes; Potential scan range from – 0.2 to 1.6 V; scan rate 100 mV/s.*

After electropolymerization and deposition of polymers, the modified Pt-disk working electrode was immersed in a freshly distilled 0.1 M electrolytic DCM solution to obtain the electropolymerized films electrochemical data (see Figure 2.11). The presence of the two typical oxidation waves is an indication of the effective electropolymerization of these complexes on the working electrode surface. The unchanged oxidation potentials obtained from these measurements confirm that the HOMO levels for these polymers are at the

same energy when compared to the HOMO level of the corresponding monomeric complexes.

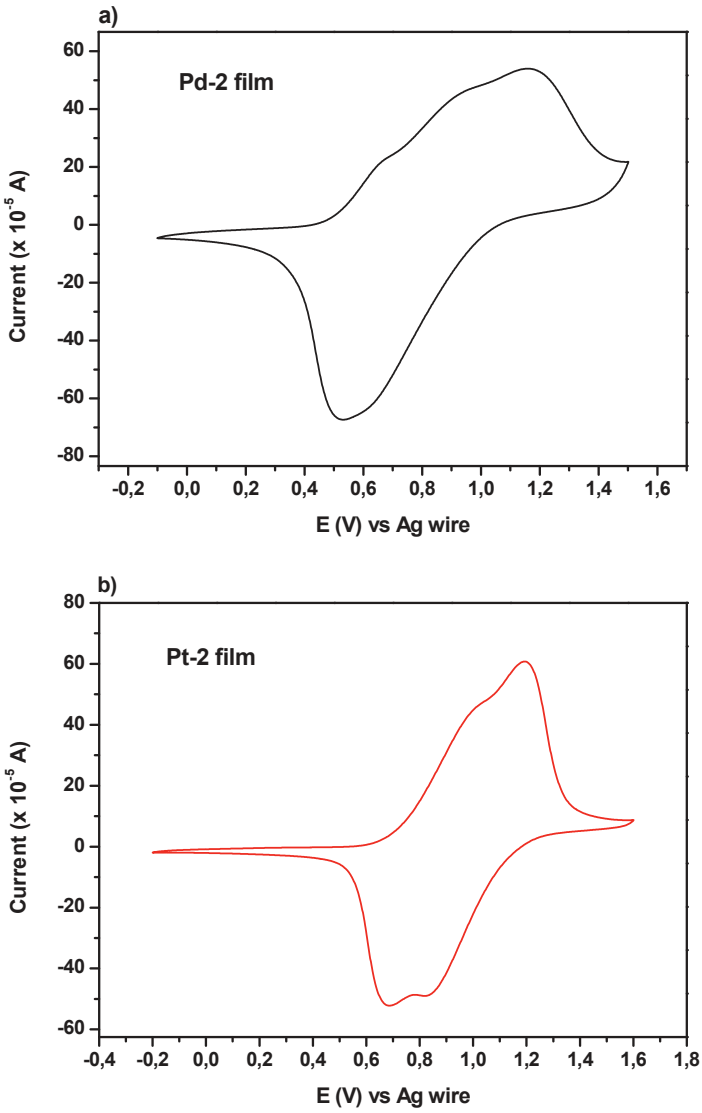


*Figure 2.11- Cyclic voltammograms of the Pt-modified WE in DCM for the previously electropolymerization complexes; a) Pd-2 electropolymerized film and b) Pt-2 electropolymerized film.*

To investigate the photoconductive properties of these polymeric films, it is necessary to deposit them onto a transparent substrate, to ensure that light can reach the active material. Patterned ITO-covered glasses (prepared as described in the experimental section) was chosen as a new WE during cyclic voltammetry electrodeposition. The same solvent, CE, RE, electrolyte concentration, as in the previous electrochemical polymerization on Pt-disk were used. In addition, to perform a reliable photoconductivity

measurement, it is necessary to obtain a film with uniform thickness, surface coverage and without defects (*i.e.* pinholes and cracks). For this reason, several electrochemical experiments were performed, exploring the effects of monomer concentration, number of cycles and different scan rate on the polymeric film formation. Typical electrodeposition CV curves are shown in Figure 2.12 for both complexes.

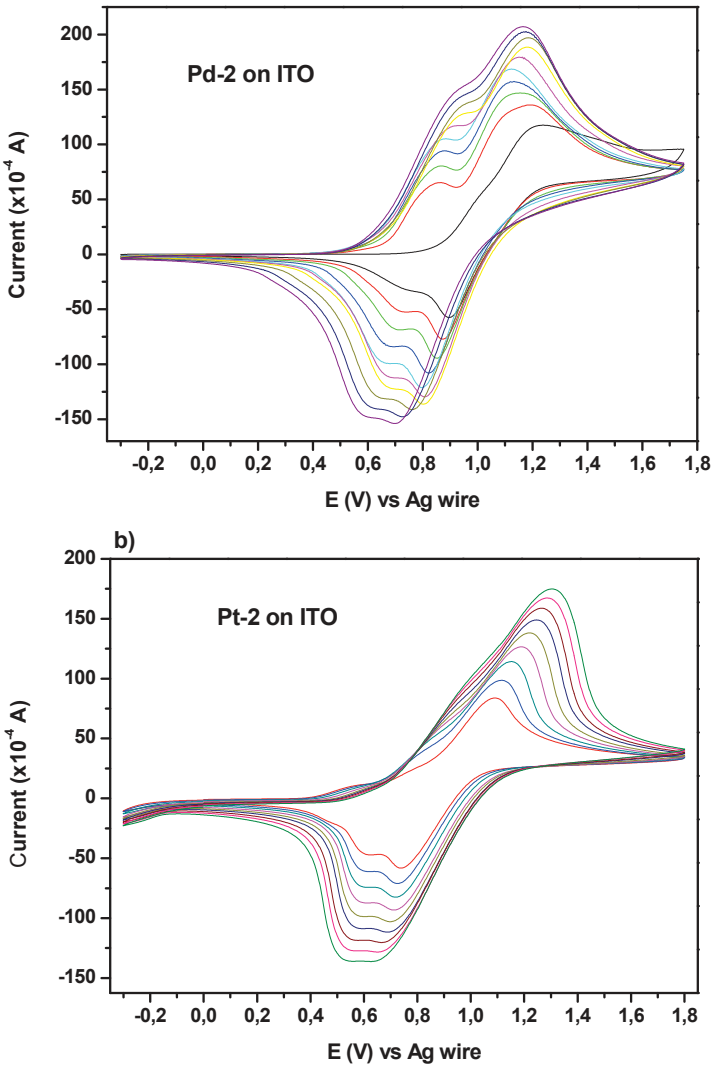


*Figure 2.12- Electropolymerization of a) Pd-2 and b) Pt-2 on ITO covered glasses; 50 cycles (shown every 5 cycles); scan rate 250 mV/s; 2·10$^{-4}$ M and 1·10$^{-4}$M DCM solution for Pd-2 and Pt-2 respectively.*

Figure 2.13 shows a picture of thin films of the Pt-2 complex electropolymerized on ITO-glass at several scan rates – to illustrate the obtained uniformity of deposition onto this WE surface – while Table 2.2 and 2.3 contains data on the thickness range obtained by varying

the monomer concentration, the number of cycles and the potential scan rate for the polymerization of the Pd-2 and Pt-2 complexes.

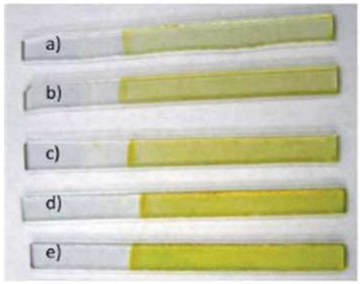


*Figure 2.13- Photograph of electropolymerized films of Pt-2 ($5 \cdot 10^{-4}$ M in DCM) on ITO-coverd glass, at different scan rate: a) 1000, b) 800, c) 500, d) 250, e) 100 mV/s.*

| *complex* | *Unvaried experimental condition* | *Varied experimental condition* | *Range of thicknesses (nm)* |
|---|---|---|---|
| *Pd-2* | Number of cycles: 50<br>Scan rate: 100 mV/s | Concentration from $5 \cdot 10^{-5}$ M to $2 \cdot 10^{-3}$ M | <10 ; 300 |
| *Pd-2* | Number of cycles: 50<br>Concentration: $2 \cdot 10^{-3}$ M | Potential scan rate from 50 to 1000 mV/s | 300 ; 10 |
| *Pd-2* | Scan rate: 100 mV/s<br>Concentration: $2 \cdot 10^{-3}$ M | Number of potential cycles from 10 to 80 | 10 ; 400 |

*Table 2.2- Indication of the obtained thicknesses for Pd-2 electropolymerized thin films on ITO-WE at different experimental condition.*

| *complex* | *Unvaried experimental condition* | *Varied experimental condition* | *Range of thicknesses (nm)* |
|---|---|---|---|
| *Pt-2* | Number of cycles: 50<br>Scan rate: 100 mV/s | Concentration from $5 \cdot 10^{-5}$ M to $1 \cdot 10^{-4}$ M | 20 ; 100 |
| *Pt-2* | Number of cycles: 50<br>Concentration: $1 \cdot 10^{-4}$ M | Potential scan rate from 20 to 300 mV/s | 600 ; 40 |
| *Pt-2* | Scan rate: 100 mV/s<br>Concentration: $1 \cdot 10^{-4}$ M | Number of potential cycles from 10 to 80 | 30 ; 200 |

*Table 2.3- Indication of the obtained thickness for Pt-2 electropolymerized thin films on ITO-WE at different experimental condition.*

### 2.6.2.1 Electropolymerization dynamic

As illustrated in Figure 2.14, the peak currents (both for anodic and cathodic waves) are proportional to the square root of the scan rates for both complexes. This is an indication that the electron transfer is fast and the electropolymerization process is limited by the diffusion of the monomeric species to the electrode[56]. In the opposite case, when the electropolymerization is controlled by the electron transfer with the electrode, the peak current would be linear with the scan rate[57].

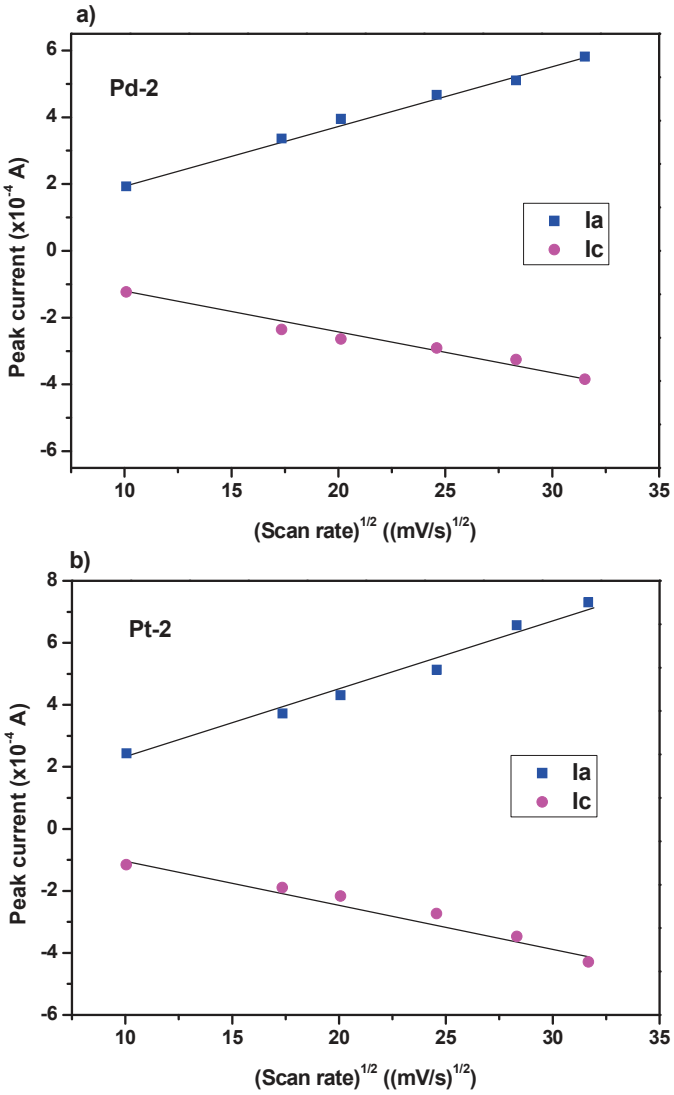


*Figure 2.14- Plots of cathodic and anodic peak currents as a function of scan rate (from 0.1 to 1 V/s) for a) Pd-2 and b) Pt-2 complexes; ca. $10^{-4}$ DCM solutions; data are taken during the 20th cycle of electropolymerization on Pt-disk WE.*

### 2.6.2.2 Electropolymerized film stability

It should be noted that these electropolymerized thin films on ITO show stable cyclic voltammograms after hundred repetitive cycling, in different solvents, such as acetonitrile and tetrahydrofuran, after storage in air and after maintaining the films at an oxidizing potential. Some of these features are illustrated in Figure 2.15.

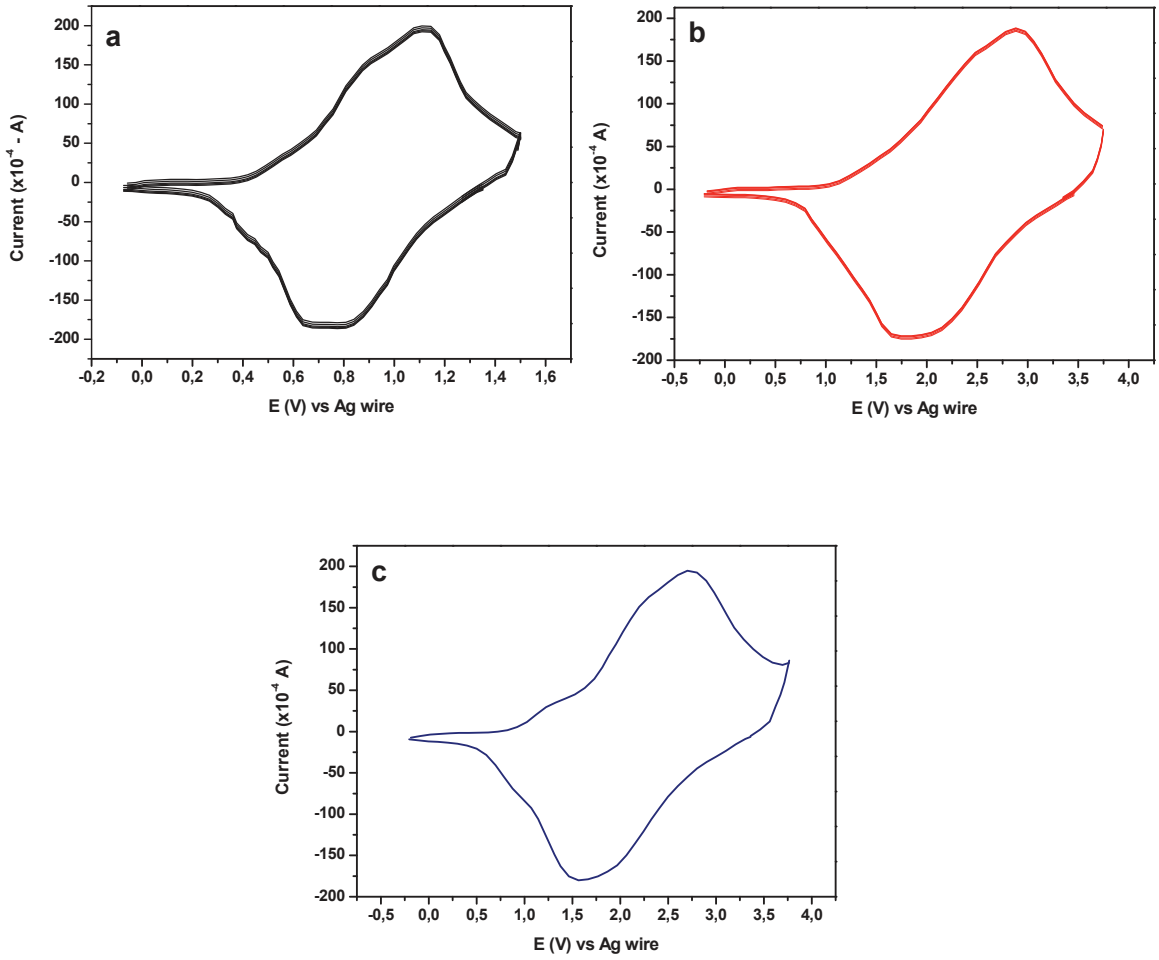


*Figure 2.15- Stability of electrodeposited Pd-2 film in: a) 100 cycles on electrodeposited film after washing with DCM; b) 100 cycles on electrodeposited film used in a) after one night exposure to air; c) 1 cycle on the electrodeposited film used in a) and b) after having kept at 1.5 V for 5 minutes. Note: only one cycle over 25 is shown for clarity.*

### 2.6.3 Thin film characterization

#### 2.6.3.1 Film thickness

These different experimental conditions have an effect on the thickness of the electropolymerized films. Film thickness was measured with a stylus profilometer in several areas of the samples, to evaluate the uniformity of deposition. Typical thickness profiles are shown in Figure 2.16, where the different surface homogeneity between "thin" and "thick" films is emphasized.

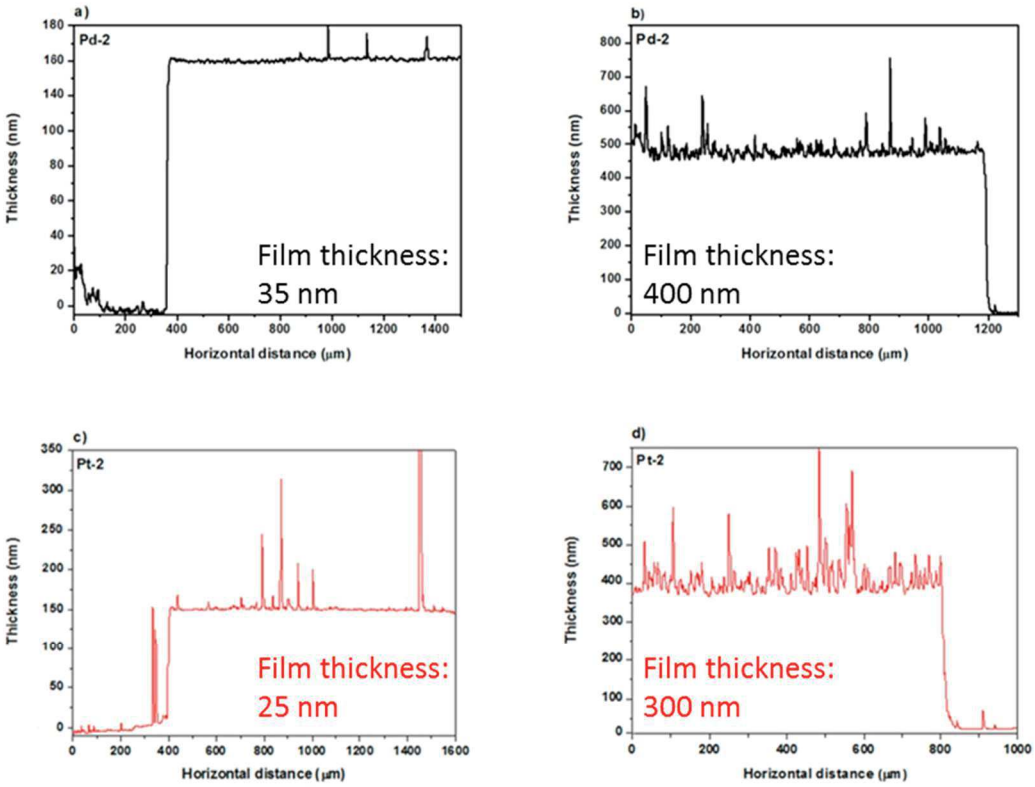


*Figure 2.16- Measured thicknesses for "thin" (a and c) and "thick" (b and d) Pd-2 and Pt-2 films electropolymerized on ITO stripes; real film thickness has been calculated subtracting from these measurements the known ITO thickness of about 120 nm.*

Thinner films of both polymers (Figure 2.16 a and c – about 35 and 25 nm respectively) show a very smooth profile, apart from local spikes due to dust deposition form the environment after film formation. Thicker films (Figure 2.16 b and d – about 400 and 300 nm respectively) instead, show a jagged profile, due to the polymer growth mechanism on the ITO stripes. This thickness-dependence for the film homogeneity remains for all monomer concentrations and for all the varied experimental parameters used; Figure 2.16, indeed, shows the thicknesses for electrodeposited films obtained from optimized electropolymerization conditions.

### 2.6.3.2 Film morphology and surface coverage

The morphology of the electropolymerized films was studied by AFM. As shown in Figure2.17 for electrodeposited films of Pd-2 (obtained from the same monomer concentration and number of cycles) for scan rate values higher than 100 mV/s (Figure 2.17 a), the films present a relative smooth topography, with a root-mean-squared (RMS) roughness of about 5 nm for the 250 mV/s electrodeposited film. For lower scan rates, surface roughness presents an RMS value of about 22 nm (higher roughness) and shows a cauliflower-liketexture[58] as shown in Figure 2.17 b for the 50 mV/s deposited thin film.

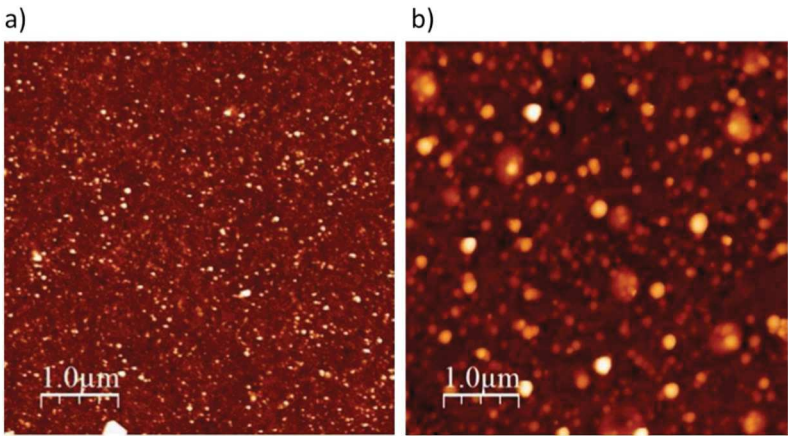


*Figure 2.17- AFM topographic images of Pd-2 electropolymerized film on ITO-covered glasses, from a $5 \cdot 10^{-4}$ M DCM solution at different scan rates: a) 250 and b) 50 mV/s.*

These structures could be the result of the different nucleation and growth mechanisms for high and slow scan rates. In the first case, the creation of new nuclei is faster than their growth, producing a smoother surface with very small domains. The surface coverage of the substrates were determined through Equation[59]1 and plotted against the number of cycles during electropolymerization:

$$\Gamma = {Q}/{nFA} \tag{1}$$

Where Γ is the surface coverage in mol/cm$^2$, Q is the charge in Coulomb – determined by integrating the area under the oxidation peak during the characterization of the ITO-modified electrode in DCM electrolytic solution – n is the number of electrons transferred during the redox process, A is the area of the ITO surface in cm$^2$ and F is the Faraday constant. From Figure 2.18, in the case of the Pd-2 complex, it is clear that the surface coverage, as well as the possibility of obtaining a steady-state peak current during electropolymerization, are strongly dependent on the experimental scan rate.

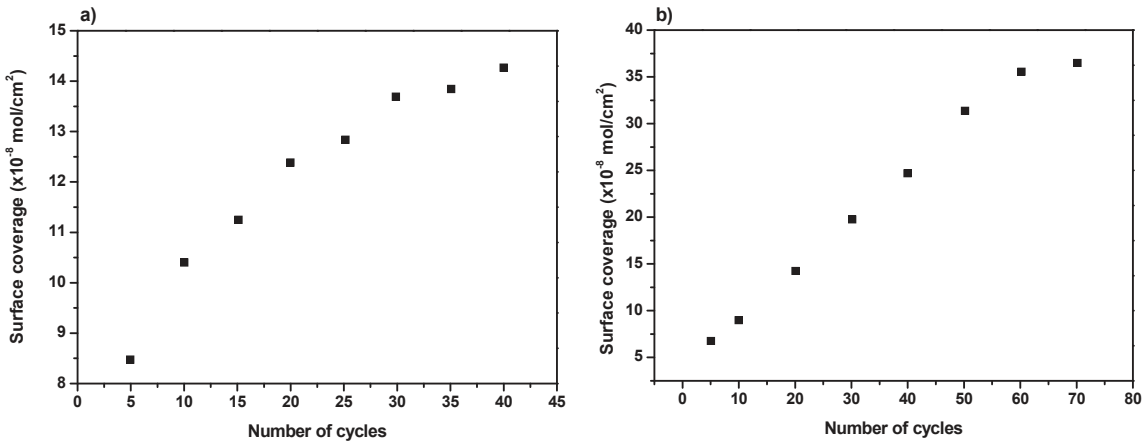


*Figure 2.18- Surface coverage as a function of the number of electropolymerization cycles for Pd-2 complex deposited on ITO covered glasses (2.25 cm$^2$ area) at a) 50 and b) 100 mV/s scan rate from 5·10$^{-4}$ M DCM solution.*

From Figure 2.18 a and b, it is evident that, although a constant peak current is not fully reached in both cases, the coverage dependence on the number of cycles becomes less steep after 35 cycles for electropolymerization at 50 mV/s (Figure 2.18 a), while only after 60 cycles for a scan rate of 100 mV/s (Figure 2.18 b).

### 2.6.4 Photoconductivity of electropolymerized thin films

Photoconductivity ($\sigma_{photo}$) measurements have been performed both on the electropolymerized thin films and on the Pd-2 and Pt-2 monomers, in their amorphous state, for direct comparison. Sample preparation, as well as the derivation of the $\sigma_{photo}$ from measured currents, are described in the chapter of the experimental methods. Photoconduction measurements have been conducted by irradiating the samples in the absorption tail, at a wavelength of 532 nm, as indicated in Figure 2.19.

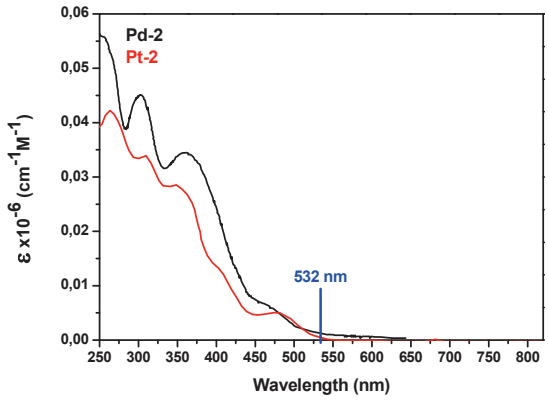


*Figure 2.19- Absorption spectra of Pd-2 and Pt-2 complexes; indication of the λ = 532 nm used for photoconductivity measurements.*

This choice was dictated by the need to illuminate the entire thickness of the samples to obtain a reliable bulk photoconductivity value. The photoresponces of these compounds are shown in Figure 2.20.

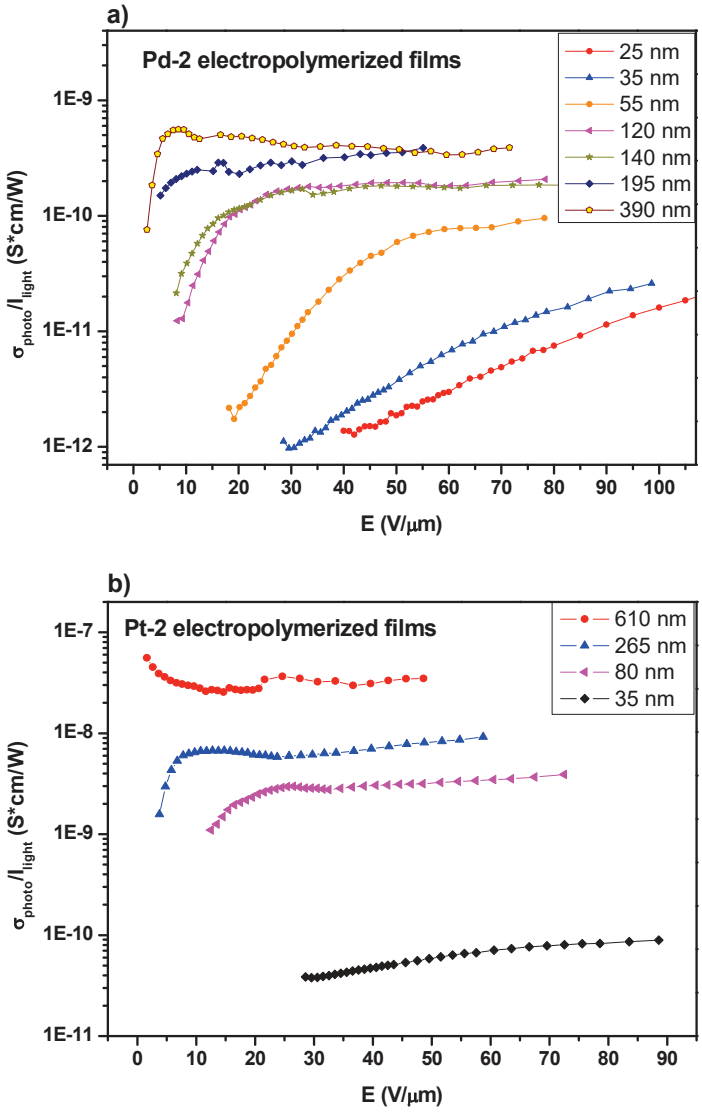


*Figure 2.20- Photoresponce of a) Pd-2 electropolymerized films from 25 to 390 nm and b) Pt-2 electrpolymerized films from 35 to 610 nm, as a function of applied electric field (ITO/Al cells, negatively polarized ITO electrode)*

It is to be noted that the measured photoconductivity is a function of the film thickness. This result may be due to the relative weight of interfaces with respect to the bulk material for thinner and thicker films. In the first case, in fact, charge trapping at the electrode/photoconductive layer interfaces could have a major effect on the decrease of bulk photoconductivity. For this reason, comparison with the photoconductivity of the electropolymerized films of the two monomers has been made only for the *ca*. 200 nm-thick films, which are the most reproducible ones, as shown in Figure 2.21.

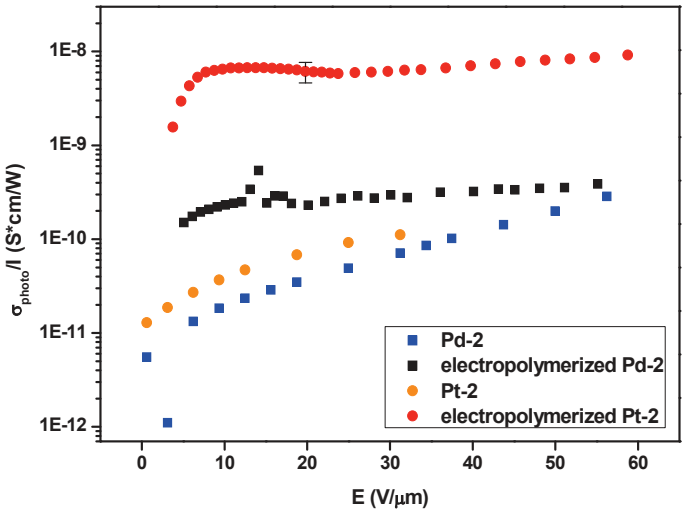


*Figure 2.21- Photoresponces of Pd-2 and Pt-2 complexes and their corresponding electropolymerized films (thicknesses of 195 nm for Pd-2 film and 265 nm for Pt-2).*

In both cases, the photoconductivities ($\sigma_{photo}$) of the electropolymerized films are higher than those of the corresponding monomers, especially for low values of applied electric fields. Considering that, at low fields, the increase of photoconduction with increasing electric field is mainly due to a better photogeneration efficiency rather than to an increase of charge mobility[60], this behavior could be an indication that electropolymerization of these metal complexes leads to an increase of their photogeneration efficiency. Furthermore, it should be noted that the thicknesses of the two types of samples are very different (*ca*. 4 μm for monomer cells and *ca*. 200 nm for electropolymerized thin films). For the polymers, the increased charge trapping phenomenon already discussed might still be present, due to the relatively higher impact of interfaces. For this reason, the photoconductivity of the electropedosited films could even be underestimated. Thicker but, at the same time, homogeneous and defect-free films, to limit this effect on the electrical measurement, are difficult to prepare experimentally. Moreover, the substitution of the Pd(II) metal center with Pt(II) results in an increase of the photoconduction, as previously observed for analogous complexes. Also in this case, this difference could be correlated to the higher population of longer living triplet excited state that characterize

the Pt complexes[49]. Photocurrent was also measured *versus* intensity of light for electropolymerized films of *ca*. 200 nm in thickness. The results are shown in Figure 2.22:

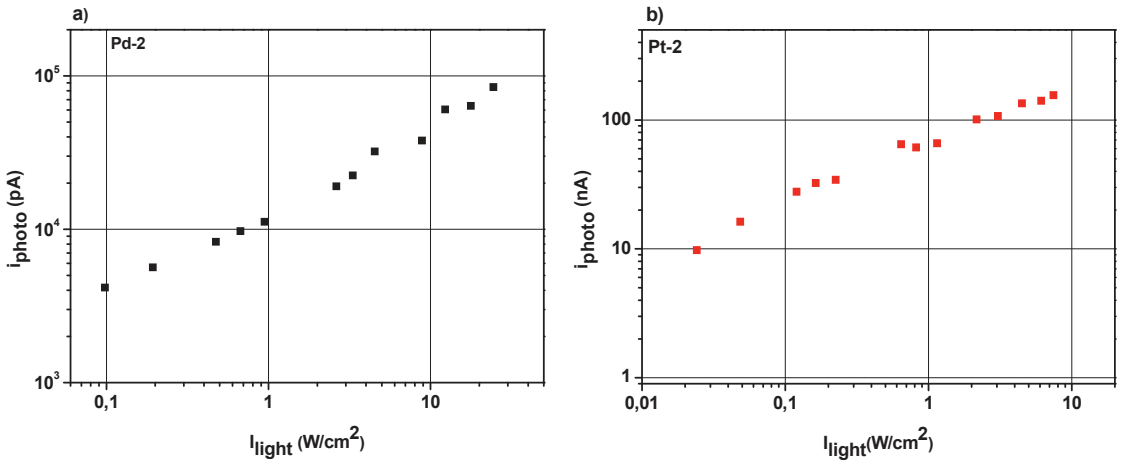


*Figure 2.22- Photocurrent vs light intensity for a) Pd-2 and b) Pt-2 films.*

The photocurrent measured for both materials is linear whit the square root of the light intensity. This dependence is consistent with a bi-molecular recombination as a factor dominating the current decay[40b]. The photoconductivity of these polymers is several orders of magnitude lower than in silicon[61] and in amorphous inorganic materials[62], as usually observed for organic materials, which exhibit lower charge mobility and photogeneration efficiency. At the same time, the performances of the presented electropolymerized films are comparable to that of other semiconducting polymers used in the fabrication of bulk heterojunction solar cells[63].

### 2.6.5 Hole mobility in electropolymerized thin films

In addition to photoconductivity, charge mobility is another important characteristic of organic semiconductors to be used in electronic devices. TPA-derived compounds are known to exhibit good hole transporting properties[40]. The hole mobility of the electropolimerized thin films of both complexes (thickness range 30-100 nm) was measured using the SCLC method, with one ITO and one gold electrode in each cell.

Examples of the current-voltage curves obtained for these samples are shown in Figure 2.23. Charge injection into the sample, a requirement for the creation of the SCLC regime, was obtained from both Au and ITO electrodes; no significant differences where observed by changing the polarity of the applied field.

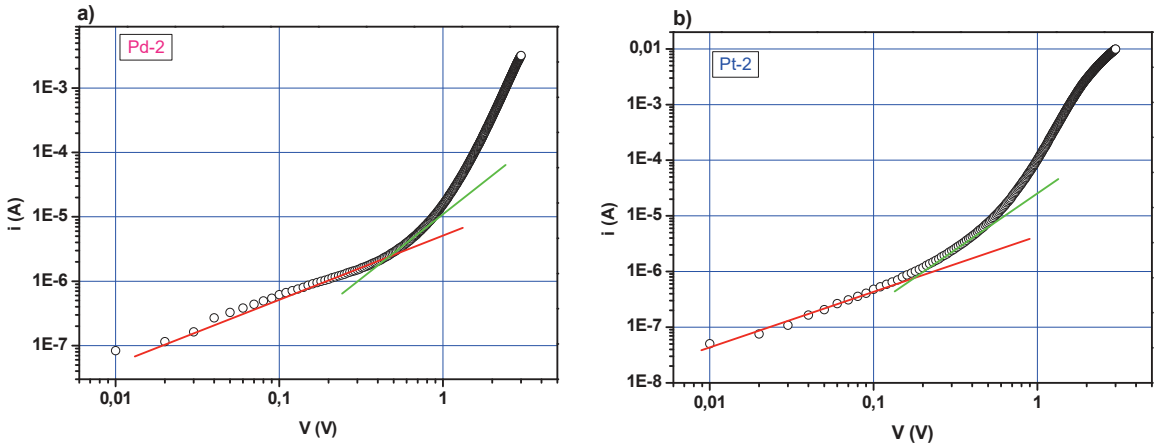


*Figure 2.23- Typical SCLC curves obtained during mobility measurements for a) Pd-2 and b) Pt-2 electropolymerized films of about 60 nm thickness; Au was the injecting electrode.*

As shown in Figure 2.23, in both cases the SCLC regime is not reached clearly, but order of magnitude values for hole mobility can be estimated and are summarized in Table 2.4:

| *complex* | *hole mobility* ($cm^2V^{-1}s^{-1}$) | $V_T^{exp} / V_T^{cal}$ |
|---|---|---|
| *Pd-2* | $2 \cdot 10^{-11}$ | 1 |
| *Pt-2* | $3 \cdot 10^{-11}$ | 0.98 |

*Table 2.4- Hole mobility determined by SCLC measurements.*

No difference in mobility between electropolymerized Pd-2and Pt-2was observed. As the SCLC technique is sensitive to the effectiveness of charge injection from the electrodes, this should be considered as a lower limit for the hole mobility in these materials. Indeed, as already evident from photoconductivity measurements, in these thin films the interfaces

play a major role in charge transport. Trapping phenomena at the interface could be at the origin of a reduced charge injection, limiting the set-up of the SCLC regime and the measured hole mobility. However, considering that photoconductivity increases by orders of magnitude by using thicker samples, it is more probable that the interface traps are a key factor determining the experimental result.

### 2.6.6 Photoconductive electropolymerized organo-metallic thin films as ABL

Electropolymerized thin films of the Pd-2 complex were used as an anode buffer layer to prepare solar cells (operating in the standard configuration) in combination with the P3HT:$PC_{60}BM$ active layer, trying to replace the PEDOT:PSS layer usually employed in these devices. Only the Palladium-containing polymers have been used since, comparing to its Platinum-containing analogous, this monomeric complex is characterized by a more controllable electrochemical synthesis, leading to a preparation of more homogeneous, defect-free and reproducible films. The schematic representation for the structure of solar cells and the corresponding energy level diagram are shown in Figures 2.24 and 2.25, respectively.

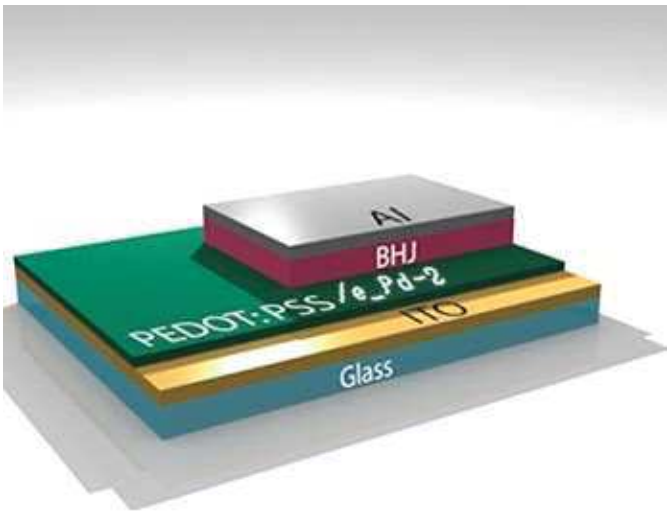


*Figure 2.24- Representation of the structure of the solar cells under study.*

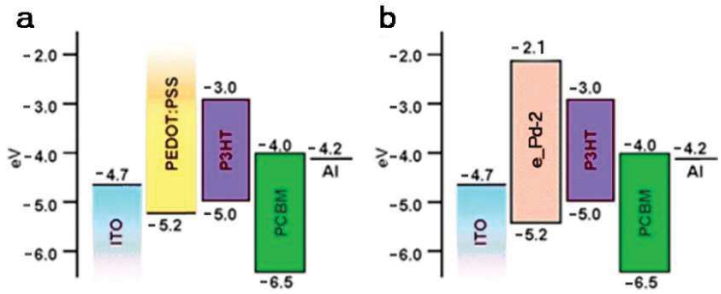


*Figure 2.25- Energy level diagram for the materials used in construction of the BHJ solar cells, determined either through experimental characterization or from literature[64].*

From an energetic point-of-view, the electropolymerized Pd-2 films could be certainly used as a buffer layer onto the ITO electrode. As shown in Figure 2.25, the HOMO level of these thin films has the same value as that of PEDOT:PSS, commonly used as a layer for collecting the holes generated in the active layer. Due to their LUMO level around – 2.1 eV, these electropolymerized compounds could effectively act also as electron blocking layer to prevent charge recombination near the hole collecting electrode. Finally, TPA-containing polymers are hole-transporting materials[40]. The solar device working parameters, under standard light irradiation conditions (AM 1.5G; 100 mV/cm$^2$), are reported in Table 2.5 while the corresponding J-V curves are shown in Figure 2.26.

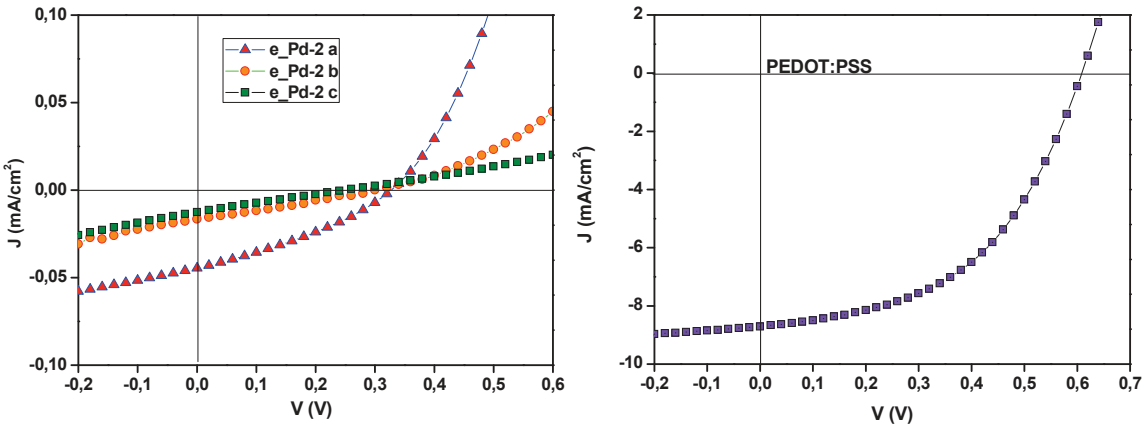


*Figure 2.26- J-V curves for the all studied devices.*

| Type of ABL | ABL thickness (nm) | PCE (%) | FF | Voc (V) | Jsc ($mA/cm^2$) |
|---|---|---|---|---|---|
| PEDOT:PSS | **30** | **2.2021** | **0.50** | **0.60** | **- 7.290** |
| e_Pd-2 a | **19** | **0.0048** | **0.33** | **0.32** | **- 0.045** |
| e_Pd-2 b | **28** | **0.0014** | **0.28** | **0.30** | **- 0.017** |
| e_Pd-2 c | **32** | **0.0008** | **0.25** | **0.26** | **- 0.013** |

*Table 2.5- Figures of merit of the studied solar cells.*

These devices were prepared with the same photoactive P3HT:$PC_{60}BM$ blend, prepared and treated in all cases with the same procedures (see experimental methods chapter for details). The figures of merit of the resulting devices are quite disappointing. The parameter that presents the highest worsening respect to the reference system is the short-circuit current. This could be due to:

- A lower thickness of the active layer due to a lower affinity of the P3HT:$PC_{60}BM$ with the underlying layer during spin coating deposition. Indeed, the properties of the buffer layers are very different for PEDOT:PSS and for the electropolymerized films. The first difference derives from the different roughness of the ABL used. PEDOT:PSS film prepared by spin coating are known to present a very smooth and homogeneous surface[65], while, as already said, the RMS roughness of the electropolymerized films mainly depends, apart from the thickness, on the potential scan rate used during electrodeposition. To obtain films with the lowest roughness as possible, all electropolymerization have been conducted at very low monomer concentration ($5 \cdot 10^{-5}$ M in DCM) at 300 mV/s; the different thicknesses (desired maximum thickness around 35/40 nm) were due to the different number of cycles performed. All these films present similar roughnesses (around 5 nm). More important than roughness, the electropolymerized films present wettability problems for the solution (in chlorobenzene) of the active species. This problem surely leads to a different thickness for the active blend deposited onto these new polymers, comparing with the optimized thickness used for PEDOT:PSS devices (about 70 nm on electropolymerized thin films *vs.* 120 nm on PEDOT:PSS). Moreover, also a different

morphology for the active layer blend could be induced bythe different polarity, roughness and homogeneity of the underlying layer, leading to the lower FF presented by devices realized with the electropolymerized films;

- A lower conductivity of the electropolymerized thin films. Electropolymerized thin films show a very low hole mobility. PEDOT:PSS films, instead, are characterized by very high conductivity, both in lateral (sheet resistance) and vertical ("bulk" resistance)[14,66]. As previously mentioned, the hole mobility in these thin systems could be dramatically affected by recombination and trapping processes at the interfaces with the electrodes, leading to an problematic measurement of this value. By contrast, measurements on thicker samples (by which "bulk" mobility of these materials could be obtained) are not simple to perform and give irreproducible results due to the experimental difficulties to obtain very smooth thicker films.
- A higher series resistance at the ITO interface, due to the above mentioned phenomena present at this interface, leading to an increase in resistance to charge flow to the electrode;
- A lower light transmittance from the electropolymerized thin film compared to PEDOT:PSS. In this way, a lower amount of light can reach the active layer and be absorbed, leading to a decrease in $J_{sc}$ (see Figure 2.27).

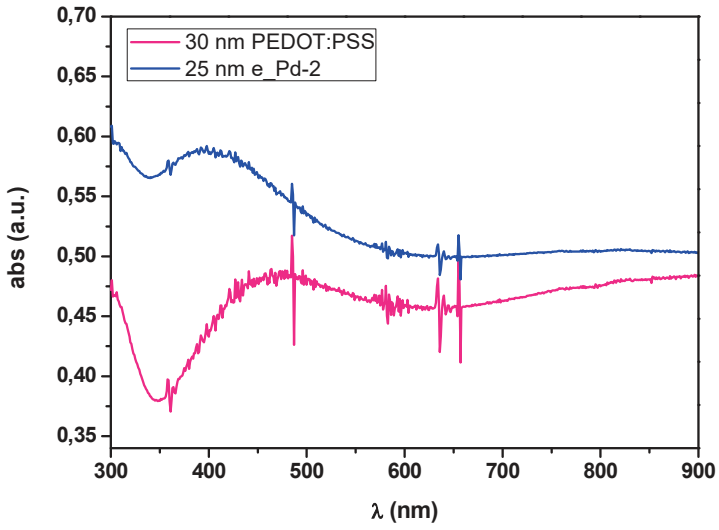


*Figure 2.27- Absorption spectra of PEDOT.PSS and e_Pd-2 film of comparable thickness.*

Also, the open circuit voltage shows a decrease with the introduction of these materials as ABL. In organic solar devices, $V_{oc}$ is found to be proportional to the difference between the donor HOMO and the acceptor LUMO[3] (if an ideal Ohmic contact with the electrode is realized). This means that in the solar cell with electropolymerized complexes, although there is a good matching with the energetic levels of the P3HT, the $V_{oc}$ could be limited by the recombination processes that may occur at the A/D interface due to the poor hole extraction from the $HOMO_D$ to the electropolymerized film HOMO.

## 2.7 CONCLUSIONS

In this chapter, results on the use of novel photoconductive, electropolymerized metallo-polymer films as anode buffer layers in BHJ solar cells were presented. These thin films were prepared from the corresponding monomeric organometallic complexes through the electropolymerization of the TPA group, grafted into the H(O^N) ancillary ligand. By using electropolymerization, the polymer formation and its deposition occur simultaneously, avoiding solubility drawbacks and providing controllable film thickness and surface coverage, especially for very thin electrodeposited films. Both the starting complexes and the electrodeposited polymers are photoconductors, and the photoresponsivity (*i.e*. the photoconductivity per Watt of incident power) of electrodeposited films is one to two orders of magnitude higher than that of the corresponding complexes, indicating that the electropolymerization reaction leads to an improvement of the photogeneration efficiency. By contrast, the hole mobility of these electropolymerized thin films is difficult to determinate with the SCLC methods, at least in part due to the unfavorable effect of trapping sites at the interfaces with the electrodes, that unfortunately is a predominant feature (with respect to the bulk conductivity) in films of the needed thickness for PV applications, *i.e.*~ 5-50 nm. Anyway, these results show that electropolymerization could represent a useful approach for preparing thin films of electro-active species, such as the cyclometallated complexes studied in this work, characterized by thickness and morphology dependent on the experimental conditions. Noteworthy, this technique could be easily used for PV applications where an ITO-electrode pattern is usually employed in device construction. Indeed, one of the most important features of this electrochemical deposition method consists in the possibility to follow a pre-set electrode pattern, important detail in device preparation that cannot be achieved by using spin coating or other common thin film solution deposition techniques. Moreover, both the starting organometallic complexes and the polymeric thin films are photoconductors, important feature where the increase in conductivity, reached upon light illumination, could represent an advantageous issue for PV applications.

The first solar devices containing these organometallic polymers as ABL have shown wettability (respect to the active layer used) and resistivity problems, leading to the poor

$J_{sc}$, FF and $V_{oc}$. Further work is necessary both on the preparation of electropolymerized thin films (*i.e.* trying to use thinner than 10 nm films for enhance charge collection to the electrode for avoid resistivity problems) and on the optimization of the above active layer formation. However, at the same time, these preliminary results confirm that electropolymerization of such photoconductive complexes can actually represent a useful procedure for the preparation of high quality thin films for optoelectronic and energetic application.

## 2.8 BIBLIOGRAPHY

**[1]** W. Hu, *SPIE Newsroom*, **2013**, DOI: 10.1117/2.1201301.004665.
**[2]** A. Kokil, K. Yang, J. Kumar, *J. Pol. Sci. part B: Pol. Phys*., **2012**, 50, 1130.
**[3]** C.W. Schlenker, M.E. Thompson, *Chem. Comm*., **2011**, 47, 3702.
**[4]a)** S. Wen, C. Wang, P. Ma, G. Wang, W. Dong, Y. Gao, S. Ruan, *J. Phys. Chem. C*, **2015**, 119, 20817;
**b)**A.K.K. Kyaw, D.H Wang, D. Wynands, J. Zhang, T.-Q. Nguyen, G.C. Bazan, A.J. Heeger, *Nanolett*., **2013**, 13, 3796.
**[5]** Z. Yin, J. Wei, Q. Zheng, *Adv. Sci*., **2016**, 3, 1500362.
**[6]** N.K. Elumalai, C. Vijila, R. Jose, A. Uddin, S. Ramakrishna, *Mater. Renew. Sustain. Ener*., **2015**, 4:11.
**[7]** S.-H. Zhao, J.-K. Chang, J.-J. Fang, H.-W. Tsai, I.-H. Liu, W.-H. Tseng, T.-W. Pi, M.-H. Chen, *Thin Solid Films*, **2013,** 545, 361.
**[8]a)**S. Das, J. Joslin, T.L. Alford, *Sol. Ener. Mater. Sol. Cells*, **2014**, 124, 98;
**b)** Z.H. Khan, *Cogent Engin*., **2016**, 3, 1170097;
**c)** A. Muthurasu, V. Ganesh, *J. Colloid Interface Sci*., **2012**, 374, 241
**[9]a)** J. Han, Y. Chen, W. Chen, C. Yu, X. Song, F. Li, Y. Wang, *ACS Appl. Mater. Interfaces*, **2016**, 8, 32823;
**b)**B.A.E. Courtright, S.A. Jenekhe, *ACS Appl. Mater. Interfaces*, **2015**, 7, 26167.
**[10]** A. Mantovani Nardes, M. Kemerink, R.A.J. Janssen, J.A.M. Bastiaanesn, N.M.M. Kiggen, B.M.W. Langeveld, A.J.J.M. van Breemen, M.M. de Kok*, Adv. Mater*., **2007**, 19, 1196.
**[12]** G. Heywang, F. Jonas, *Adv. Mater*., **1992**, 4, 116.
**[11]** S. Kirchmeyer, K. Reuter*, J. Mater. Chem*., **2005**, 15, 2077.
**[13]** L.B. Groenendaal, F. Jonas, D. Freitag, H. Pielartzik, J.R. Reynolds, *Adv. Mater*., **2000**, 12, 481.
**[14]a)** A.M. Nardes, M. Kemerink, M.M. de Kok, E. Vinkem, K. Maturova, R.A.J. Janssen, *Org. Electr*., **2008**, 9, 727;
**b)** X. Crispin, F.L.E. Jakobsson, A. Crispin, P.C.M. Grim, P. Andersson, A. Volodin, C. van Haesendonek, M. Von der Auweraer, W.R. Salanick, M. Berggren, *Chem. Mater*., **2006**, 18, 4354.
**[15]** T.-R. Chou, S.-H. Chen, Y.-T. Chiang, Y.-T. Lin, C.-Y. Chao, *J. Mater. Chem. C*, **2015**, 3, 3760.
**[16]** A. Elschmer, S. Kirchneyer, W. Lovenich, U. merker, K. Reuter, *PEDOT: Principle and application of an intrinsically conductive polymer*, **2011**, CRC Press, Taylor and Francis Group.
**[17]** Y. Liao, Q. Lu, Y. Fan, X. Liu, *Appl. Phys. Lett*., **2011**, 99, 023302.
**[18]a)** Y.J. Xing, M.F. Qian, J.F. Qin, G.M. Zhang, *J. Vac. Sci. Technol. B*, **2014**, 32, 02B101;
**b)** Y.-J. Xing, M.-F. Quian, D.-Z. Guo, G.-M. Zhang, *Chin. Phys. B*, **2014**, 23, 038504.
**[19]** A. Savva, M. Neophyton, C. Koutsides, K. Kalli, S.A. Choulis, *Org. Electr*., **2013**, 14, 3123.
**[20]** F.J. Lim, K. Ananthanarayanan, J. Luther, G.W. Ho, *J. Mater. Chem*., **2012**, 22, 25057.
**[21]a)** K. Kawano, R. Pacios, D. Poplavskyy, J. Nelson, D.D.C. Bradley, J. R. Durrant, *Sol. Ener. Mater. Sol. Cells*, **2006**, 90, 3520;
**b)** J.-F. Wei, Q.-L. Wu, Y.-X. Lin, Y. Zhang, *ECS J. Solid State Sci. Technol*., **2016**, 5, Q171.
**[22]** 1) T. Unuma, M. Yoshikawa, A. Nakamura, M. Kishida, *Appl. Phys. Express*, **2016,** 9, 051601;

**[23]** M.P. de Jon, L.J. Van IJzendooorn, M.J.A. de Voigt, *Appl. Phys. Lett*., **2000**, 77, 2255.
**[24]a)** J.J. Jasieniak, J. Scifter, J. Jo, T. Mates, A.J. Heeger, *Adv. Funct. Mater*., **2012**, 22, 2594;
**b)** U. Kwan, B.-G. Kim, D.C. Nguyen, J.-H. Park, N.Y. Ha, S.-J. Kim, S.H. Ko, S. Lee, D. Lee, H.J. Park, *Sci. Rep.*, **2016**, 6, 30759;
**c)** F. Ongul, *Opt. Mater*., **2015**, 50, 244;
**d)** F. Guillain, D. Tsikritzis, G. Skoulakakis, S. Kennou, G. Wantz, L. Vignau, *Sol. Ener. Mater. Sol. Cells*, **2014**, 122, 251.
**[25]a)** L. Yang, S.K. Sontag, T.W. LaJoie, W. Li, N.E. Huddleston, J. Locklin, W. You, *ACS Appl. Mater. Interfaces*, **2012**, 4, 5069;
**b)** E. Andreoli, K.-S. Liao, A. Haldar, N.J. Alley, S.A. Curran, *Synth. Metals*, **2013**, 185, 71;
**c)** S. Bom, M. Ortel, V. Wagner, *Phys. Status Solidi A*, **2014**, 211, 1634;
**d)** D. Triantu, S. Soulis, S. Koureli, A. De Sio, E. von Hauff, *J. Appl. Pol. Sci*., **2013**, 585.
**[26]** J. Heinze, B.A. Frontana-Uribe, S. Ludwings, *Chem. Rev.,* **2010**, 110, 4724.
**[27]** R. Kumar, S. Singh, B.C. Yadav, *International Adv. Research J. Sci. Engin. Technol*., **2015**, 2, 110.
**[28]a)** A.H. Saïd, C. Dridi, S. Roudesly, F. Matoussi Mhalla, *Eur. Pol. J*., **2000**, 36, 909;
**b)** C. Eiras, M. Foschini, J.C. Soores, D. Gonçalves*, Chem. Papers*, **2015**, 69, 958.
**[29]a)** B. Parakhonskiy, D. Shchukin, *Langmuir*, **2015**, 31, 9214;
**b)** R. Gupta, K. Jayachandran, J.S. Gamare, B. Rajeshwari, S.K. Gupta, J.V. Kamat, *J. Nanopart*., **2015**, ID149406.
**[30]a)** T. Wang, W. Wang, Y. Dai, H. Zhang, Z. Shen, Y. Chen, X. Hu, *Russian J. Electrochem*., **2015**, 51,743;
**b)** C.T. Pereira de Silva, V.L. Kipfer, G. Reinaldo de Silva, M Pereira Moisés, M.A. Gonçalves Trindade, N.L. de Campos Domingues, A. Wellington Rinaldi, *Int. J. Electrochem. Sci*., **2016**, 11, 5380.
**[31]a)** J Roncali, *Chem. Rev*., **1992**, 92, 711;
**b)** J. Simitzis, D. Trintau, S. Soulis, *J. Appl. Pol. Sci*., **2010**, 118, 1494.
**[32]** M.M. Gvozdenović, B.Z. Jugović, J.S. Stevanović, B.N. Grgu, *Hem. Ind*., **2014**, 68, 673.
**[33]** G.V. Govindaraju, G.P. Wheeler, D. Lee, K.-S. Choi*, Chem. Mater*, **2017**, 29, 355.
**[34]** V. Tsakova, A. Milchev, J.W. Schultze, *J. Electroanal. Chem*., **1993**, 346, 85.
**[35]a)** H.D. Abruna, P. Denisevich, M. Umaňa, T.J. Meyer, R.W. Murray, *J. Am. Chem. Soc*., **1981**, 103, 1;
**b)** H.-J- Nie, J.-Y. Shao, J. Wu, J. Yao, Y.-W. Zhong, *Organometallics*, **2012**, 31, 6952;
**c)** S.-C. Huang, C.-Y. Lin, *Chem. Comm*., **2015**, 51, 519:
**d)** M.M Gvozdenović, B.Z. Jugović, J.S. Stevanović, T.L. Trišović, B.N. Grgu, *Electropolymerization; chapter 4: Electrochemical Polymerization of Amine*, **2011**, Pubisher: InTech, ISBN 978-953-307-693-5;
**[36]** G.G. Wallace, R.P. Teasdale, G.M. Spinks, L.A.P. Kane-Magure, *Conductive Electroactive Polymers*, 3rd Ed, **2009**, Taylor and Francis Group.
**[37]** K.Y. Chiu, T.X. Su, J.H. Li, T.-H. Lin, G.-S. Liou, S.-H. Cheng*, J. Electroanal. Chem*., **2005**, 575, 95.
**[38]** E.T. Seo, R.F. Nelson, J.M. Fritsch, L.S. Marcoux, D.W. Leedy, R.N. Adams, *J. Am. Chem. Soc*., **1966**, 88, 3498.
**[39]** R.F. Nelson, R.N. Adams, *J. Am. Chem. Soc*., **1968**, 90, 3925.
**[40]a)** N. Tsutsunu, *Pol.J*., **2016**, 48, 571;
**b)** J. Kalinowski, K. Szybowska, *Org. Electr*., **2008**, 9, 1032;

**c)** E. Bellmann, S.E. Shaheen, S. Thayumanavan, S. Barlow, R.H. Grubbs, R.S. Marder, B. Kippelen, N. Peyghambarian, *Chem. Mater*., **1998**, 10, 1668;
**d)** J. Ha, H.C. Lee, S.-H. Lee, N. Kimura, H. Sato, *Pol. J*., **2004**, 36, 219;
**e)** D.C. Santra, S. Mandal, S. Malik, *RCS Adv*., **2016**, 6, 81597;
**f)** L. Ji, Y. Dai, S. Yan, X. Lv, C. Su, L. Xu, Y. Lv, M. Ouyang, Z. Chen, C. Zhang, *Sci. Rep.*, **2016**, 6, 30068;
**g)** M. Thelakkat, *Macromol. Mater. Engin*., **2002**, 287, 442;
**h)** H.-J. Yen, G.-S. Liou, *Pol. Chem*., **2012**, 3, 255;
**i)** A. Iwan, D. Sek, *Prog. Pol. Sci*., **2011**, 36, 1277.

**[41]a)** M.K. Leung, M.-Y. Chou, Y.O. Su, C.L. Chiang, H.-L- Chen, C.F. Yang, C.-C. Yang, C.-C. Lin, H.-T. Chen, *Org. Lett*, **2003**, 5, 839;
**b)** T. Yasuda, *IOP Conference Series, Mater. Sci. Engin*., **2014**, 122, 251;
**c)** J.M. Campiňa, J. Electrochem. Soc., 2015, 162, H142;
**d)** A.M. Namespetra, A.D. Hendsbee, G.C. Welch, I.G. Hill, *Canadian J. Chem*., **2015**, R1, 0427.

**[42]a)** N. Camaioni, R. Po, *J. Phys. Chem. Lett*., **2013**, 14, 1821;
**b)**D. Black, I. Salaoru, S. Paul, *EPJ Photovol*., **2014**, 5, 50403.

**[43]** H. Dong, H. Zhu, Q. Meng, X. Gong, W. Hu, *Chem. Soc. Rev*., **2012**, 41, 1754.

**[44]** T. Cazati, L.F. Santos, F.T. Reis, R.M. Faria, *Appl. Phys A*, **2012**, 108, 545.

**[45]** D.S. Weiss, M. Abkowitz, *Chem. Rev*., **2010**, 110, 479.

**[46]** A Ionescu, N. Godbert, A. Crispini, R. Termine, A. Golemme, M. Ghedini, *J. Mater. Chem*., **2012**, 22, 23617.

**[47]** R.P. Kingsborough, T.M. Swager, *J. Am. Chem. Soc*., **1999**, 121, 8825.

**[48]a)** M Ghedini, I. Aiello, A. Crispini, A. Golemme, M. La Deda, D. Pucci, *Coord. Chem. Rev*., **2006**, 250, 1373;
**b)** N. Godbert, D. Dattilo, R. Termine, I Aiello, A. Bellusci, A. Crispini, A. Golemme, M. Ghedini, *Chem. Asian J*., **2009**, 4, 1141;
**c)** A. Ionescu, I. Aiello, M. La Deda, A. Crispini, M. Ghedini, M.P. De Santo, N. Godbert, *ACS Appl. Mater. Interfaces*, **2016**, 8, 12272.

**[49]** M Ghedini, A. Golemme, I. Aiello, N. Godbert, R. Termine, A. Crispini, M. La Deda, F. Lelj, M. Amati, S. Belviso, *J. Mater. Chem*., **2011**, 21, 13434.

**[50]** U.K. Pandey, R. Termine, A. Ionescu, N. Godbert, M.P. De Santo, M. Ghedini, A. Golemme, *Mol. Cryst. Liq. Cryst*., **2012**, 558, 148.

**[51]a)** L. Niam, W. Zhang, N. Zhu, L.Liu, Z. Xie, H. Wu, F. Würthner, Y. Ma, *J. Am. Chem. Soc*., **2015**, 137, 6995;
**b)** L. Niam, Z. Chen, S. Herbst, Q. Li, C. Yu, X. Jiang, H. Dong, F. Li, L Liu, F. Würthner, J. Chen, Z. Xie, Y. Ma, *Adv. Mater*., **2016**, 28, 7521.

**[52]** N. Cocherel, P. Leriche, E. Ripaud, N. Galleo-Planas, P. Frère, J. Roncali, *New J. Chem*., **2009**, 33, 801.

**[53]** D. Qiu, Q. Zhao, X. Bao, K. Liu, H. Wang, Y. Guo, L. Zhang, J. Zeng, H. Wang, *Inorg. Chem. Comm*., **2011**, 14, 296.

**[54]** E.C. Constable, A.M.W. Cargill Thompson, T.A. Leese, D.G.F. Reese, D.A. Tocher, *Inorg. Chim. Acta*, **1991**, 182, 93.

**[55]** N. Godbert, T Pugliese, I. Aiello, I. Bellusci, A. Crispini, A. Ghedini, *Eur. J. Inorg. Chem*., **2007**, 5105.

**[58]** A.J. Bard, L.R. Faulkner, *Electrochemical Methods. Fundamentals and Application*, **2001**, Wiley, New York.
**[59]** S. Sezgin, M. Ates, E.A. Parlak, A.S. Sarac, *Int. J. Electrochem. Sci*., **2012**, 7, 1093.
**[56]** T. Lana-Villarreal, J.M. Campiňa, N. Guijarro, R. Gòmez, *Phys. Chem. Chem. Phys*., **2011**, 13, 4013.
**[57]** K.L Brown, S.B. Gray, *Int. J. Chem*., **2010**, 2, 3.
**[60]** H. Bässler, *Phys Status Solidi B*, **1993**, 175, 15.
**[61]** A. Shah, *EPFL Press*, **2010**, Lousanne, Switzerland, pp. 58-61.
**[62]** R.K. Pal, S. Yadav, A.K. Aghinotri, D. Kumar, A. Kumar*, J. Non-oxide Glasses*, **2009**, 1, 285.
**[63]** M Tong, S. Cho, J.T. Rogers, K. Schmidt, B.B.Y. Hsu, D. Moses, R.C. Coffin, E.J. Kramer, G.C. Bazan, A.J. Heeger, *Adv. Funct. Mater*., **2010**, 20, 3959.
**[64]** M.D. Irwin, D. B. Buchholz, A.W. Hains, R.P.H. Chang, T.J. Marks, *PNAS*, **2008**, 105, 2783.
**[65]**J. Huang, P.F. Miller, J.C de Mello, A.J. de Mello, D.D.C. Bradley, *Synth. Met*., **2003**, 139, 569.
**[66]**A. Fallahzadeh, J. Saghaei, M.H. Yousefi, *Appl. Surface Sci*., **2014**, 320, 895.

# CHAPTER 3:
# TOWARDS PLASMONIC METAMATERIAL STRUCTURES FOR EFFICIENCY ENHANCEMENT OF OSCs

## 3.1 INTRODUCTION

In the previous chapters, it was shown that improvements in device efficiency can be achieved through a combination of factors, such as an accurate engineering of the photoactive materials (*i.e.* for determining its absorption and solubility features), the choice of the processing conditions to obtain the suitable nanomorphology for the active layer (*i.e.* used solvent, post-fabrication treatments like solvent/temperature annealing), or the presence of buffer layers in the OPV device architecture. All these features play a crucial role in determining the device efficiency and it is very difficult to decouple them and to reach simultaneous optimization of each of these processes. The major bottleneck for OPV to achieve higher efficiency lies in the trade-off between the light absorption depth (usually hundreds of nanometers in organic materials), the low exciton diffusion length (in the range of about 10 nm[1]) and the low charge mobility, leading to the use of thin photo-active films with a limited absorption efficiency. To overcome this intrinsic limit, strategies for concentrating, trapping or tuning the light inside the device seem to be an appealing approach to enhance the light absorption of the active layer (improve its optical thickness) without increasing its physical thickness and perturbing its charge transport properties.

## 3.2 LIGHT MANAGING IN OSCs

In the past years, different approaches for light managing in solar cells have been proposed, such as: using interlayers as optical spacers[2], collector mirrors and lenses, luminescent concentrators[3] or up-converter[4], anti-reflection coatings[5] and surface plasmon resonators[6]. Mirrors and concentrating lenses collect the light through the

physical principles of reflection (for mirrors[7]) or refraction (for lenses[8]) on curved surfaces, focusing the light onto a smaller area. In this way, it is possible to increase the power density incident on the solar cell in a smaller device area, decreasing the surface coverage of the device, with significant material cost reduction. In luminescent concentrators, the light is both concentrated and wavelength-tuned. In this case, the incident light passes through a layer formed by a matrix containing luminescent molecules. These molecules absorb the light which would not be absorbed by the adjacent active layer and re-emit it at a longer wavelength, in the range of the absorption spectrum of the active layer. Since organic solar cells consist of a stack of several thin layers, a certain percentage of the light is always lost by reflection at the interfaces (optical losses) and from the glass substrates on which devices are usually prepared. A possibility to reduce these losses involves the use of anti-reflection coatings. Numerous strategies and materials have been proposed to this aim, like "moth-eye"[9] and several periodic structures[5].

In addition to such techniques, the use of Surface Plasmon Resonance (SPR) effects has recently attracted much attention thanks to the possibility of improving light absorption and efficiency of OPV devices, as discussed below.

## 3.3 PLASMONIC IN PHOTOVOLTAICS

A relatively new technique for achieving light trapping consists in using metallic nanostructures that support Surface Plasmons (SPs). A surface plasmon is a collective excitation of conduction electrons at the interface between a metal (or a highly doped semiconductor[10]) and a dielectric (or a semiconductor). By an accurate engineering of these nanostructures both Localized Surface Plasmons (LSPs) and Surface Plasmon Polaritons (SPPs) could be obtained and used to concentrate and "fold" the light into the semiconductor thin layer, thereby increasing its absorption.

Currently, plasmonic structures integrated in OSC architectures involve the use of metallic nanoparticles (NPs) that could have a double effect, as shown in Figure 3.1. First, they can be used as sub-wavelength scattering elements to trap the light into the semiconductor layer, increasing the light optical path inside this active layer. Indeed, in contrast to light scattering in a homogeneous medium, when the NPs are located near an

interface between two different media light will preferentially scatter into the material having the larger permittivity. Through multiple and high-angle scattering, the overall optical path length will effectively increase, thereby trapping the photons in the device and enhance their absorption. Second, metallic NPs can be used as sub-wavelength antennas in which the high plasmonic near-field – generated in their closeness – could increase the absorption cross-section in the semiconductor slab. This enhanced near-field induced by the SPs around the NPs, can increase the absorption efficiency because the light absorption is proportional to the intensity of the electromagnetic field[11]. However, the construction of such a device is not simple because the metal NPs tend to undergo phase separation from the organic active materials, to disturb the formation of the optimized nanomorphology for a given active system and, furthermore, the inclusion of NPs might affect the device's electrical properties and decrease the carrier collection efficiency.

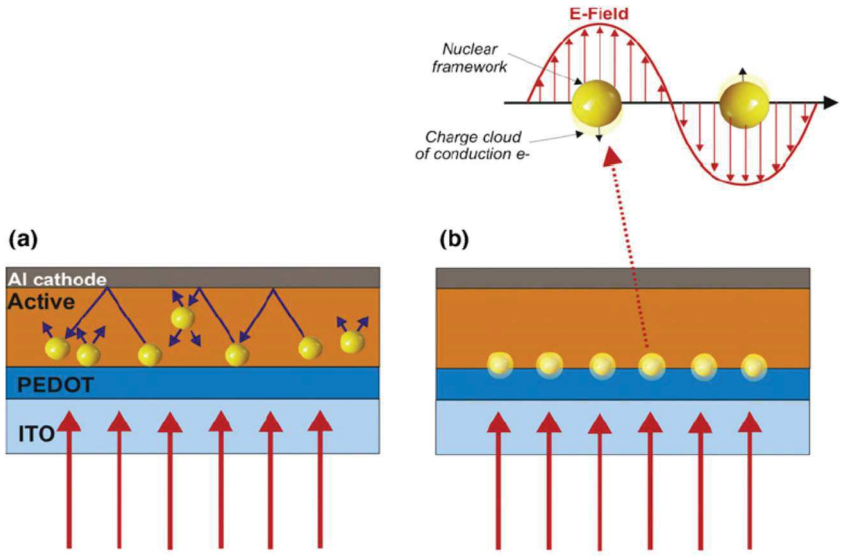


*Figure 3.1- Plasmonic effect of metal NPs: a) scattering for large diameter (> 50 nm) NPs inside the active layer and b) LSPR induced by small particle (diameter 5-20 nm)[12]*

Noble metal NPs are known to exhibit a strong plasmonic absorption band in the UV-Vis region, the same spectral range of the optical absorption band of the conjugated polymers used in the active layer of OSC. In the quasi-static limit and for NPs with dimension below

the wavelength of light, the scattering and absorption cross section are given by Equations 1 and 2, respectively[13]:

$$\sigma_{sc} = \frac{1}{6\pi}\left(\frac{2\pi}{\lambda}\right)^4 |a|^2 \quad (1)$$

$$\sigma_{abs} = \frac{2\pi}{\lambda}\mathrm{Im}[a] \quad (2)$$

where $a$ is the polarizability of the particle. For spherical NPs embedded in a semiconductor with permittivity $\varepsilon_d$, the polarizability is calculated from Equation 3:

$$a = 4\pi r^3 \frac{\varepsilon_m - \varepsilon_d}{\varepsilon_m + 2\varepsilon_d} \quad (3)$$

where $r$ is the radius of the nanoparticle, and $\varepsilon_m$ is the permittivity of the metal. When the relation $\varepsilon_m \approx -2\varepsilon_d$ is verified, the particle polarizability reaches a maximum together with the absorption cross-section. This condition is named Localized Surface Plasmon Resonance and its frequency depends on the size and shape of the NPs, on the NP material and on the optical constant of the dielectric medium. Usually, for solar cell applications, it is important to have $\sigma_{sc} >> \sigma_{abs}$; this is necessary to keep metallic losses low, because light absorbed in the metal will not contribute to useful carrier generation. From the above equations, metallic NPs could improve absorption behave as local-field enhancer or as scattering centers or both. For the smallest nanoparticles, with diameter in the range of 5-20 nm[12], the scattering cross-section is very low, so that $\sigma_{sc} + \sigma_{abs} \approx \sigma_{abs}$. For these nano-antennas, the absorption rate in the semiconductor must be larger than the reciprocal of the typical plasmon decay time to avoid dissipation of the absorbed energy into Ohmic damping in the metal[14]. As the particle size increases, $\sigma_{sc}$ grows also, and the plasmon resonance red shifts and broadens.

Another mechanism involving plasmonic effects consists in the excitation of propagating modes at the thin semiconductor/metal interface. These modes could be either Photonic Waveguide modes or Surface Plasmon Polaritons (SPPs). With this mechanism, light is "turned" by 90°with respect to the incidence direction and it could be partially absorbed by the semiconductor as the mode propagates, along the lateral direction of the solar cell, generating electron-hole pairs and increasing the photocurrent[15], as illustrated in Figure 3.2.

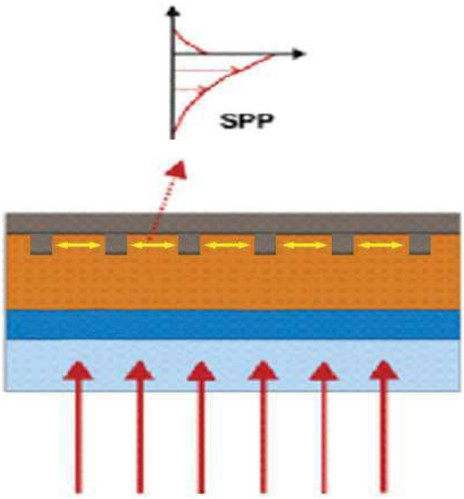


*Figure 3.2- Excitation of SPPs at the nanostructure/active layer interface[12].*

### 3.3.1 Surface Plasmon Polaritons

SPPs are collective oscillations of electromagnetic waves and free electrons at the interface of a metal and a dielectric or semiconductor material. The SPPs can propagate along the interface for a relatively long distance[16] but are strongly confined at the metal/dielectric or metal/semiconductor interface (*i.e.*do not propagate in the perpendicular direction). The intensity of these evanescent waves decays exponentially with the distance from the interface, faster in the metal than in the dielectric or

semiconductor material, according to the refractive index of this layer. Equation for describing Surface Plasmons Polaritons can be derived from a wave-like solution of the Maxwell's equations confined at an interface of two semi-infinite media. With the proper boundary conditions and considering only TM polarization (for TE polarization no solutions are possible), the SPPs dispersion relation (that is the frequency-dependent SPP wave-vector[17]) can be derived as:

$$k_{SPP} = \frac{\omega}{c}\sqrt{\varepsilon_m \varepsilon_d / \varepsilon_m + \varepsilon_d} \tag{4}$$

The real part of the complex dielectric constant of the metal ($\varepsilon_m$) has to be negative and with an absolute value greater than that of the dielectric material ($\varepsilon_d$) to make it possible for the SPPs to be excited at such an interface as evanescent waves; for metals this condition is fulfilled at frequencies below the bulk plasmon frequency $\omega_p$. From Equation 4, the interaction between the surface charge density and the electromagnetic field results in the momentum for the SPP modes being greater than that of a free-space photon of the same frequency ($k_{SPP} > \omega/c = k_0$ is the free-space photon wave-vector), as shown in Figure 3.3.

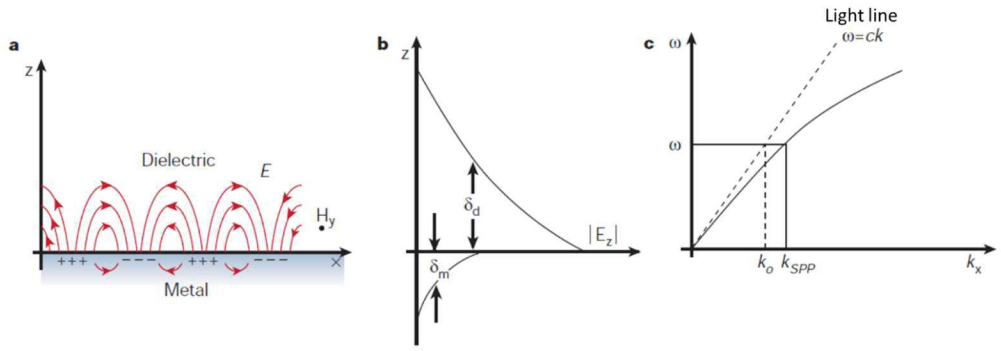


*Figure 3.3- Representation of a) electric field in a SPP; b) Variation of electric field according to an evanescent wave; c) Dispersion curve for a SPP and representation of the momentum mismatch with the free-space photons[17].*

Due to this momentum mismatch between light and SPPs of the same frequency, SPPs cannot be excited directly with incident light but a light-coupling structure has to be integrated in the metal/dielectric interface to overcome this momentum limitation.

Historically, there are four main techniques by which this momentum adjustment can be achieved:

- Use of prism-coupling and of the attenuated total reflection phenomenon with Kretschmann or Otto geometry[18];
- Use of a grating on the metal surface[19], usually employed in PV applications;
- Use of topological defects on the surface, such as sub-wavelength apertures, like slits and holes[20];
- Use of an inherently rough metallic surface that support SPPs[21]; this method, however, does not allow a fine control on the plasmon features in these thin film systems.

Another method exists to increase the magnitude of the incident light momentum, for a given frequency, at the metal-dielectric interface. In this case, conditions are adjusted for the dispersion curve of SPPs and the new "tuned" light line to cross each other[22]. Physically, this can be accomplished by passing the incident light through another medium, such as glass, on which the metal film is deposited. This concept can be illustrated for the system represented in Figure 3.4.

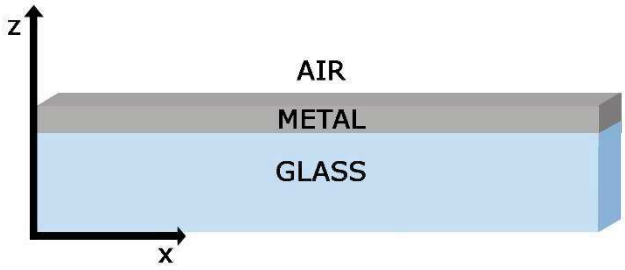


*Figure 3.4- Schematic representation of structure used to solve the momentum mismatch between photons in air and SPP.*

The glass has the effect of modifying the light wave-vector due to its refraction index ($N_{glass}$, which is assumed frequency-independent). After passing through the glass and for a sufficiently thin metal layer, some of the incident light could be transmitted up to the metal-air interface, where the SPPs could be excited, as shown in Figure 3.5, due to the intersection between the dispersion curve for the SPPs and the tuned light-line.

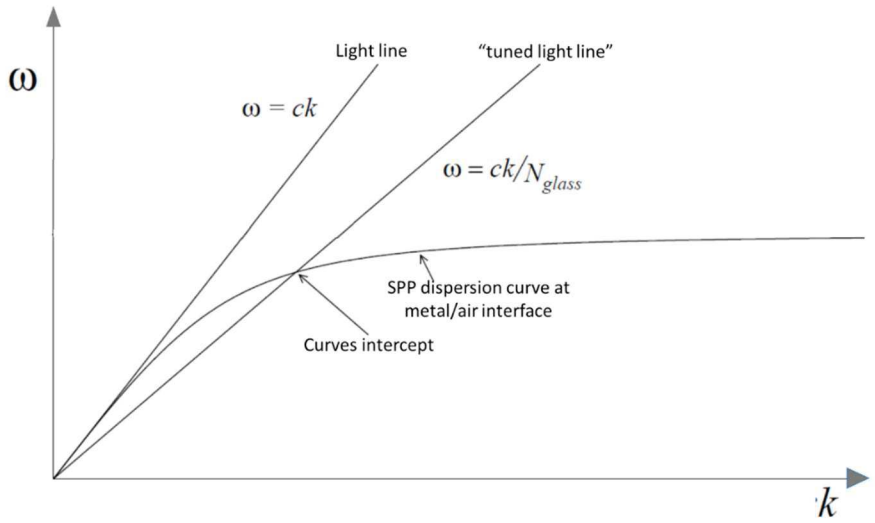


*Figure 3.5- Dispersion curves for SPP, photons in air and in glass.*

Even if Figure 3.5 qualitatively depicts the requirement for SPP excitation, it has to be noted that this condition is actually reached only for a proper angle of light incidence on glass (measured relative to the normal to the glass/metal interface).

### 3.3.2 Plasmon Hot-Carrier generation

Besides being efficient light-trapping components or near-field enhancers integrated in photovoltaic cells[6,12,23] to improve their absorption, metallic nanostructures that support Surface Plasmons (both LSPs and SPPs) can also directly convert the light into electrical energy by generating the so called "Hot-Electrons"[24]. This process is extremely different from the previously described phenomena because the light is absorbed directly by the metal rather than from the semiconductor. After the SPs excitation in these nanostructures, due to the absorption of light, surface plasmons decay (in the femto-second time scale) either radiatively or non-radiatively, through the creation of a "hot" electron-hole pair inside the metal; in sequence, emission of electrons can occur if the energy of the SPs exceeds the work-function of the metal, as illustrated in Figure 3.6[25].

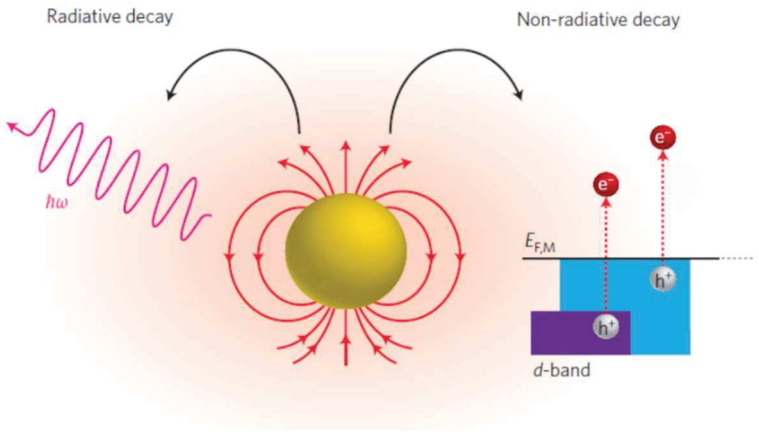


*Figure 3.6- Surface Plasmon can decay radiatively (emitting a photon) or non-radiatively (generating a hot-electron).*

The most accepted mechanism for describing this phenomenon is the Landau damping[26], a quantum mechanical process in which the plasmon-induced electric field represents a perturbation on the conduction electrons of the metal[27] and could induce their transition from occupied to unoccupied states. Some of these excited states could have enough energy to eject electrons above the metal Fermi level; the rest of the single-electron excited states relax non-radiatively through electron-electron and electron-phonon collision, producing heat[28]. Besides Landau damping, other plasmon-induced hot-electron transfer mechanism from metallic nanostructures have been proposed[26]. An efficient mechanism to collect these hot carriers for energy production, consists in forming a Schottky barrier with an appropriate semiconductor, as shown in Figure 3.7 for the collection of hot-electrons (with a n-type semiconductor) or of hot-holes (with a p-type semiconductor).

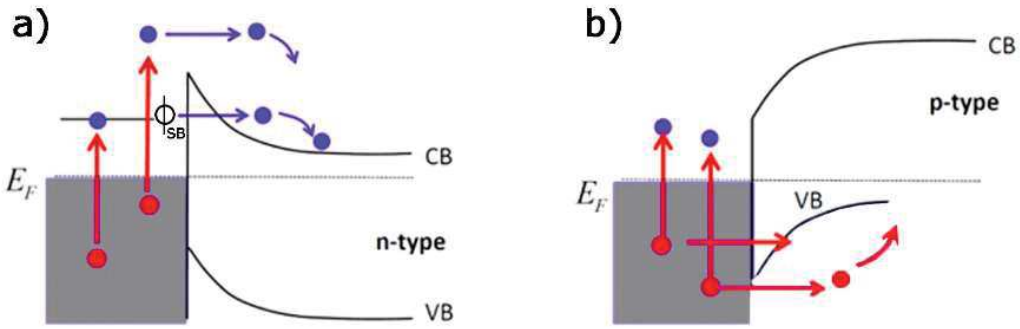


*Figure 3.7- Band diagrams of a metal/semiconductor junction with processes for hot-carrier generation and transport in a) n-type semiconductor for hot-electrons collection and b) p-type semiconductor for hot-holes collection.*

The following considerations apply for the former case. Hot-electrons with energies higher than the Schottky barriers will be injected in the conduction band of the neighbouring semiconductor, with an efficiency depending on their energy[29], on the semiconductor band-gap (which affects the height of the Schottky barrier measured respect to the Fermi level of the metal) and on the density of available states in the semiconductor conduction band[25]. In addition, electron tunneling across this barrier can take place, but with a lower probability[30]. In the past, this hot-carrier collection mechanism has been used to determine Schottky barrier heights in several metal/semiconductor systems where no plasmon-supporting structures had been integrated in. However, this process has not been considered for energy production due to its low efficiency[24a]. The high density of optical states in the vicinity of plasmonic structures[31] could enhance the hot-carrier generation and boost the energy conversion efficiency in this type of structures. Moreover, the energy need for these hot-electrons to overcome the Schottky barrier is usually smaller than the band-gap of the employed semiconductor; this consideration implies that in this device photocurrent generation is no longer limited to photon energies above the band-gap of the semiconductor, but rather to photon energies greater than the formed Schottky barrier[32]. After injection of hot-electrons into the semiconductor layer, the metallic plasmonic nanostructures remains positively-charged; for this reason, to support a current flow, a hole-transporting material - HTM - (or an electron-donor solution) has to be in contact with the metal[33] (but not with the semiconductor, to prevent detrimental charge recombination)[34] to transport these holes to the counter-electrode. In this way a faster hot-electrons injection and metal regeneration occur, improving the energy conversion efficiency resulting from this mechanism.

Most certainly, the composition, the geometry and the location of the plasmonic metallic nanostructures, respect to the semiconductor and the HTM, play a key role in determining the effectiveness of excitation of surface plasmons and their subsequent non-radiative decay with generation (and collection) of hot-carriers. Many studies on plasmonic hot-carrier generation are based on Au or Ag nanoparticles of different shapes and dimensions supported on titanium dioxide, involving the decay of LSPs[35,24c]. Indeed, $TiO_2$ is the most used material in these devices, being a wide band-gap semiconductor ($E_g$ = 3.3

eV) with a high density of states in its conduction band, due to the d-orbital nature of its conduction band.

So far, only few works support the hot-carrier generation using propagating surface plasmon-polaritons[24a,36].

## 3.4 MULTILAYER SYSTEMS AND METAMATERIALS

Another class of metallic nanostructures for light absorption enhancement are the multilayered systems. The simplest multilayer arrangement consists of alternating metal and dielectric layers in MIM or IMI configuration; in such systems, each M/D interface could support SPPs. When the separation among adjacent interfaces is comparable to the decay length of these interface modes, interactions between SPPs can appear, giving rise to coupled SPP modes named as Long-Range Surface Plasmons (LR-SPPs) and Short-Range Surface Plasmons (SR-SPPs), according to their symmetry[37]. These SPP coupling mechanisms could further increase the absorption of thin film solar cells because LR-SPPs propagate for longer distances at the metal/semiconductor interface and penetrate deeper into this latter layer[38]; for this reason, efficient light absorption is possible if the absorption of these SPP modes in the semiconductor layer is stronger than in the metal[6]. Moreover, coupled SPP modes are efficient mediators for energy transfer between donor and acceptor molecules on opposite sides of a metallic thin film – where Dexter (based on wave-function overlap) and Förster (due to the near-field resonant dipole-dipole interaction) – energy transfer mechanisms fail[39] or, as already mentioned, can be used to promote the hot-carrier generation for photovoltaic, photocatalytic devices[25] and thermoelectric power conversion or refrigeration[31]. This type of coupled-SPP plasmonic excitations can be achieved also in other structures known as MetaMaterials (MMs).

MetaMaterials derive their name from the Greek word μετά (meta), meaning “beyond”, because they are characterized by properties that are not found in natural materials. MMs are artificial media with a sub-wavelength periodic geometry, rationally conceived to possess extraordinary optical properties which are not derived from the

constituent materials (like for natural media) but that originate from the newly designed arrangement in the structure rather than from their chemical composition. For these reasons, MMs can be engineered for several applications in all aspects of material science[40]. A class of uniaxial MMs with highly anisotropic features is constituted by Hyperbolic MetaMaterials (HMMs)[41]. The optical response of HMMs can be easily designed in the framework of the Effective Medium Theory (EMT), an approximation used to model and describe the macroscopic optical properties of composite materials as a quasi-homogeneous effective medium. The effect of using this approximation is schematized in Figure 3.8 for a generic composite material.

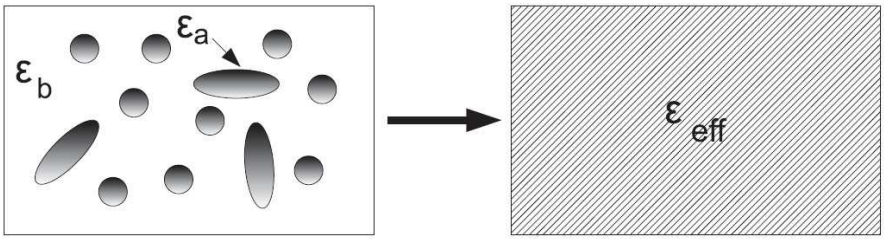


*Figure 3.8- Schematization of the effective medium approximation.*

Using this approximation, the effective dielectric tensor of a uniaxial HMM can be described as in Equation 5:

$$\hat{\varepsilon} = \begin{pmatrix} \varepsilon_{//} & 0 & 0 \\ 0 & \varepsilon_{//} & 0 \\ 0 & 0 & \varepsilon_{\perp} \end{pmatrix} \tag{5}$$

Here the subscript // and ⊥ indicate the $\varepsilon_{xx}=\varepsilon_{yy}$ and the $\varepsilon_{zz}$ components of this tensor, respectively. Usually, the three diagonal components are all positive and the corresponding isofrequency surfaces have a spherical (for isotropic media) or ellipsoidal shape (for uniaxial materials). HMMs are extremely anisotropic materials for which the relation $\varepsilon_{//} \cdot \varepsilon_{\perp} < 0$ is verified and the spherical isofrequency surface for wave propagation in vacuum distorts to a hyperboloid inside the material for TM polarization. Hence, the denomination of hyperbolic.

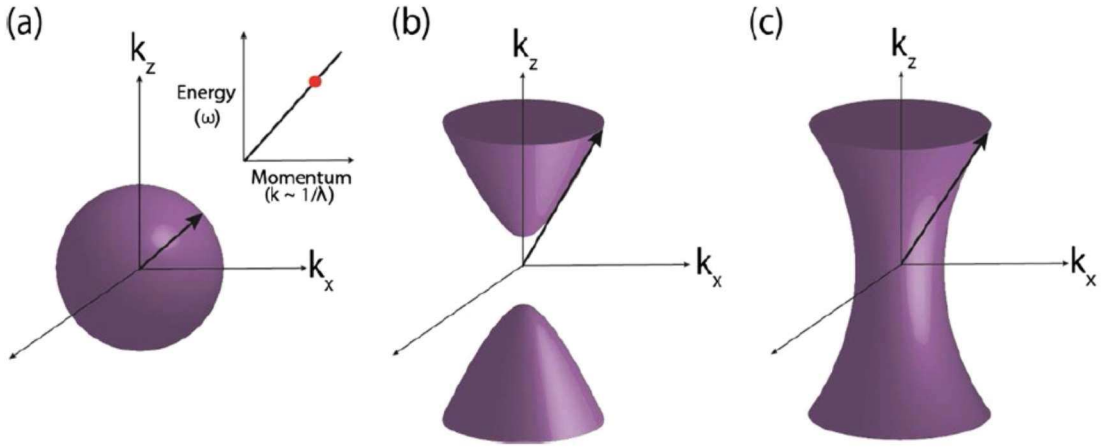


*Figure 3.9- Isofrequency surface for a) an isotropic medium (inset: dispersion relation with a red dot indicating the frequency for the derived isofrequency surface), b) Type-I HMM and c) type-II HMM[42].*

As shown in Figure 3.9, two different cases can be obtained: Type I HMM, in which $\varepsilon_{//}>0$ and $\varepsilon_{\perp}<0$, and Type-II HMM where $\varepsilon_{//}<0$ and $\varepsilon_{\perp}>0$. These conditions require the material to behave like a metal in one direction and as a dielectric in the other one and, consequently, metals and dielectrics/semiconductors have to be used as building blocks to construct these artificial media. The open shape of their isofrequency surface allows the propagation of waves with infinitely large wave-vector, as a result of the near-field coupling of SPPs forming at each of the metal/dielectric interfaces in the structure[42]. As already mentioned, SPPs can couple in multilayered arrangements; hence this type of structures is the most simple way to engineer a HMM, but other geometries exist[41a]. The main characterization of HMMs is carried out by analyzing their reflection and transmission spectra, as a function of the angle of incidence, for p- and s-polarized light separately, because features of hyperbolic behavior appear only for TM (p-) light polarization.

### 3.4.1 Differences in plasmonic and metamaterial absorbers

Both resonant plasmonic and metamaterial structures allow for the possibility to rationally design and fabricate devices with suitable optical properties at the nanoscale,

such as absorption, emission or refraction. For photovoltaic applications, these structures have been mainly used to enhance the absorption of the solar cell, improving in this way the performances of these devices. The main difference between metamaterial absorbers and other plasmonic approaches for enhancing solar power conversion efficiency is that the former approach provides more flexible light management in terms of broadband[43], polarization independent[44] and wide angular optical absorption[45]. In particular, the latter feature is a great advantage for solar light harvesting and PV applications, where there is a large portion of solar power coming from diffuse light due to atmospheric scattering. Indeed, these features cannot be easily achieved using conventional plasmonic structures integrated in solar cells, like nanoparticles or simple metallic back-contact gratings, due to their narrow-band plasmon resonance. However, MM absorbers and, specifically, HMMs have not been studied systematically in the literature for photovoltaic applications[46] and only few works employing HMMs as absorbers for PV applications (both theoretical and experimental) exist[47].

## 3.5 ALUMINUM PLASMONICS

Usually, most of the plasmonic works have involved noble metals such as gold or silver. These metals exhibit plasmon resonance in the visible spectral region but are expensive, limiting their application in real-life devices. The plasmonic response of aluminum has been studied[48] during the past 10 years for different reasons:

- Reduction of material cost;
- Material abundance;
- Possibility of large scale production with the fabrication technology of microelectronics[49] (where processes are well known for Al deposition, patterning and etching);
- High tunability[50] as a function of size, shape, use of different substrates and native oxide content (from deep UV to visible and near-IR) respect to other plasmonic metals.

Most of the applications of Al-based plasmonic systems take advantages from the higher plasma frequency of this metal (if compared with gold or silver), with a surface plasmon resonance in the UltraViolet (UV) spectral region. However, due to the possibility to excite interband transitions in the near-IR range[49,51], possible hybrid surface plasmon-interband modes can also occur[52], enhancing the absorption properties of the Al-based nanostructures through the UV-VIS-NIR spectral range. All these features, together with the opportunity to generate hot-electrons[53], are extremely important for PV applications. Indeed, they pave the way for the opportunity to overlap the plasmonic metal optical response with the absorption of OPV active materials, to engineer the use of these additional absorption bands for increasing the OPV efficiency[54] and, moreover, being this metal extensively used as a low work-function counter-electrode in common OPV devices (such as the BHJ based on P3HT:$PC_{60}BM$ active layer) its plasmonic properties can be integrated in a natural way in this type or organic solar cells. Nevertheless, only few examples of Aluminum-based HMMs are reported in the literature,[55] which is still an unexplored but potentially fertile field of research.

## 3.6 TOWARDS HMM-SOLAR CELLS

In this work, a first attempt in trying to use the previously analyzed plasmonic effects of HMMs for improving the efficiency of solar devices is reported. In detail, this part of the thesis is focused on the possibility to take advantage of an enhanced absorption in the NIR sunlight spectrum induced by the presence of an HMM. Such an HMM is composed by sub-wavelength-sized layers of the well-studied Bulk HeteroJunction P3HT/$PC_{60}BM$ (as a dielectric) and of Al (as a metal). These materials are widely employed in the construction of standard configuration solar devices where aluminum acts as the counter-electrode and all the photogenerated carries are formed in the “thick” absorbing active layer blend, as shown in Figure 3.10. Thus, the generation of charge is limited to the spectral region of the active layer absorption in the visible range and a significant portion of the sunlight

spectrum (from the NIR to higher wavelength) still cannot be collected. In the new concept HMM-solar device proposed, the excitation and coupling of SPPs at each metal/BHJ interface, for rationally designed thicknesses, could lead to enhanced absorption in this spectral range and, consequently, lead to an improved efficiency of the solar cell constructed inside the HMM design.

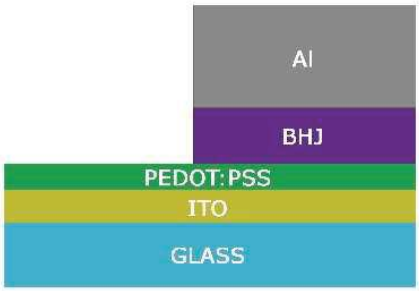


*Figure 3.10- Schematic representation of "standard-thickness" BHJ solar cells used in this work.*

## 3.7 EXPERIMENTAL SECTION AND DATA DISCUSSION

The commonly used thicknesses for each layer in P3HT:$PC_{60}$BM BHJ solar cells are summarized in Table 3.1, where a comparison between literature data[56] and optimized thicknesses and domain size for normal OPV devices realized in this work are reported:

| *Layer* | *Thickness range (nm) literature / optimized in our lab* | *Domain size (nm) literature / optimized in our lab* |
|---|---|---|
| *PEDOT:PSS* | **0 -50 / 30 - 35** | |
| *P3HT:$PC_{60}$BM Blend* | **40 - 300 / 100 - 120** | **10 - 40 / 25 - 30** |
| *Al* | **100 - 200 / 200** | |

*Table 3.1- Typical and optimized thickness of different layers and domain size within the active layer of P3HT:$PC_{60}$BM BHJ solar cells.*

These typical thicknesses for standard solar cells are not compatible with the construction of a plasmonic device, where the clear prerequisite of using nanostructures with sub-wavelength dimension is required. However, by changing the experimental condition for the spin-coating deposition for the active blend (time and/or spinning rate) and the deposition thickness of the evaporated metal, it can become possible to meet this requirement on thickness.

### 3.7.1 Ellipsometric characterization: complex refractive indices, thicknesses and absorption properties

To rationally design the hyperbolic/plasmonic structure to build with these starting materials, preliminary measurements of the complex refractive indices and of the other optical features of each layer were conducted, also as a function of the layer thickness, through spectroscopic ellipsometry. These measurements, together with all the simulations, were conducted in collaboration with the institute CNR-Nanotec. Spectroscopic ellipsometry is a powerful technique that can be used to calculate several properties of a material including the layer thickness, the refractive index and the extinction coefficient, by measuring the changes in phase (Δ) and polarization (Ψ) of reflected and transmitted polarized-light from the material under study, deposited as a thin film onto a substrate. By iterative fitting (to obtain the minimum least-square error) of these data with models depending on the material type and the region of interest of the light spectrum, it is possible to match the experimentally measured data against the simulated ones. From the analysis of this comparison and from the characteristic parameters of the model, the refractive index and the thickness of the investigated material can be estimated. Moreover, in this work, the thicknesses of the deposited layers were double-checked with a stylus profilometer (for solution spin-coated films) or with a quartz microbalance (during the thermal deposition of the metal layers). This preliminary ellipsometric characterization on all used materials has a fundamental importance because the optical model for multilayer structures, based on the Transfer/Scattering Matrix

Method (TMM - SMM), requires, as the input data, the thickness of each layer together with their complex refractive indices.

### 3.7.1.1 Analysis of BHJ thin films

As already mentioned, an ellipsometric characterization was conducted on films of different thickness for the active layer blend used in this work (P3HT as a donor and $PC_{60}BM$ as the acceptor), with the aim of measuring complex dielectric permittivity and thickness of films of this blend. Typical examples of these measurements are shown in Figure 3.11 a (for the real part of the dielectric permittivity) and 3.11 b (for the imaginary part), while the experimental conditions for the preparation of these films and the measured thickness are summarized in Table 3.2.

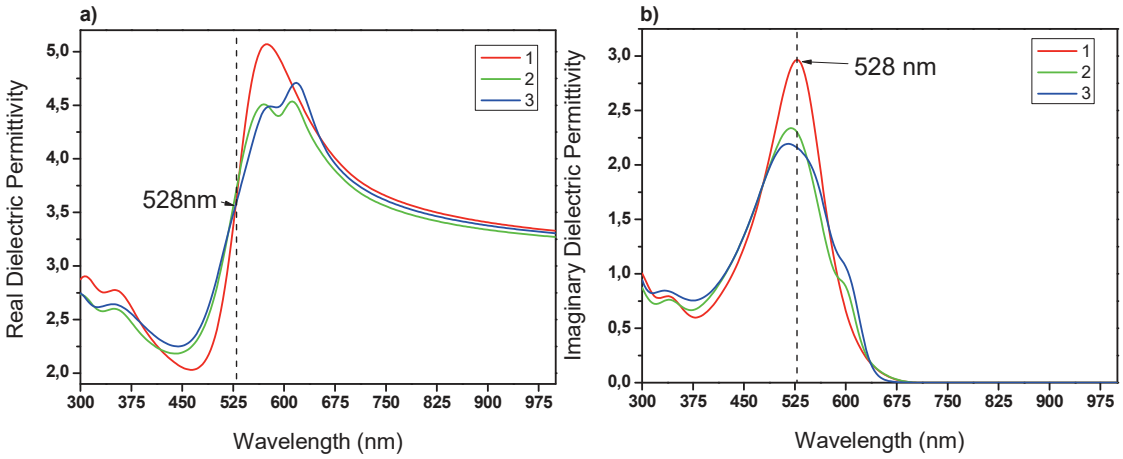


*Figure 3.11- a) Real and b) imaginary part of dielectric permittivity measured for P3HT:$PC_{60}BM$ films of different thickness on glass; see Table 3.2 for details.*

| *BHJ sample* | *Spin coating condition Rpm - time* | *Ellipsometric thickness (nm)* | *Profilometer thickness (nm)* |
|---|---|---|---|
| *1* | **700 – 1'** | **95** | **≈ 100** |
| *2* | **1500 – 1'** | **44** | **≈ 45** |
| *3* | **3000 – 1'** | **39** | **≈ 36** |

*Table 3.2- Experimental conditions for preparation of BHJ samples for ellipsometric measurements.*

Minor variances for the maximum of the peak in Figure 3.11 are due to the slight difference in transmittance and reflection spectra for these samples characterized by different thickness. The absorption peak (at about 530 nm – see Figure 3.11 b) is clearly present in all the spectra and, of course, it is more defined for the thicker and more absorbing sample (100 nm). The low-intensity and additional signals between 600 nm and 650 nm for thinner films could indicate a slightly different morphology of these samples. Indeed, a thermal annealing process (that is necessary during the fabrication of optimized solar cell based on this BHJ) was conducted in the same manner (150°C for 30 minutes) for all the prepared samples. However, this process was adjusted for "standard thickness" solar device; for thinner films, it is reasonable that this thermal treatment could lead to a little difference in the phase separation between the polymer and the fullerene and, above all, to difference in crystallization degree in the donor phase, causing the presence of this additional peak. In any case, the maximum in absorbance is in accordance with the literature[57]. A BHJ active layer of about 100 nm is the "reference thickness" for the normal configuration of these solar cells, while 45 nm was the chosen as "plasmonic active layer" thickness to use during following experimental work regarding the HMM preparation. This choice was dictated by the need to have a functioning reference system to evaluate the effect of the construction of the HMM-solar cell. Too thin BHJ films, indeed, could limit the direct absorption of light in the semiconductor slab and, if used in devices with standard aluminum thickness (for which no plasmonic effects are expected) could show low current and no diode-like J-V curves.

#### 3.7.1.2 Analysis of Al thin films and of BHJ/Al one-bilayer systems

Even more important than the absorption features of the BHJ semiconductor layer, for constructing a plasmonic solar cell it is necessary to have bands associated to metallic nanostructures in the absorption spectrum. For this reason, ellipsometric characterizations were performed on thermally deposited films of aluminum, in the thickness range from 5 nm to 200 nm, to evaluate the presence of plasmonic features. The dielectric function and morphology of these thin films (and, consequently, their plasmonic properties), heavily

depend on the deposition conditions[58]; that is why thermal deposition of all aluminum samples analyzed in this work have been conducted with the same experimental conditions (pressure of ~ $1 \cdot 10^{-6}$ mbar and deposition rate around 2 Å/s). Transmission and reflection spectra were collected and absorption was then calculated as:

$$\mathrm{Abs}(\lambda) = 1 - [\mathrm{Refl}(\lambda) + \mathrm{Trans}(\lambda)] \tag{6}$$

Results are shown in Figure 3.12 for two selected angles of incidence (40 and 80 degrees) and for TM- (or "p-pol") polarization of light. Measurements were conducted even for TE-polarized light (or "s-pol") but, as previously mentioned, these plasmonic resonances for metallic thin films are sensitive only to the TM-polarization. Therefore, results are shown only for this polarization. The absorption of 200 nm-thick aluminum films was not included because, for this relatively thick film with a very smooth surface, most of the incident light was reflected, with no significant absorption.

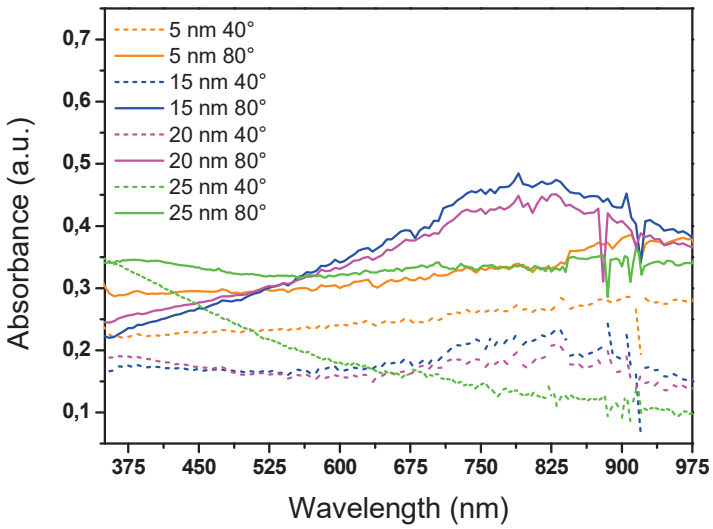


*Figure 3.12- Absorption spectra of Al thin films for p-polarized light and for different angle of incidence.*

Analysis of these spectra reveals the presence of a broad absorption plasmonic band peaked around 800 nm for incident light at 80° and p-polarization, for film thicknesses of

15 nm and 20 nm. As stated above, aluminum thin films could show plasmonic absorption enhancement from UV (where the surface plasmon resonance is located) to near-IR (due to the possibility of interband transitions and hybrid resonances)[50,52]. Therefore, these results are in agreement with the excitation of plasmons and hybrid modes in aluminum films. Absorption from films with other thicknesses shows, instead, a flat response for the entire considered spectral range. For nominal aluminum thickness of 5 nm, it is reasonable that a dense metallic film is not formed, leading to the absence of additional absorption bands relative to the plasmonic excitations; 25 nm-thick films, instead, could be thick enough to show no specific absorption enhancement. This aluminum absorption enhancement has been confirmed even for a one-bilayer hyperbolic system of BHJ 45 nm and Al (different thicknesses), as shown in Figure 3.13. Here, for clarity, only the spectra recorded for a 45 nm BHJ layer and aluminum film thickness of 20 nm and 200 nm are reported, for p-polarized incident light and for angles of incidence of 40° and 80°.

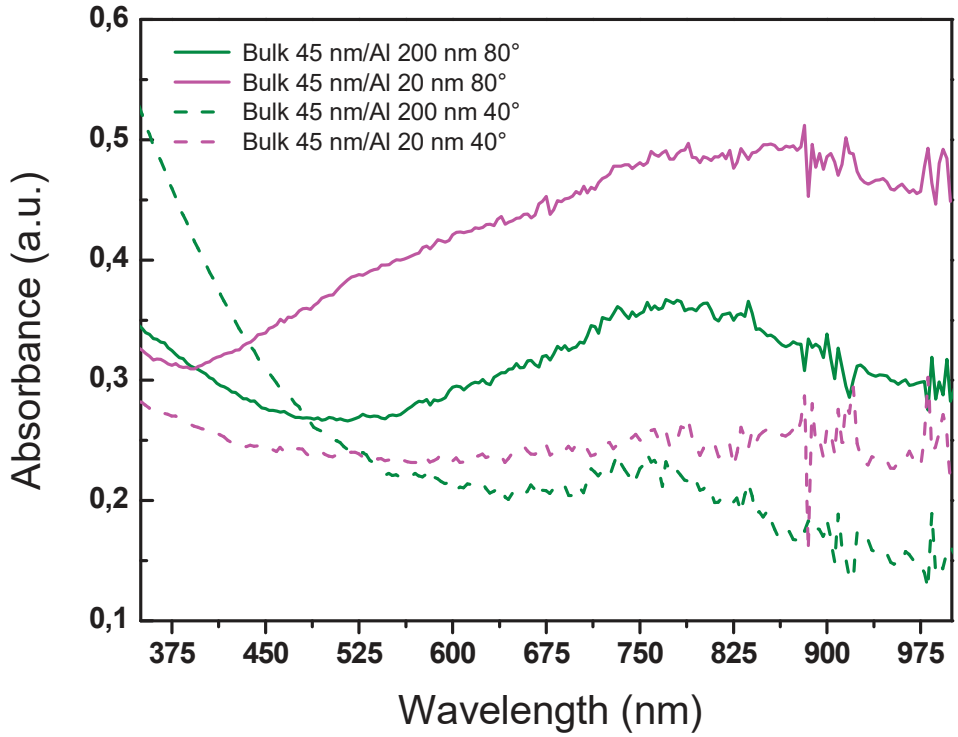


*Figure 3.13- Absorption spectra for one BHJ/Al bilayer system and p-pol light.*

From the spectra in Figure 3.13, it is clear that the absorption of the bilayer system is improved in the NIR spectral range, where the BHJ active layer does not absorb light. In this experiment, light strikes the sample from Al-side and for the thicker film (200 nm) the plasmonic absorption due to the single hyperbolic bilayer is much less pronounced due to major reflectance of this sample.

### 3.7.2 Plasmonic solar cells

To confirm if the measured improvement in absorption in the NIR spectral range - due to the plasmonic effect of aluminum thin films - could be used to improve a solar device efficiency, BHJ solar cells with P3HT:$PC_{60}BM$ as an active layer were prepared and tested under standard conditions (AM1.5G and 100mW/$cm^2$). Some devices (type A) consist of a "standard-thickness" active layer (around 100 nm) and several plasmonic-thicknesses for the aluminum layer, used as the counter-electrode; in this case the reference system is type A6 (see Table 3.3). Type B devices, instead, have been prepared with plasmonic layers of both aluminum and BHJ; the reference system is type B6 (Table 3.4). The best J-V curves are shown in Figure 3.14 a and b for the two series of samples and the corresponding figures-of-merit (mediated over about 12 cells) are listed in Tables 3.3 and 3.4.

| *Type A* *BHJ thickness / nm* | *Sample type* | *Al thickness / nm* | *Efficiency / %* | *$J_{sc}$ / mA/$cm^2$* | *$V_{oc}$ / V* | *FF* |
|---|---|---|---|---|---|---|
| *100* | **A1** | **5** | **0.48 ± 0.14** | **-2.63 ± 0.66** | **0.63 ± 0.07** | **0.27 ± 0.03** |
| *100* | **A2** | **10** | **1.82 ± 0.18** | **-6.23 ± 0.44** | **0.63 ± 0.01** | **0.46 ± 0.07** |
| *100* | **A3** | **15** | **2.28 ± 0.33** | **-7.00 ± 0.43** | **0.64 ± 0.01** | **0.51 ± 0.09** |
| *100* | **A4** | **20** | **2.63± 0.21** | **-7.21 ± 0.44** | **0.63 ± 0.01** | **0.58 ± 0.02** |
| *100* | **A5** | **25** | **1.92 ± 0.18** | **-5.55 ± 0.32** | **0.65 ± 0.01** | **0.54 ± 0.06** |
| *100* | **A6** | **200** | **2.12± 0.37** | **-7.31 ± 0.48** | **0.59 ± 0.02** | **0.49 ± 0.05** |

*Table 3.3- Figures of merit for Type A devices.*

| *Type B* *BHJ thickness / nm* | *Sample type* | *Al thickness / nm* | *Efficiency / %* | *$J_{sc}$ / mA/cm$^2$* | *$V_{oc}$ / V* | *FF* |
|---|---|---|---|---|---|---|
| *45* | **B1** | **5** | **0.42 ± 0.13** | **-2.13 ± 0.31** | **0.60 ± 0.03** | **0.32 ± 0.03** |
| *45* | **B2** | **10** | **1.36 ± 0.02** | **-4.64 ± 0.19** | **0.63 ± 0.01** | **0.47 ± 0.02** |
| *45* | **B3** | **15** | **1.73 ± 0.09** | **-4.85 ± 0.29** | **0.64 ± 0.01** | **0.57 ± 0.02** |
| *45* | **B4** | **20** | **1.62 ± 0.30** | **-4.73 ± 0.40** | **0.63 ± 0.01** | **0.54 ± 0.05** |
| *45* | **B5** | **25** | **1.22 ± 0.12** | **-3.80 ± 0.26** | **0.63 ± 0.01** | **0.51 ± 0.05** |
| *45* | **B6** | **200** | **1.56 ± 0.13** | **-4.97 ± 0.30** | **0.60 ± 0.02** | **0.52 ± 0.01** |

*Table 3.4- Figure of merit of Type B devices.*

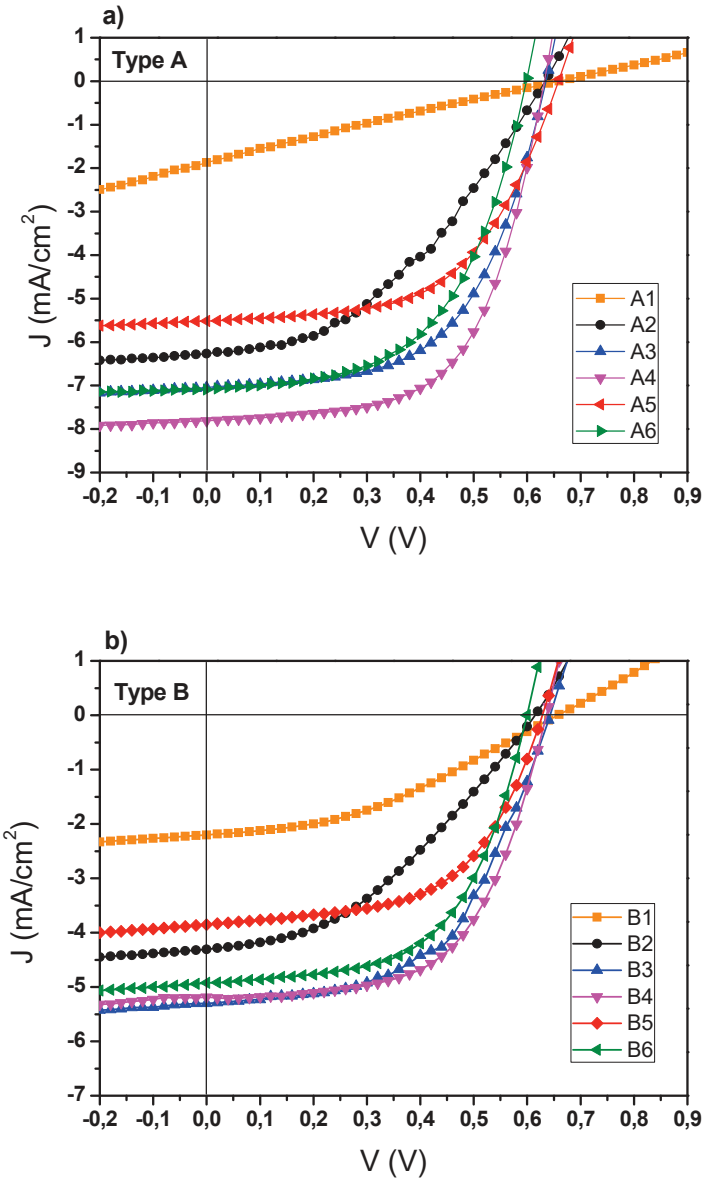


*Figure 3.14- J-V curves for a) best Type A devices and b) best Type B devices under study.*

From Figures 3.14, the beneficial contribution of plasmonic designed thin Al layers in determining the enhancement in PCE of the devices is evident. For the values reported in Tables 3.3 and 3.4 for the short circuit current, regardless of the BHJ layer thickness, solar cells obtained with 15 nm and 20 nm aluminum films (A3, A4 and B3, B4) do not show the marked enhanced photogeneration performance with respect to the control devices (A6 and B6) that is instead clearly visible in Figure 3.14 only for the best devices. The high dispersion that usually characterizes the $J_{sc}$ point in these solar cells makes the plasmonic improvement to be hidden in the experimental error. However, the $V_{oc}$ of these plasmonic

devices shows a clear improvement. This could be due to the creation of a better Ohmic contact between the BHJ and aluminum. The FF shows a little improvement as well. This parameter heavily depends on charge recombination phenomena due to the presence of impurities with energy states within the band-gap[59] or on the set-up of a space charge regime caused by a large difference in the hole and electron mobilities[60] and/or by the ineffective charge collection at the electrodes. Because of the higher $V_{oc}$ exhibited by plasmonic solar cells, it is possible for these thin film electrodes to have better electron-extraction properties, leading to an improvement of both these parameters. Further experiments aimed to explain the reasons behind this enhancement in PCE are in progress and focused on clarifying the role of the improved absorption (EQE) and the importance of the angle of incidence of light.

### 3.7.3 Towards HMM-Solar cells

Results on one bilayer BHJ/Al system are encouraging. However, as required for constructing a HMM, a multilayers system, as illustrated in Figure 3.15, is needed.

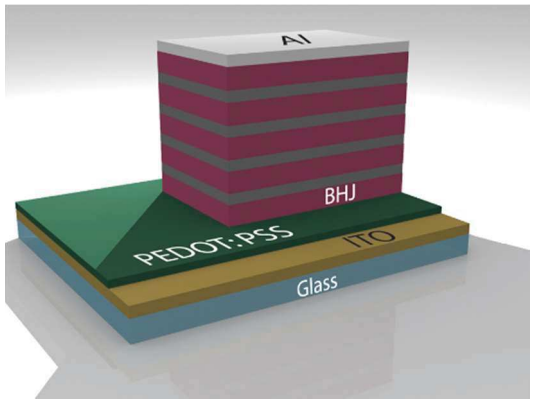


*Figure 3.15- Representation of the proposed HMM-OSC.*

As a first steps toward this new device concept, two type of simulations have been performed:

- The effective medium approximation (EMA) theory has been used to derive the values of the permittivity components of the uniaxial tensor and verify if the hyperbolic condition is fulfilled (see Figure 3.16).
- TMM calculated transmittance and SMM simulated reflectance spectra have been used to evaluate the absorption properties of a "perfect" two-bilayer system [BHJ (45 nm)/Al (20 nm)/BHJ (45 nm)/Al (20 nm)] and to compare the experimental (ellipsometric) data on a real sample with the simulated one (see Figure 3.17).

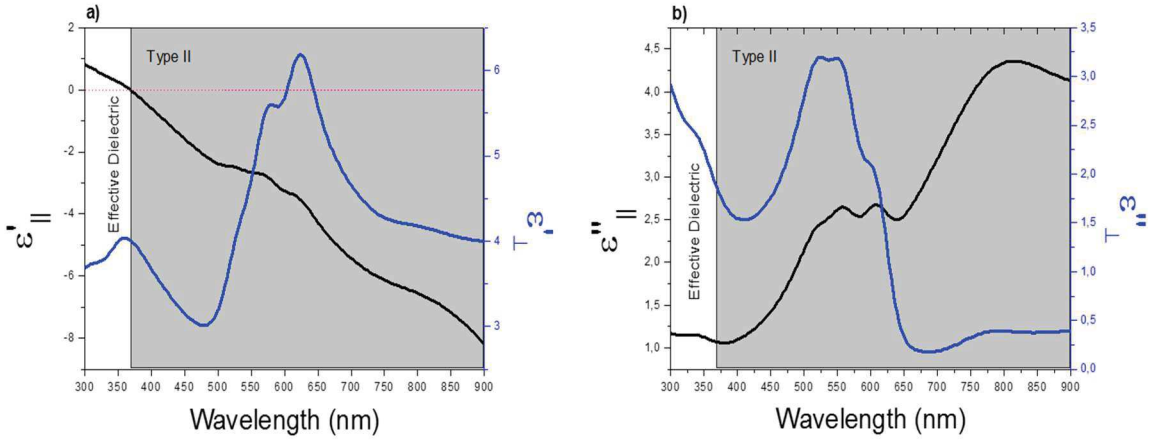


*Figure 3.16- a) real and b) imaginary $\varepsilon_{//}$ and $\varepsilon_{\perp}$ components of the polarizability tensor of the two-bilayers system, as predicted by EMA.*

As it can be seen, this multilayer structure gives rise to a Type-II HMM for most of Vis-NIR spectral range.

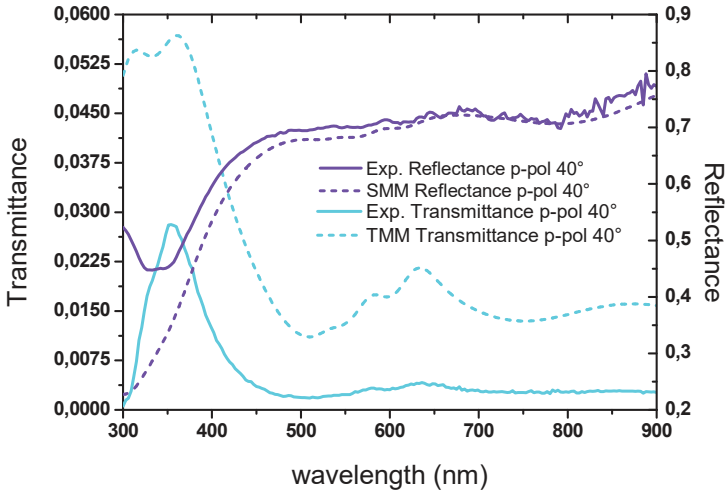


*Figure 3.17- Simulated (dotted line) and experimental (solid line) Transmittance and Reflectance of a two-bilayer BHJ/Al system.*

From Figure 3.17 there is a good accordance between theoretical and experimental data, indicating the robustness of the experimental procedure followed for the preparation of these samples and the validity of the ellipsometric measurements. Moreover, Type-II BHJ/Al HMM shows high absorbance in the NIR range, thus configuring as a good candidate to absorb light at these wavelengths. This appears to be evident from the absorbance definition in Equation 6 according to which the light that is not reflected is almost all absorbed (transmittance of this system is very low from 500 nm to 900 nm).

## 3.8 CONCLUSIONS

In this chapter, preliminary results towards the construction of a HMM-organic solar cell are presented. This device configuration could offer an extraordinary possibility of engineering the absorption band of the entire multilayered structure to achieve the desired absorption performances, even in spectral ranges where organic materials usually cannot absorb the solar radiation, improving in this way the performance of the devices. A plasmonic one-bilayer system consisting of P3HT:$PC_{60}BM$ BHJ and aluminum thin films of appropriate thicknesses was prepared and characterized from the optical (ellipsometry) and electrical (J-V curves) point of view. Plasmonic solar cells showed an improvement in PCE between 10 and 20 %, when compared to reference devices. The major improvements towards enhanced device efficiency were recorded on $V_{oc}$ and FF, rather than on $J_{sc}$. Additional experimental work aimed to a better understanding of the phenomena behind this enhanced power conversion efficiency (EQE measurements *in primis*) is in progress.

Simulations were conducted using the Effective Medium Theory and TMM and SMM methods for a two-bilayer system, showing that the Type-II regime occurs from the Vis to the NIR, where this multilayer structure showes a high absorbance. These results towards a plasmonic HMM- solar cell are very encouraging and their relevance goes well beyond the use of the particular system chosen in this work, since it is possible to replace it with a myriad of promising metal/dielectric combinations.

## 3.9 BIBLIOGRAPHY

**[1]** P.E. Shaw, A. Ruseckas, I.D.W. Samuel, *Adv. Mater*., **2008**, 20, 3516.
**[2]**J.K. Lee, N.E. Coates, S. Cho, N.S. Cho, D. Moses, G.C. Bazan, K. Lee, A.J. Heeger, *Appl. Phys. Lett*., **2008**, 92, 243308.
**[3]** M.G Debije, P.C. Verbunt, *Adv. Energ. Mater*., **2012**, 2, 12.
**[4]** A.C. Atre, A. Garcia-Extarri, H. Alaeian, J.A. Dionne, *J. Opt*., **2012**, 14, 024008.
**[5]** H.K. Raut, V.A. Ganesh, A.S. Nair, S. Ramakrishna, *Energ. Environ. Sci*., **2011**, 4, 3779.
**[6]** H.A. Atwater, A. Polman, *Nature Mater*., **2010**, 9, 205.
**[7]** C. bronnbauer, J. Hernich, N. Gasparini, F. Guo, B. Hartmeier, N.A. Luechinger, C. Pflaum, C.J. Brabec, K. Forberich, *Adv. Opt. Mater*., **2015**, 3, 1424.
**[8]a)** K. Tvingstedt, S. DalZilio, O. Inganäs, M. Tormer, *Opt. Express*, **2008**, 16, 21608;
**b)** O Fidaner, F.A. Suarez, M. Weimer, V.A. Sabnis, T. Asano, A. Itou, D. Inoue, N. Hayashi, M. Arase, A. Matsushita, T. Nakagawa, *Appl. Phys. Lett*., **2014**, 104, 103902.
**[9]**K. Forberich, G. Donneler, M.C. Scharber, K. Hingerl, T. Fromherz, C.J. Brabec, *Thin Sol. Films*, **2008**, 516, 7167.
**[10]a)** J.A. Faucheaux, A.L.D. Stanton, P.K. Jain, *J. Phys. Chem. Lett*., **2014**, 5, 976;
**b)** J.M. Luther, P.K. Jain, T. Ewers, A.P. Alivisatos, *Nature Mater*., **2011**, 10, 361.
**[11]** Y. Yang, Gang Li, *Progress in High-Efficient Solution Process Organic Photovoltaic Devices: Fundamentals, Materials, Devices and Fabrication*, Springer, **2015**.
**[12]** E. Stratekis, E. Kymakis, *Mater. Today*, **2013**, 16, 133.
**[13]** V.E. Ferry, J.N. Munday, H.A. Atwater, *Adv. Mater*., **2010**, 22, 4794.
**[14]** C.F. Guo, T. Sun, F. Cao, Q. Liu, Z. Ren, *Light: Sci. Appl*., **2014**, 3, e161.
**[15]** S. Pillai, M.A. Green, *Sol. Energ. Mater. Sol. Cells*, **2010**, 94, 1481.
**[16]**H. Raether, Surface Plasmons on Smooth and Rough Surfaces and on Gratings, Springer-Verlag, **1988**.
**[17]** W.L. Barnes, A. Dereux, T.W. Ebbesen, *Nature*, **2003**, 424, 824.
**[18]a)** E. Kretscmann, *Z. Phys*., **1971**, 241, 313;
**b)** A. Otto, *Z. Phys*., **1968**, 216, 398.
**[19]**H.R Ritchie, E.T Arakawa, J.J. Cowan, R.N. Hamm, *Phys. Rev. Lett*., 1968, 21, 1530.
**[20]a)** T.H. Isaac, J. Gòmez Rivas, J.R. Sambles, W.L. Barnes, E. Hendry, *Phys. Rev. B*, **2008**, 77, 113411;
**b)** S.-H. Chang, S.K. Gray, *Opt. Express*, **2005**, 13, 3150.
**[21]** R. Malureanu, A. Lavrinenko, *Nanotechnol. Rev*., **2015**, 4, 259.
**[22]** J. Stoltenberg, D. Pengra, courses.washington.edu/phys431/SPR/spr.pdf
**[23]** Q. Gan, F.J. Bartoli, Z.H. Kafafi*, Adv. Mater*., **2013**, 25, 2385.
**[24]a)** F. Wang, N.A. Melosh, *Nanolett*., **2011**, 11, 5426;
**b)** J. Li, S.K. Cushing, P.Zheng, T. Senty, F. Meng, A.D. Bristow, A. Manivannan, N. Wu, *JACS*, **2014**, 136, 8438;
**c)** L. Du, A. Furube, K. Hara, R. Katoh, M. Tachiya, *J. Photochem. Photobiol. C: Photochem. Rev*., **2013**, 15, 21;
**d)** S. Mubeen, J. Lee, N. Singh, S. Krämer, G.D. Stucky, M. Moskovits, *Nature Nanotech*., **2013**, 8, 247;
**e)** M.W. Knight, Y. Wang, A.S. Urban, A. Sobhani, B.Y. Zheng, P. Nordlander, N.J. Halas, *Nanolett*., **2013**, 13, 1687.
**[25]** C. Clavero, *Nature Photonics*, **2014**, 8, 95.

**[26]** K. Wu, J. Chen, J.R. McBride, T. Lian, *Science*, **2015**, 349, 632.
**[27]** M.L. Brongersma, N.J. Halas, P. Nordlander, *Nature Nanotechnol*., **2015**, 10, 25.
**[28]** T. Inagaky, K. Kagami, E.T. Arakawa, *Phys. Rev. B*, **1981**, 24, 3644.
**[29]** T.P. White, K.R. Catchpole, *Appl. Phys. Lett*., **2012**, 101, 073905.
**[30]** M. Moskovits, *Science*, **2011**, 332, 676.
**[31]** S.V. Boriskina, H. Ghasemi, G. Chen, *Mater. Today*, **2013**, 16, 375.
**[32]** M.W. Knight, H. Sobhani, P. Nordlander, N.J. Halas, *Science*, **2011**, 332, 702.
**[33]** Y. Tian, X. Wang, D. Zhang, X. Shi, S. Wang, *J. Photochem. Photobiol. A: Chemistry*, **2008**, 199, 224.
**[34]** K. Yu, N. Sakai, T. Tatsuma, *Electrochem*., **2008**, 76, 161.
**[35]a)** K. Marchuk, K.A. Willets, *Chem. Phys*., **2014**, 445, 95;
**b)** H.-N. Barad, A. Ginsburg, H. Cohen, K.J. Rietwyk, D.A. Keller, S. Tirosh, Y. Bouhadana, A.Y. Anderson, A. Zaban, *Adv. Mater. Interfaces*, **2016**, 3, 1500789;
**c)** D. Zhang, W.C.H. Choy, F. Xie, W.E.I. Sha, X. Li, B. Ding, K. Zhang, F. Huang, Y. Cao, *Adv. Funct. Mater*., **2013**, 23, 4255.
**[36]a)** F.P. Garcia de Arquer, A. Mihi, D. Kufer, G. Konstantatos, *ACS Nano*, **2013**, 7, 3581;
**b)** F.B. Atar, E. Battal, L.E. Aygun, B. Daglar, M. Bayindir, A.K. Okyay, *Opt. Express*, **2013**, 21, 7196;
**c)** F. Wang, N.A. Melosh, *Proc. of SPIE*, **2013**, 8111.
**[37]**S.A. Maier, *Plasmonics: Fundamentals and Applications*, Springer, **2007**.
**[38]** Z. Sakkat, S. Hayashi, D.V. Nesterenko, A. Rahmouni, S. Refki, H. Ishitobi, Y. Inouye, S. Kawata, *Opt. Express*, **2016**, 24, 20080.
**[39]**P. Andrew, W.L. Barnes, *Science*, **2004**, 306, 1002.
**[40]a)** V.G. Veselago, *Soviet Physics Uspekhi*, **1968**, 10, 509;
**b)** S. Xiao, V.P. Drachev, A.V. Kildishev, X. Ni, U.K. Chettiar, H.-K. Yuan, V.M. Shalaev, *Nature*, **2010**, 466, 735;
**c)**N.Liu, H. Guo, L. Fu, S. Kaiser, H. Schweizer, H. Giessen, *Nature Mater*.,**2008**, 7, 31.
**[41]a)** A. Poddubny, I. Irosh, P. Belov, Y. Kivshar, *Nature Photonics*, **2013**, 7, 958;
**b)** H.N.S. Krishnamoorthy, Z. Jacob, E. Narimanov, I. Kretzschmar, V. M. Menon, *Science*, **2012**, 336, 205.
**[42]** P. Shekhar, J. Atkinson, Z. Jacob, *Nano Convergence*, **2014**, 1:14.
**[43]a)** C.-H. Lin, R.-L. Chern, H.-Y. Lin, *Opt. Express*, **2011**, 19, 415;
**b)** C. Wu, G. Shvets, *Opt. Lett*., **2012**, 37, 308.
**[44]** K. Aydin, V.E. Ferry, R.M. Briggs, H.A. Atwater, *Nature Commun*., **2011**, 2:517.
**[45]** J. Wang, Y. Chen, J. Hao, M. Qiu, *J. App. Phys*., **2011**, 109, 074510.
**[46]** J. Gwamuri, D.Ö. Güney, J.M. Pearce, chap. 10 in *Solar Cell Nanotechnology*, Wiley, **2013**.
**[47]a)** A. Vora, J. Gwamuri, N. Pala, A. Kulkarmi, J.M. Pearce, D. Ö. Güney, *Sci. Reports*, **2014**, 4:4901;
**b)** T.U. Kumkur, L. Gu, J.K. Kitur, E.E. Narimanov, M.A. Noginov, *Appl. Phys. Lett*., **2012**, 100, 161103;
**c)** Y. Wang, T. Sun, T. Paudel, Y. Zhang, Z. Ren, K. Kempa, *Nano Lett*., **2012**, 12, 440.
**[48]a)** A. Taguchi, Y. Saito, K. Watanabe, S. Yijian, S. Kawata, *Appl. Phys. Lett*., **2012**, 101, 081110;
**b)** N.P. Hylton, X.F. Li, V. Giannini, K.-H. Lee, N.J. Ekins-Daukes, J. Loo, D. Vercruysse, P. Van Dorge, H. Sadebanlu, M. Sugiyama, S.A. Maier, *Sci. Reports*, **2013**, 3:2874;

**c)** F. Bisio, R. Proietti Zaccaria, R. Moroni, G. Maidecchi, A. Alabastri, G. Gonella, A. Giglia, L. Andolfi, S. Nannarone, L. Mattera, M. Canepa, *ACS Nano*, **2014**, 8, 9239;
**d)** G. Lonzano, D.J. Louwers, S.R.K. Rodriguez, S. Murai, D.T.A. Jansen, M.A. Verschuuren, J. Gomez-Rivas, *Light: Sci. Appl.*, **2013**, 2, e66.
**[49]** D. Gérard, S.K. Gray, *J. Phys. D: Appl. Phys*., 2015, 48, 184001.
**[50]** M.W. Knight, N.S. King, L. Liu, H.O. Everitt, P. Nordlander, N.J. Halas, *ACS Nano*, **2014**, 8, 834.
**[51]** M. Schwind, B. Kasemo, I. Zorić, *Nano Lett*., **2012**, 13, 1743.
**[52]** T. Pakizeh, *J. Opt*., **2013**, 15, 025001.
**[53**] T. Gong, J.N. Munday, *Appl. Phys. Lett*., **2017**, 110, 021117.
**[54] a)** K. Liu, B. Zeng, H. Song, Q. Gau, F.J. Bartoli, Z. Kafafi, *Opt. Commun*., **2014**, 314, 48;
**b)** V. Kochergin, L. Neely, C.-Y. Jao, H.D. Robinson, *Appl. Phys. Lett*., **2011**, 98, 133305.
**[55] a)** V.N. Smolyaninova, C. Jensen, W. Zimmerman, J.C. Prestigiacomo, M.S: Osofsky, H. Kim, N. Bassim, Z. Xing, M.M. Qazilbash, I.I. Smolyaninov, *Sci. Reports*, **2016**, 6:34140;
**b)** V. Smolyaninova, *SPIE newsroom*, doi: 10.1117/2.1201507.006009.
**[56]** Y.M. Nam, J. Huh, W.H. Jo, *Sol. Energ. Mater. Sol. Cells*, **2010**, 94, 1118.
**[57] a)** Z. Jin, J. Wang, *Appl. Phys. Lett*., **2013**, 102, 053304;
**b)** B. Hailegnaw, G. Adam, T. Yohannes, *Thin Solid Films*, **2015**, 589, 272;
**c)** D. Ryu, K.J. Loh, *Smart Mater. Struct*., **2014**, 23, 085011.
**[58]** K.M. McPeak, S.V. Jayanti, S.J.P. Kress, S. Meyer, S. Iotti, A. Rossinelli, D.J. Norris, *ACS Photonics*, **2015**, 2, 326.
**[59]** B. Kippelen, J.L. Brédas, *Energy Environ. Sci*., **2009**, 2, 251.
**[60]** Y.H. Huh, B. Park, I. Hwang, *J. Appl. Phys*., **2014**, 115, 124504.

# CHAPTER 4:
# ADDITIONAL RESULTS ON PLASMONIC HMMs

## 4.1 INTRODUCTION

During the optimization of the BHJ/Al HMMsfor PV applications, several experiments have been carried out with other plasmonic metals, such as silver, and other dielectric materials, such as titanium dioxide ($TiO_2$), with the aim of exploring the possibility of using the plasmonic resonances of these different HMMs for photovoltaic applications. Both Ag and $TiO_2$could be used to excite plasmonic effects in the near-UV and Visible spectral regions and, eventually, to overlap the absorption band of organic active layers in solar cells. Intriguing features were derived from these experiments and they will be briefly discussed as results of a side project that looks beyond photovoltaics.

## 4.2 Ag/BHJ PLASMONIC SYSTEM: FERRELL-BERREMAN MODE

With the aim to verify if changing the metal could have improved the absorption features of the multilayer system prepared with the BHJ under study, aluminum films were replaced by silver layers. The indispensable and preliminary optical characterization was conducted, layer by layer, as previously described for the Al-containing samples, and a scheme of the prepared hyperbolic samples is shown in Figure 4.1.

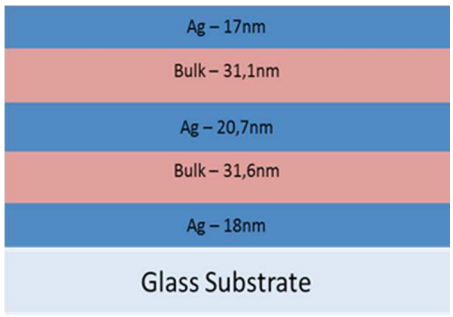


*Figure 4.1- Schematic representation of the multilayer Ag/BHJ sample under investigation; indicated thicknesses were extracted by ellipsometric measurements conducted for each layer.*

The effective medium simulation for this multilayer system reveals interesting features, as illustrated in Figure 4.2.

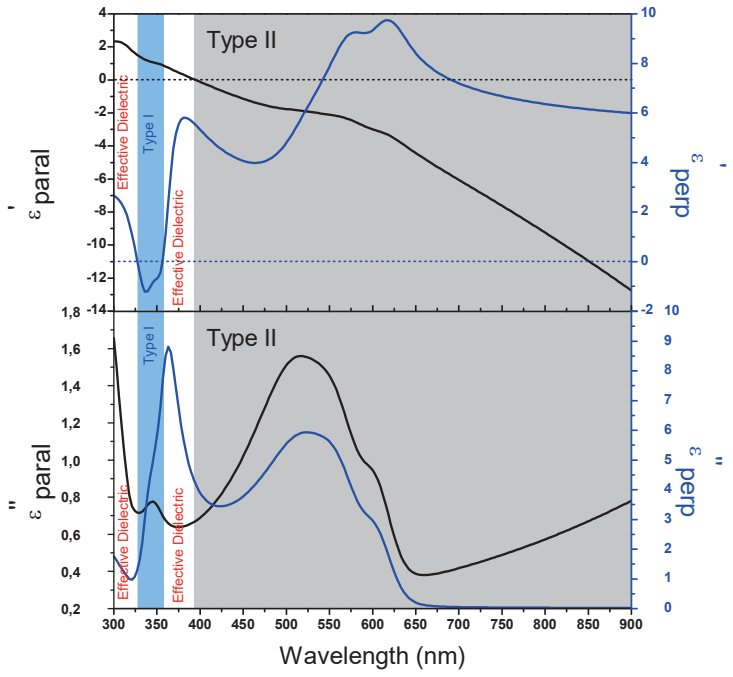


*Figure 4.2 - EMA for the Ag/BHJ multilayer structure.*

This sample is characterized by the co-existence of both types of HMM in different spectral ranges. It behaves as Type-I HMM from about 330 nm to 360 nmand as Type-II from about 400 nm to 900 nm. This latter type is characterized by two components of the effective dielectric tensor to be negative ($\varepsilon_{xx} = \varepsilon_{yy} = \varepsilon// < 0$ ; $\varepsilon_{zz} = \varepsilon_{\perp} > 0$); for this reason the sample is highly reflective in the Vis-near-IR spectral range and much less in the UV region, since a Type-II HMM is more metallic then its Type-I counterpart.

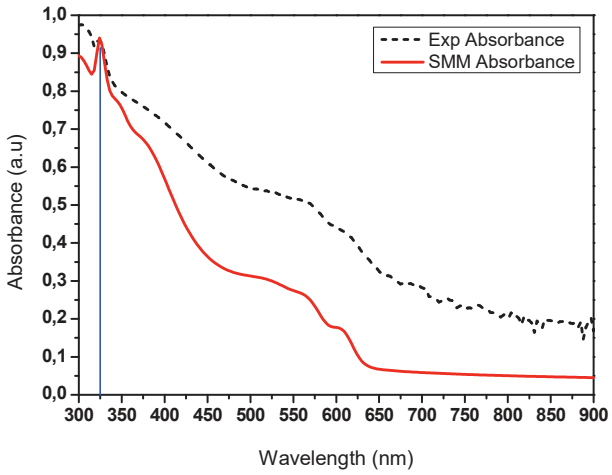


*Figure 4.3- Experimental and simulated absorbance for the multilayer system in Fig. XX.1; input data for the simulation wereextracted by the ellipsometric characterization.*

The absorbance analysis shown in Figure 4.3 for these HMMsreveals the presence of a broad band in the visible spectral range, which is a typical resonant range forseveral silver nanostructures[1] and, at the same time, the absorption spectral range of the BHJ used. In addition, a narrow absorption peak at 327 nm is detected. An in-depth analysis of literature has shown that this unique absorption resonance is related to the excitation of Ferrell-Berreman bulk plasmon-polaritons[2] that are more pronounced for silver films respect to other plasmonic metals because of its small Ohmic losses[3]. The presence of bulk plasmon polaritons could be related to the occurrence of a particular condition named as Epsilon-near-Zero (ENZ). This means that at specific wavelengths (depending on HMM building materials, geometry and metal/dielectric fill fraction) a component of the dielectric tensor crosses the zero. The opposite situation, in which a component of the dielectric tensor

diverges, is known as epsilon-near-pole condition (ENP). The direction of these resonances depends mainly on the construction geometry of the HMM; for multilayer systems, the ENZ condition occurs parallel to the layers ($\varepsilon_{//}\rightarrow 0$) and the ENP condition perpendicular to the layers ($\varepsilon_{\perp}\rightarrow\infty$) while for metallic nano-wire arrangements the opposite is verified. A schematization of this behavior is represented in Figure 4.4.

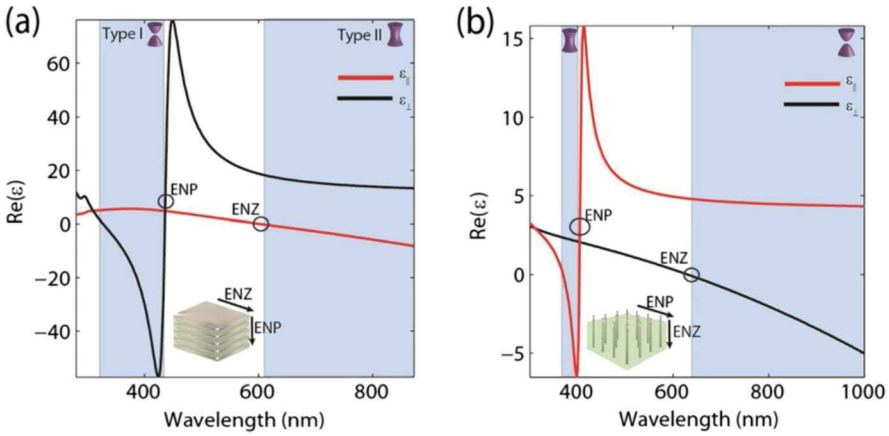


*Figure 4.4- Examples for the real part of the dielectric permittivity for a) multilayers and b) nanowires HMMs; Type I and Type II hyperbolic regions as well as ENZ and ENP pointsare indicated for both structures[4].*

From a physical point of view, these different conditions for ENZ and ENP behavior can be explainedas a function of allowed free electrons motions within the material; in multilayered structures, the motion of electrons is nearly free within each metal plane whileit is confined in the perpendicular direction. Thus, the parallel effective medium parameter follows the frequency dispersion relation of an effective metal, creating an ENZ condition only in this direction; conversely, the frequency dispersion of the perpendicular permittivity follows that of an effective dielectric, accompanying the ENP resonance[4]. For multilayer systems, within the Effective Medium Theory, the effective $\varepsilon_{//}$ and $\varepsilon_{\perp}$of an HMM can be calculated from the following simplifiedEquations 1:

$$\varepsilon_{//} = \frac{t_D\varepsilon_D + t_M\varepsilon_M}{t_D + t_M}$$
$$\varepsilon_{\perp} = \frac{t_D t_M\left(\varepsilon_M + \varepsilon_D\right)}{t_D\varepsilon_M + t_M\varepsilon_D} \qquad (1)$$

where $t_D$ and $t_M$ are the thicknesses of dielectric and metallic layers, respectively, and $\varepsilon_D$ and $\varepsilon_M$ are their relative dielectric permittivity. From Equations 1 it is clear that $\varepsilon_{//}$ can vanish (ENZ frequency) only for frequencies when the following condition holds:

$$\frac{\varepsilon_D}{\varepsilon_M} = -\left(\frac{t_M}{t_D}\right) \tag{2}$$

The effective perpendicular permittivity has a resonant pole at a frequency for which Equations 3 is satisfied:

$$\frac{\varepsilon_D}{\varepsilon_M} = -\left(\frac{t_D}{t_M}\right) \tag{3}$$

Recently, it has been demonstrated that the above conditions for ENZ and ENP (usually verified for different wavelengths within a HMM) could be reached simultaneously, if materials and geometrical restriction during the construction of the HMM are being followed, leading to a HMM where an epsilon-near-zero-and-pole is obtained for the same wavelength[5]. It has to be noted that, in multilayer structures, as well as in pure silver, particular conditions exist for a resonant ENZ effect occurring in the perpendicular component of the dielectric constant[2a]. In our resulting HMMs, the absorption peak at 327 nm occurs at the ENZ condition of pure silver films and it is due to the excitation of the so-called Ferrell-Berreman modes bulk plasmon polaritons (BPPs). Indeed, due to the very thin metallic layers required for a HMM construction, in addition to the long- and short-range plasmon polaritons that propagate along the interface, also these BPPs modes whose energy propagates within the bulk multilayer can be excited by light at frequency near the epsilon near zero condition[2a], giving a higher absorption at this specific wavelength. Our future work in this field will be focused on verifying if it is possible to generate free charges from this additional absorption at 327 nm.

## 4.3 HMMs WITH THERMALLY-RECONFIGURABLE PROPERTIES: an Ag/$TiO_2$ -BASED SYSTEM

Multilayer HMMs are known to be artificial mediawith optical properties that can be specifically designed for different applications. Indeed, as revealed by Equations 1, it is possible to design a structure with specific and desired values for the effective dielectric tensor components ($\varepsilon_{//}$ and $\varepsilon_{\perp}$), by choosing the proper materials (metal – $\varepsilon_M(\omega)$ – and dielectric - $\varepsilon_D$) and their relative thicknesses ($t_M$ and $t_D$). In this way, the frequency of the ENZ or ENP transitions, for example, can be chosen. However, once the components are assembledwithin a given HMM structure, it is not possible to tune the value for the ENZ or other conditions, unless thickness or refractive indices are changed.

To overcome this limit, designing a specific dielectric whose properties could be tuned by external stimuli can represent a successful strategy. To ensure the ENZ frequency occurs in the visible spectral range, a dielectric with a high refractive index is required. According to this consideration, unsintered $TiO_2$ - obtained through a sol-gel process – can represent a solution.Indeed, morphological and optical properties of as-prepared $TiO_2$ films are extremely sensitive to any temperature and moisture changes. Morphological, optical and, eventually, electrical changes induced by the environment are usually detrimental for applications of this compound in opto-electronic devices. Therefore, $TiO_2$ films are often sintered in order to achieve a major stability. For our purposes instead, these intrinsic environmental sensitivityof the sol-gel- $TiO_2$-containing films could be used to introduce further tunability in HMMs even after their physical realization. Moreover, with the aim of tuning the refractive index of the conceived $TiO_2$-based dielectric layer, poly(vinylpyrrolidone) (PVP) was added to the $TiO_2$ matrix. An organic dye (Cumarin 522B) was also addedto the $TiO_2$ + PVP system to experimentally confirm (through the measuring of its decay lifetime) the hyperbolic nature of the multilayer structure, obtained alternating this noveldielectric layer and Ag.Thin films of $TiO_2$were prepared by slightly modifying the procedure reported elsewhere[6], starting from titanium-tetraisopropoxide ($Ti(OC_3H_7)_4$) as a precursor. The process involved two steps: first, an acidic solution of ethanol was prepared by adding HCl 2M to the pure ethanol solvent (14µL/1mL); $Ti(OC_3H_7)_4$ and anhydrous ethanol were then mixed (140µL/1mL) and added drop-wise to the first solution while

stirring. For PVP- and/or dye-doped solutions, 2% w/w of PVP 10.000 and/or 3% w/w of Coumarin 522B (with respect to $Ti(OC_3H_7)_4$) were added to the HCl/Ethanol solution before mixing with the $Ti(OC_3H_7)_4$solution. The final solution was spread on a clean glass substrate by using a 0.45 µm poly(tetrafluoroethylene) (PTFE) syringe filter and then spun at 3000 RPM for one minute, leading to the following different samples:

- $TiO_2$ (sintered – 500°C for 45 minutes – and unsintered);
- TP ($TiO_2$ + PVP);
- TPD ($TiO_2$ + PVP + Dye);
- TD ($TiO_2$ + Dye).

Reference films of PVP + Dye (PD), PVP only and Dye only (D) were obtained by spin coating, with the same conditions,the corresponding solution in ethanol.

The detailed reaction mechanism for the $TiO_2$ nanoparticles nucleation is not yet fully understood for this type of non-aqueous synthesis, but it is supposed to proceed via a two-step process[7] involving a ligand exchange first and then an ether elimination, as shown in the following Scheme 4.1:

1) Ligand exchange:


2) Ether elimination:

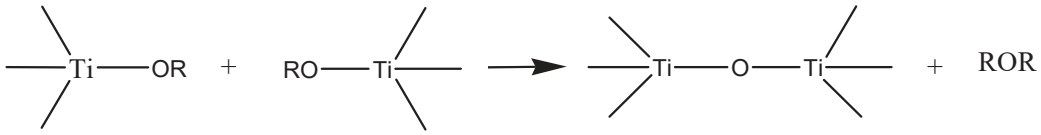


EtOH: ethyl alcohol
iPrOH: isopropyl alcohol
R: iPr/Et

*Scheme 4.1- Proposed reaction mechanism for $TiO_2$ formation.*

Ellipsometric optical characterizations were conducted on all types of prepared samples, as reported in Figures 4.5 a and b. In these Figures, a tuning (at room temperature) of the real refractive index among these samples is illustrated and, as shownFigure 4.5 b, a peak

in K due to the absorption of the dye (at λ = 422 nm) in TD e TPD films is recorded. Moreover, dye absorption is stronger for TPD than for TD, because PVP acts a favorable host medium for the dye, meaning that a major amount of dye is held during the TPD film deposition.

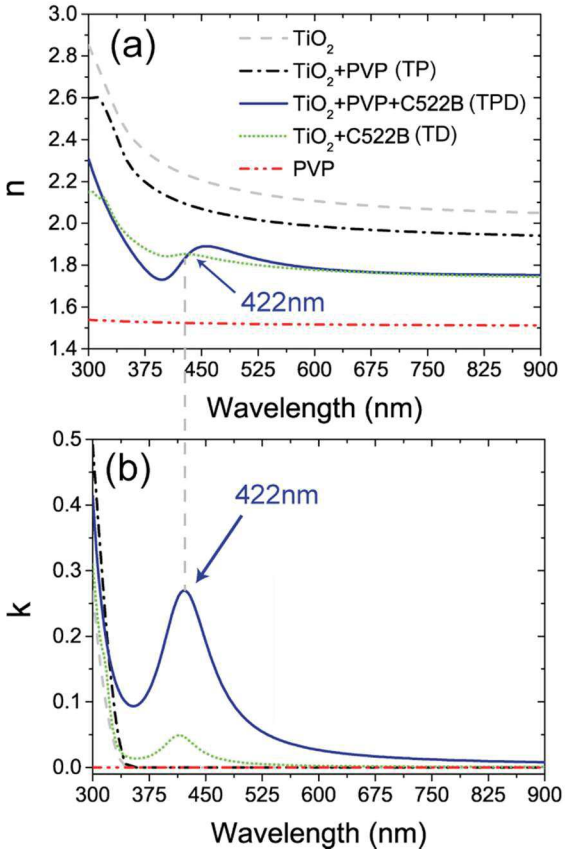


*Figure 4.5- a) real and b) imaginary refractive indices of all samples under study.*

Variable-temperature ellipsometric measurements conducted on $TiO_2$, TPD and TD films, reveal that a heating process is able to contract the thickness of these films. Such a contraction is reversible from room temperature to 80°C and approaches the limits of a 20 nm-reduction between unsintered (about 80 nm) and sintered (about 60 nm) $TiO_2$ films (ellipsometrically detected) as the temperature increases. At 160°C this contraction process becomes irreversible. Furthermore, as shown in Figure 4.6, for samples containing both the $TiO_2$ and the dye, this contraction is coupled with a color switch from yellow to orange. This color change could be due to the formation of dye aggregates as a result of the improved

mobility of these films upon heating, causing the red-shift of their absorption. For this reason, it appears clear that unsintered $TiO_2$ could act as a thermally reconfigurable template for tuning the absorption properties of the embedded dye.

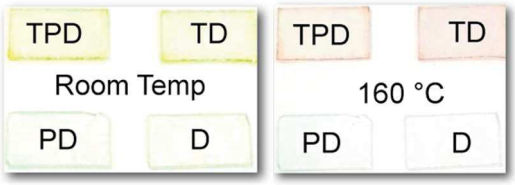


*Figure 4.6- Photographs of samples at room temperature and after heating at 160°C.*

The reversible temperature-induced contraction for the unsintered $TiO_2$- containing samples could be attributed to water absorption/desorption for the environmental moisture, being the $TiO_2$ a hygroscopic compound. Indeed, the same color switch was obtained for the yellow TPD film introduced and then stored (at room temperature) in a nitrogen atmosphere (less than 1 ppm of water), where it immediately became orange. The yellow color was recovered over a couple of minutes after the film was again exposed to ambient atmosphere. Ellipsometric measurements conducted at room temperature and at 160°C for the TPD samples, shown in Figures 4.7 a and b, reveal a red-shifted of about 45 nm both in absorption (see the inset also) and transmittance when heating these samples. Moreover, the real refractive index of TPD layer increases upon this heating, towards the values of the sintered $TiO_2$ (see Figures 4.7 a and 4.5 a for comparison).

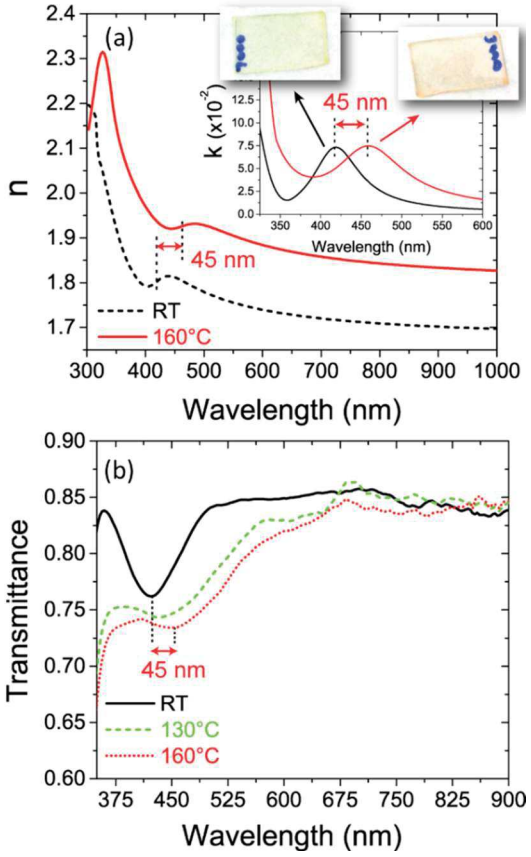


*Figure 4.7- a) n and k (inset) and b) transmittance spectrum for the TPD film at room temperature and at 160°C.*

These experimental measurements confirm the hypothesis that, if this engineered dielectric layer is used to prepare a hyperbolic system, both these temperature-induced variations may be used to tune the ENZ frequency of the corresponding HMM.

A three-bilayer HMM was fabricated using evaporated silver as a metal and TPD as a dielectric. From EMT calculations, at room temperaturethe ENZ condition is obtained at λ = 560 nm; at shorter wavelength the system behaves like an effective dielectric, while at longer ones like a Type-II HMM, as shown in Figures 4.8 a, b. Experimental and simulated reflectanceare shownin Figure 4.8 c.

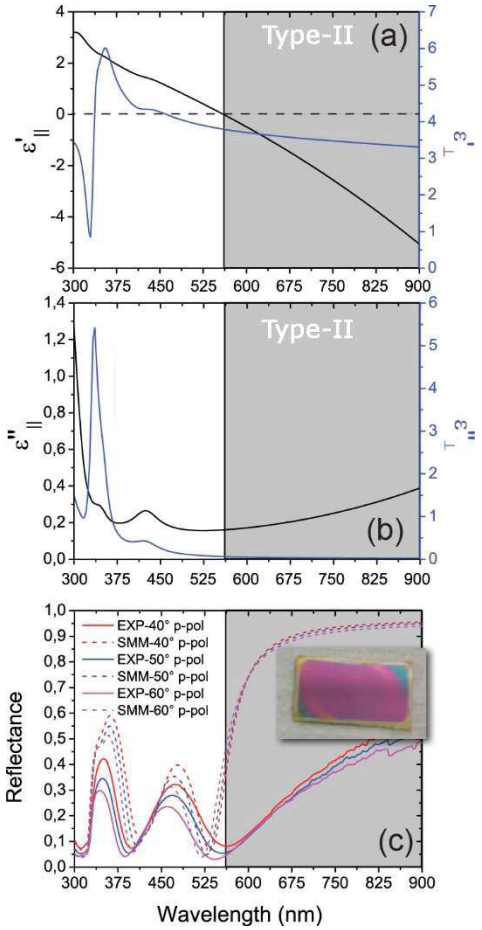


*Figure 4.8- EMT calculation for the a) real and b) imaginary part of the effective dielectric permittivity of the HMM; c) experimental and simulated reflectance of the HMM. The inset is a photograph of the three-bilayers TPD/Ag HMM showing a bright magenta color.*

In the last Figure, the two dips in reflection correspond to excitation of bulk plasmon polariton modes[8]. Thermal reconfigurability of the three-bilayer HMM was ellipsometrically detected as a reversible 10 nm blue shift in both transmission and reflectionspectra, also after three heating cycles (see Figures 4.9 a and b), between room temperature and 80°C.

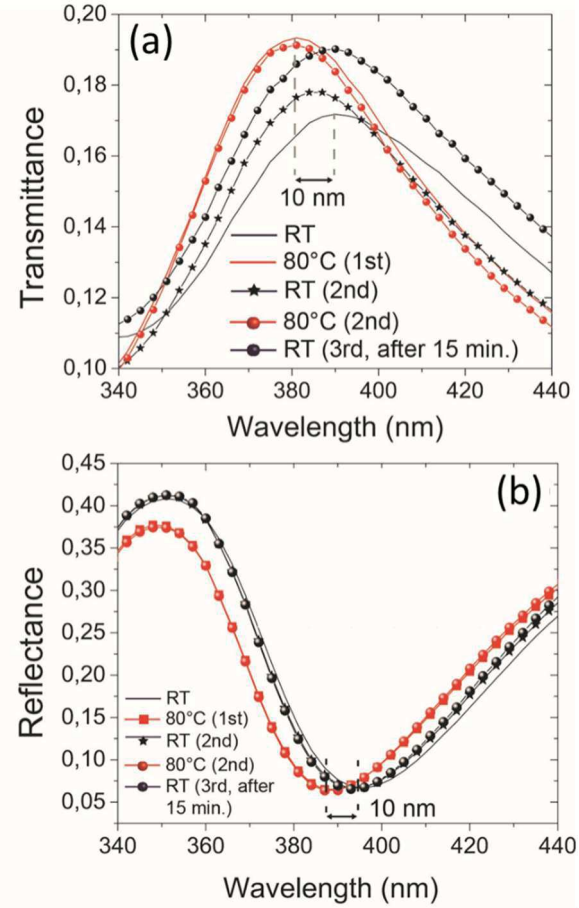


*Figure 4.9- Ellipsometrical a) transmittance and b) reflectance showing a reversible thermal tuning for the TPD/Ag HMM within the room – 80°C temperature range.*

As shown in Figure 4.10, EMT calculations revel that the wavelength for the ENZ condition of the studied hyperbolic structure has experienced a blue shift of 10 nm, passing from 560 nm to 550 nm, confirming the trend previously observed for transmission and reflection.

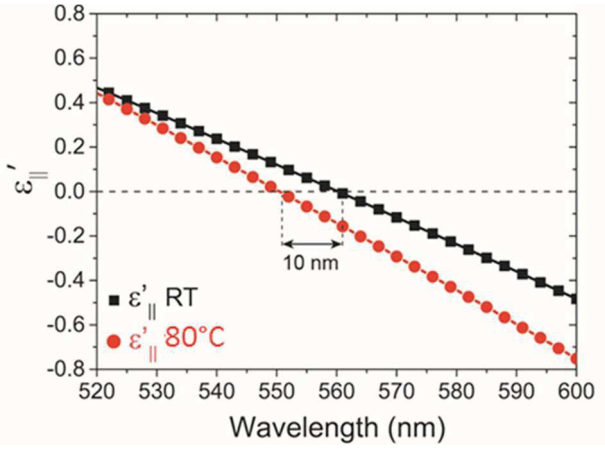


*Figure 4.10- EMT calculated blue shift of the HMM ENZ transition induced by heating.*

The emission properties of the dye were studied to point out the role of its interaction with $TiO_2$. Figure 4.11 a showshow the emission wavelength is red-shifted for both TD and TPD films, respect to the emission of the PD film, while in Figure 4.11 b the luminescent intensity decay of these samples is presented.Table 4.1 summarizes these data.

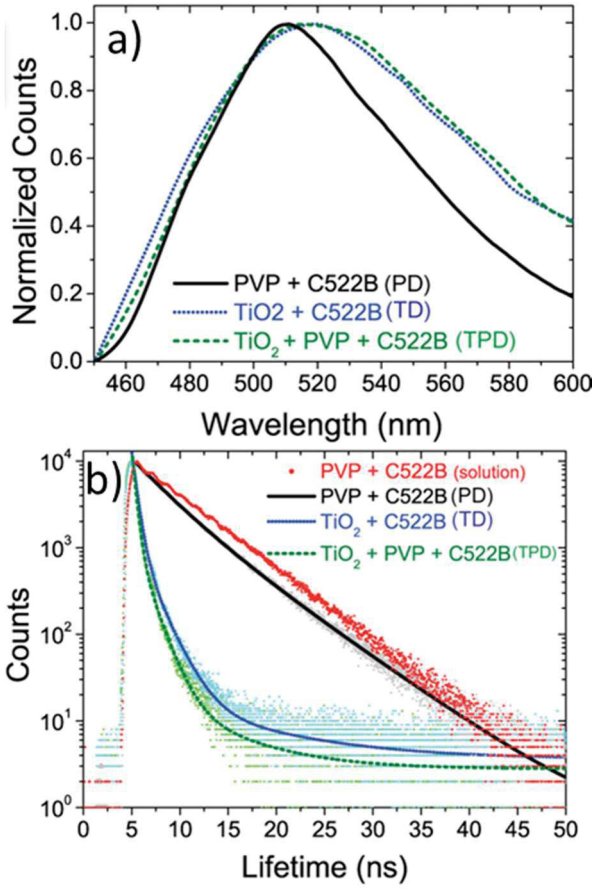


*Figure 4.11- a) Luminescence spectra and b) fluorescence intensity decay, recorded at the emission maximumfor the studied samples.*

| *Sample* | $\lambda_{em}$ / *nm* | $\tau_2$ / *ns(relative weight of decay lifetime)* | $\tau_1$/ *ns (relative weight of decay lifetime)* |
|---|---|---|---|
| *PVP + C522B (sol) - $PD_{solution}$* | **512** | **4.83** | **#** |
| *PVP + C522B - PD* | **511** | **4.57 (56.43)** | **1.8 (43.57)** |
| *TiO2 + C522B - TD* | **518** | **1.89 (29.62)** | **0.46 (70.38)** |
| *TiO2 + PVP + C522B - TPD* | **519** | **1.65 (27.18)** | **0.37 (72.82)** |

*Table 4.1- Luminescence intensity decay for the studied samples.*

From these measurements, the role of $TiO_2$ in the photo-physics of the dye is clear. Indeed, it is possible to note that the PD solution shows a single lifetime (4.83 ns) while in PD film two lifetimes are obtained the longer one (4.57 ns) due to isolated dye molecules (like in solution) and a shorter one (1.8 ns) due to the presence of aggregated molecules in the film. Both films containing $TiO_2$, instead, show two much faster decay times: $\tau_2$ attributed to aggregates in the film and the very short $\tau_1$ attributed to an energy transfer process to the $TiO_2$.[9] The fluorescence decay of the dye in the HMM ($\tau_1$) was also recorded, to confirm the hyperbolic nature of the prepared sample. Indeed, an almost constant lifetime of the fluorophore as a function of the emission wavelength in both the dielectric ($\lambda < 560$ nm) and the hyperbolic regime (Type-II HMM for $\lambda > 560$ nm) was observedin the HMM, but not in the PD film (no hyperbolic regime –used as reference), as shownin Figure 4.12. This is due to the presence of so-called high-K modes, typical in HMMs, providing a faster relaxation channel for the excitonic states[5].

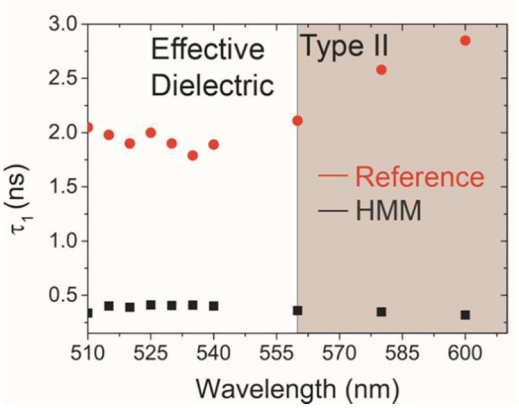


*Figure 4.12- Fluorescence lifetime of the dye in the HMM and in a PD layer (reference) as a function of the emission wavelength.*

In conclusion, in this work a successful method to tune the ENZ frequency of a HMM is presented. This method is based on the use of a thermally reconfigurable dielectric layer based on a sol-gel-derived and unsintered $TiO_2$ thin layer that undergoes a physical contraction and an increase of refractive index upon heating. This process is completely reversible in a temperature range from room temperature to 80°C. The presence of a dye allows an easy visual detection of the tunable properties of the TPD layer. A complete optical and photophysical characterization was carried out for both the TPD layer and the HMM (TPD/Ag), revealing the fundamental role of $TiO_2$ as a thermally reconfigurable template for extremely tunable HMMs.

## 4.4 BIBLIOGRAPHY

**[1]a)** A. I. Maaroof, D.S. Sutherland, J. Appl. Phys. D: *Appl. Phys*., **2010**, 43, 405301;
**b)** V. Amendola, O.M. Bakr, F. Stellaci, *Plasmonics*, **2010**, 5, 85.
**[2]a)** W.D. Newman, C.L. Cortes, J. Atkinson, S. Pramanik, R.G. DeCorby, Z. Jacob, *ACS Photonics*, **2015**, 2, 7;
**b)** R.A. Ferrell, *Phys. Rev*., **1958**, 111, 1214;
**c)** D.W. Berreman, *Phys. Rev*., **1963**, 130, 2193.
**[3]** G.V. Naik, V.M. Shalaev, A. Boltasseva, *Adv. Mater*., **2013**, 25, 3264.
**[4]** P. Shekkar, J. Atkinson, Z. Jacob, *Nano Convergence*, **2014**, 14:1.
**[5]** V. Caligiuri, R. Dhama, K.V. Sreekanth, G. Strangi, A. De Luca, *Sci. Rep*., **2016**, 6:2002.
**[6]** J.G. Lee, J.H. Cheon, M.S. Yang, D.K. Lee, J. H. Kim, *J. Nanosci. Nanotech*., **2012**, 12, 6026.
**[7]**M. Zimmermann, G. Gamweitner, *Cryst. Eng. Commun*., **2012**, 14, 8562.
**[8]** I Avrutsky, I. Salakhutdinov, J. Elser, V. Podolskiy, *Phys. Rev. B*, **2007**, 75, 241402(R).
**[9]a)** J.K. Mor, J. Basham, M. Paulose, S. Kim, O.K. Varghese, A. Vaish, S. Yoriya, C.A. Grimes, *Nano Lett.*, **2010**, 10, 2387;
**b)**B.E. Hardin, A. Sellinger, T. Moehl, R. Humphry-Baker, J.E. Moser, P. Wang, S.M. Zakeeruddin, M. Grätzel, M.D. McGehee, *JACS,* **2011**, 133, 10662.

# CHAPTER 5:
# EXPERIMENTAL TECHNIQUES

## 5.1 SAMPLE PREPARATION FOR J-V MEASUREMENT

Samples for photovoltaic cells in normal configuration were prepared on Indium Tin Oxide (ITO) coated glass (UNAXIS, 115-120 nm for ITO thickness, sheet resistivity 12 Ω/□) as anode. For the cathode, Al or LiF/Al were used, depending upon the different cases. The different steps involved in the complete preparation of samples with a structure illustrated in Figure 5.1, are described in the following sections.

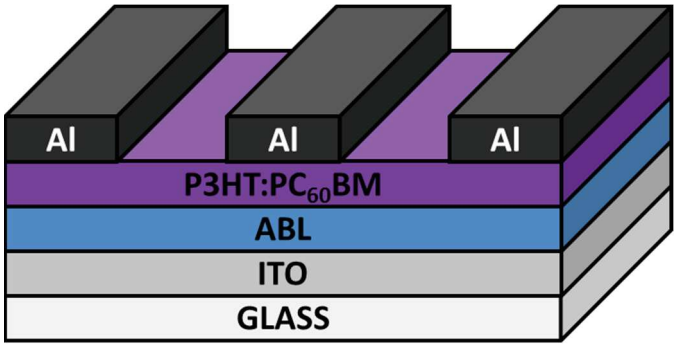


*Figure 5.1- Schematic representation of solar device under study.*

### 5.1.1 Substrate preparation

Patterned ITO glasses with different shape were obtained using either a photolithographic or an etching process. For photolithography, the shadow masks shown in Figure 5.2 were used, with a positive photoresist (Microposit S1805 Photoresist, Shipley Company) and the appropriate developing solution (Microposit MF-319 Developer, Shipley Company). The unwanted ITO was finally etched with acidic solution – 1:1:0.1 HCl (37%):$H_2O$:$H_2SO_4$(95%), for 5 minutes at 50°C. All the processing parameters (timing and temperature used) were optimized to obtain a well-defined step between the glass substrate and ITO. A mechanical profilometer (Dektak 8, from VEECO) was used for the

characterization of the etched substrates. It is noteworthy that the optimization of the photolithographic process is essential to accurately define the active area for the subsequent current-voltage measurements.

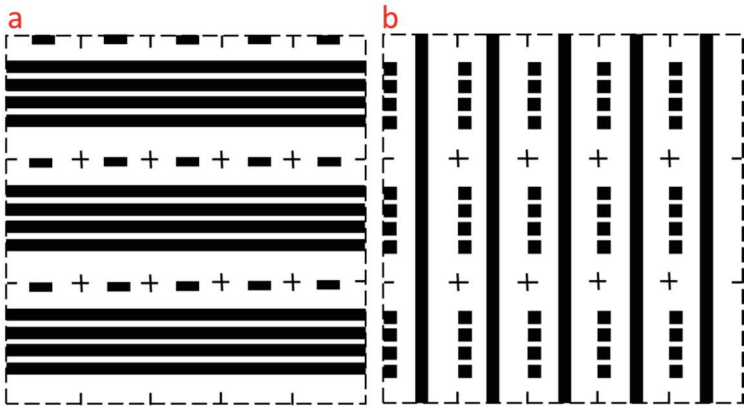


*Figure 5.2- Masks used during photolithography for ITO electrode.*

To obtain electrodes with a different ITO pattern, a simpler and faster etching procedure that does not require the photolithographic step was used. Briefly, a tape-strip was applied on the ITO regions (grey in Figure 5.3) that must be protected from the etching process. The unwanted ITO was removed through the reaction of Zn powder with an aqueous solution of HCl 2M. When using this faster procedure, a shadow mask to define the illuminated active area during J-V measurements is necessary. This mask is shown in Figure 5.4

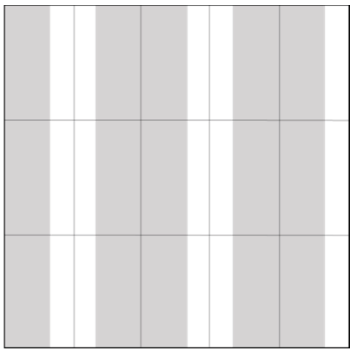

*Figure 5.3- Scheme for Zn-HCl etching of ITO.*

*Figure 5.4- Metallic mask used to define active area during J-V measurements.*

After the etching treatments, the glass plates were cut in smaller size of 1.5 x 2.5 $cm^2$. The resulting substrates were cleaned in an ultra-sonicator using four different solvents: distilled water and soap, distilled water, acetone and isopropyl alcohol, each bath lasting 20 minutes. The cleaned substrates were then dried with a nitrogen gun. An air plasma treatment (Diener Electronics, Model Femto, performed at 100% power for 5 minutes) or a further cleaning bath (RCA), as described in the following, are necessary to make the ITO surface more hydrophilic and guarantee its wettability during the PEDOT:PSS deposition. Furthermore, these treatments change the ITO work-function from about 5.1 eV (starting point of our ITO substrate) to 5.6 eV (Plasma) and 5.3 eV (RCA) respectively (Ambient Kelvin Probe KP020, KPTechnology). The RCA cleaning bath involved the preparation of a 1:1:5 solution of $H_2O_2$ : $NH_3$(OH) 30% : $H_2O$ - kept at about 70-80°C - in which ITO-covered glasses have been dipped for 15 minutes. Then, these substrates were rinsed with ultra-pure water and dried with a nitrogen gun.

#### 5.1.1.1 Work-function measurement: the Kelvin method

The Kelvin method is an experimental technique for measurement the local work function (WF) differences between a conducting sample and a reference tip in a non-contact, non-invasive way over a wide temperature range. It is a relative and indirect technique and requires that the work function of the tip ($\phi_{tip}$) to be known to calculate the WF on unknown sample ($\phi_s$). The Kelvin probe (KP) technique measures the contact potential difference ($V_{CPD}$) between the tip and the sample being in close proximity, but without electrical contact between them (Figure 5.5 a). In this condition, their Fermi levels align, with respect to the vacuum level, at energies corresponding to the respective work functions. As the tip and the sample are electrically connected through an external circuit

(Figure 5.5 b), electrons flow from the compound with the smaller work function to the sample with the larger one. This causes an alignment of the Fermi levels and a slight charging phenomenon of their surfaces, creating an electric field between the tip and the sample. The electron flow stops once the electric field between them compensates for the work function difference. In this equilibrium state, the potential associated with the electric field exactly equals the work function difference between the samples. In this condition, the contact potential difference is calculated from Equation 1:

$$qV_{CPD} = \phi_s - \phi_{tip} \tag{1}$$

where q is the charge of one electron. Thus, the WF of the sample (ϕs) can be obtained relative to the WF of the tip ($\phi_{tip}$), if the $V_{CPD}$ can be measured.

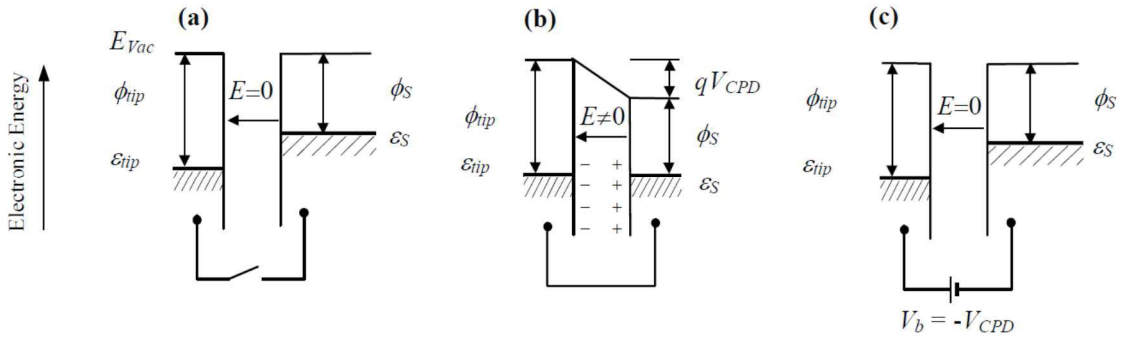


*Figure 5.5- Electron energy level diagram for a) two samples without contact; b) samples in electrical contact through an external circuit; c) external circuit including the external potential $V_b$.*

Usually, measurement of $V_{CPD}$ is conducted in a vibration capacitor configuration, according to which the tip and the sample are approximated to oscillating capacitor plates. The Kelvin probe (*i.e.* the tip) is vibrated at a certain frequency ω. The alternate current generated by the oscillations (due to the varying distance between the plates) may be monitored and can be expressed as:

$$i(t) = V_c \frac{dC_c}{dt} \tag{2}$$

where $\frac{dC_c}{dt}$ indicates the varying capacitance due to the tip vibration and $V_c$ is the voltage across the capacitor. Introducing an external potential $V_b$ (Figure 5.5 c) in this circuit, the voltage across the Kelvin capacitor $V_c$ can be expressed as:

$$V_c = V_{CPD} + V_b \tag{3}$$

A unique point exist in which the voltage $V_c$ equals to zero: $V_{CPD} = - V_b$ . At this point, even the current associated with tip vibration is zero. The work function difference between the plates (see Equation 1) is thus equal and opposite to the external potential necessary to produce a zero output signal. In the Kelvin method, a tip calibration is necessary before measuring the WF of a sample. This procedure is conducted like a typical WF measurement with a standard sample with known WF, to set the WF of the tip.

### 5.1.2 PEDOT:PSS deposition

As a hole conductive material and buffer layer between the ITO electrode and the active layer, a thin film of poly(3,4-ethylenedioxythiophene):poly(styrenesulfonate) – (PEDOT:PSS 1:6 w/w, 1.3 – 1.7 % w/V in water, Heraeus Clevios PVP Al 4083, H.C. Starck) – was used. Its chemical structure is shown in Figure 5.6.

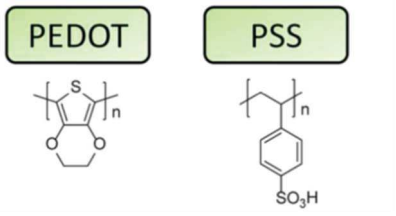


*Figure 5.6- Chemical structure of PEDOT:PSS.*

This film was obtained by spin coating (CaLCTec Instruments, Model Fr10KPA-HC) the polymer dispersion onto glass/ITO substrates. In order to avoid particles formation on the ITO surface, resulting in a inhomogeneous PEDOT:PSS layer, the dispersion was double

filtered with PVDF filters with a porosity of 0.45 µm and 0.20 µm. The substrate spinning was carried out at 3000 rpm for 1 minute. Using this high speed, a homogeneous film with thickness ranging from 30 nm to 40 nm (depending on pre-treatment used for the substrate) can be obtained. After spin coating, the connection for the ITO electrodes were cleaned with a cotton stick slightly wetted with water. After that, the PEDOT:PSS coated substrates were annealed at 140°C for 15 minutes on a hot plate to remove any residual solvent. The PEDOT:PSS covered substrates were then transferred inside a nitrogen glove box to avoid any further absorption of water and oxygen. These spinning conditions and annealing time/temperature give a PEDOT:PSS film with the best photovoltaic performances.

### 5.1.3 Active layer deposition

The active layer studied in this thesis consists in the polymer:fullerene blend formed by regio-regular poly(3-hexilthiophene-2,5-diyl) - P3HT (Rieke Metals, Inc., Electronic grade) – and by the soluble fullerene derivate Phenyl-$C_{61}$-Butyric acid Methyl ester - $PC_{60}BM$ (Nano-C®). Their chemical structures are shown in Figure 5.7.

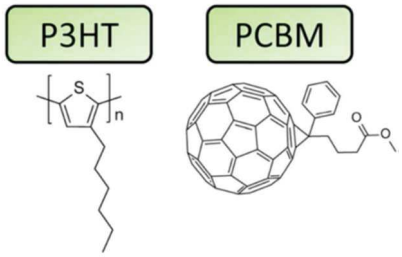


*Figure 5.7- Chemical structure of P3HT and $PC_{60}BM$.*

Chlorobenzene (anhydrous, 99.8%, Sigma-Aldrich) solutions of P3HT:$PC_{60}BM$ (17 mg/ml total concentration, P3HT:$PC_{60}BM$ ~ 1:0.7 w:w) were prepared and stirred overnight in inert atmosphere before being used. This active layer was spin coated (CaLCTec Instruments, model Fr10KPA-HC) onto the PEDOT:PSS layer in a glove box, using a syringe with a 0.22 µm PTFE filter for solution deposition onto the PEDOT:PSS-covered substrates. The

spinning speed and time of 700 RPM and 1 minute were used; in this way a film thickness of about 100-120 nm was obtained. Depending on the chosen electrode, a different annealing treatment was used. For lithium fluoride/aluminum - LiF/Al – cathode, the films were immediately annealed after their deposition, at 150°C for 30 minutes. If Al was used as the top electrode, a pre-annealing at 75°C for 10 minutes was conducted to remove most of the residual solvent in the films; after the electrode thermal deposition, a post-annealing treatment was carried out at 150°C for 30 minutes. Sample annealing was carried out with a Präzitherm precision hot plate model PZ 28-2. For plasmonic solar devices, spinning rates of 1500 and 3000 RPM were also used to obtain thinner films (thickness range 35 – 45 nm).

### 5.1.4 Metallic cathode deposition

For the cathode deposition, the spin coated films were immediately transferred into the evaporator system (Kurt J. Lesker, PVD75GB) connected to the glove box. Evaporation through the shadow masks shown in Figures 5.8 – depending on the patterned ITO glasses used in different cases – leads to four active pixel for each substrate, with active areas of 8.75 $mm^2$, 5 $mm^2$ and 11,25 $mm^2$ respectively.

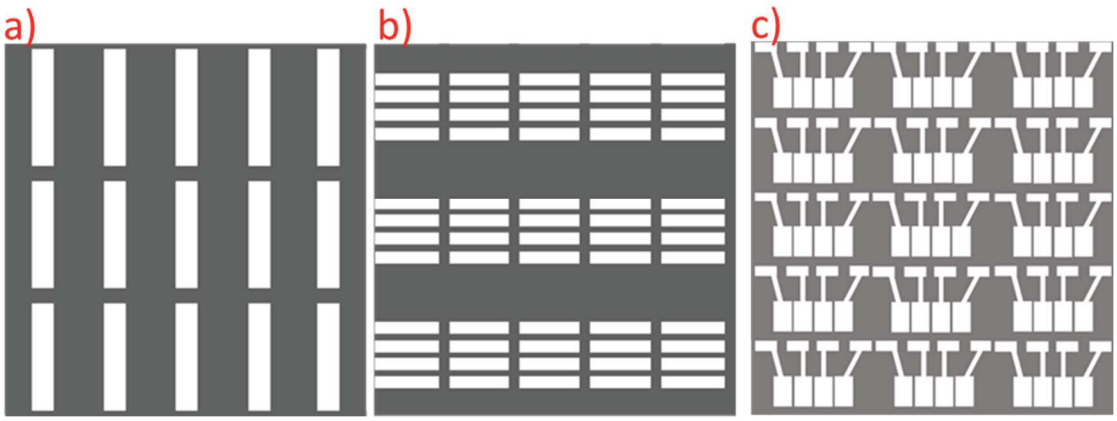


*Figure 5.8- Shadow masks used during the evaporation of the metallic cathode; different shapes correspond to different ITO-patterning for the anode.*

Two types of cathodes were used; LiF/Al or Al. In the first case, LiF powder was evaporated at a rate of about 1-2 Å/s to obtain a thickness of 0.7-0.8 nm, followed by the deposition of

200 nm of Al at a rate of 1.5 – 2 Å/s, without breaking the vacuum inside the evaporation chamber. In the latter case, only 200 nm of aluminum were evaporated onto the samples. All these thermal evaporations were carried out at the base pressure of $1 \cdot 10^{-6}$ mbar. For plasmonic solar cells different Al thicknesses were used, ranging from 5 nm to 200 nm. The thickness of the deposited electrodes was measured through a quartz microbalance during the evaporation and double-checked with a stylus profilometer or by ellipsometrical characterization. Once made, all devices were stored in a nitrogen-filled glove box for testing.

### 5.1.5 J-V characteristic measurement

The current-voltage characteristics curves were measured with a Keithley (model 2400) digital source meter controlled by a LabVIEW software (DeltaE S.r.l.), which allows to set all the experimental parameters to perform the J-V measurement (*i.e.* active area, voltage sweep range and direction, speed of recording). Irradiation of the samples was achieved with a solar simulator (Sciencetech, Model SS150) with an adequate set of filters to achieve a solar spectrum with AM 1.5G and intensity 100 $mWcm^{-2}$. The solar simulator intensity was set by using a calibrated Si photodiode (Hamamatsu S2386-44K). The sample holder was constructed in order to measure the characteristic curves and the external quantum efficiency in the four different active areas in one sample, using a manual or pc-controlled rotary switch for applying voltage on these areas. Once the solar simulator is switched on, stabilized and calibrated, measurements on devices can be recorded, under dark and illumination condition, by applying a voltage on the solar cell and measuring the current flowing through it.

## 5.2 SAMPLE PREPARATION FOR ELECROPOLYMERIZATION

### 5.2.1 Substrates preparation

Substrates for electropolymerization consist of Indium Tin Oxide (ITO) coated glass (UNAXIS, 115-120 nm ITO thickness, sheet resistivity 12 Ω/□), etched as in Figure 5.2 b according to the above described photolithographic process. These substrates (1.5 x 2.5 $cm^2$ area) were cleaned in an ultrasonic bath with acetone, NaOH 5% solution, distilled water, and isopropyl alcohol, each bath lasting 15 minutes.

### 5.2.2 Electropolimerization of organo-metallic complexes

Electropolymerizations were carried out by cyclic voltammetry, performed with an AUTOLAB PGSTAT 30 potentiostat/galvanostat controlled by the GPES v. 4.9 or NOVA 1.10 software. A conventional three-electrodes setup was employed, with a Pt wire as counter-electrode, an Ag wire as a pseudo-reference electrode and a Pt-disk or a 2 mm-wide ITO stripes on glass as working electrode. Tetrabutylammoniumhexafluorophosphate (0.1 M) was used as supporting electrolyte. Experiments were performed in a dry, freshly distilled and degassed (Ar) dichloromethane solution with several concentrations, ranging from $5 \cdot 10^{-5}$ M to $1 \cdot 10^{-3}$ M. The electropolymerization process was conducted by continuously cycling the applied potential around the oxidation potential of the studied complexes (from -0.2 V to +1.7 V) at several scan rates and for different numbers of cycles. Films thicknesses (in the range of 10 to 600 nm) were measured with a stylus profilometer (VEECO, DEKTAK 8). After electropolymerization, the resulting yellow films were aged overnight in a dichloromethane vapor-saturated atmosphere, before being washed with freshly distilled dichloromethane to remove traces of electrolyte and of unreacted monomers and to prepare them for electrode deposition by physical vapor deposition process (ca. 300 nm at the base pressure of $10^{-6}$ mbar). Figure 5.9 shows the resulting geometry for this sample.

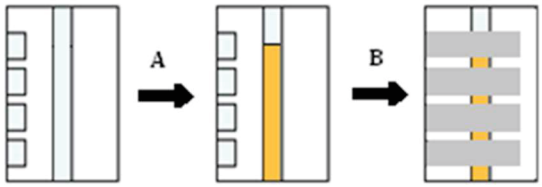


*Figure 5.9- Schematic representation of the prepared sample; etched ITO-glass, A) deposited electropolymerized film and B) Al electrodes.*

## 5.3 SAMPLE PREPARATION FOR PHOTOCONDUCTIVITY AND MOBILITY MEASUREMENTS

### 5.3.1 Cells for photoconductivity measurement on monomeric complexes

Cells for photoconductive measurements on monomeric complexes were prepared by overlapping etched ITO substrates, obtained through the previously described photolithographic process. Figure 5.10 shows a schematic representation of the cell geometry used, with an active area of 0.6 $mm^2$.

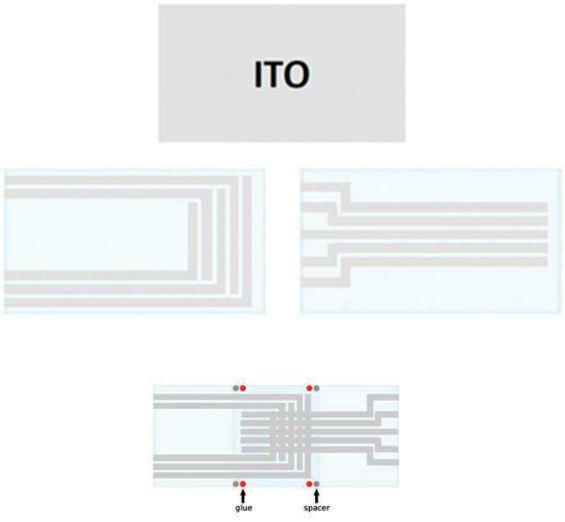


*Figure 5.10- Schematic representation of cells used for photoconductive measurements of monomeric complexes.*

These cells have a typical thickness ranging between 4 and 5 µm, controlled by means of 1.7 µm spacers dispersed in a thermal resistant glue. The real thickness of the resulting cells

was measured by recording their interferometric pattern in a UV-Vis spectrophotometer (Agilent 8453), according to Equation 4:

$$d = \frac{x\lambda_1\lambda_2}{2|\lambda_1 - \lambda_2|n} \quad (4)$$

where *n* is the air refractive index (≈ 1) and *x* is the number of periods in the interferometric pattern between $\lambda_1$ and $\lambda_2$ (both chosen at minima or maxima points in the sinusoidal signal). These cells were filled by capillarity on a hot stage at a temperature slightly above the melting point of the complexes. Rapid cooling to room temperature allowed the freezing of the melt into its amorphous and thermostable state.

### 5.3.2 Sample geometry for photoconductivity measurement on electropolymerized thin films

For measurements of photoconductivity on electrodeposited thin films, aluminum was chosen as a counter-electrode and deposited by thermal evaporation, with a shadow mask as in Figure 5.8 b, at the base pressure of $1 \cdot 10^{-6}$ mbar. The geometry of the obtained samples is illustrated in Figure 5.9. Three to four sites for measurement were obtained on each substrate, each one with an active area of about 5 $mm^2$. The choice of the materials for the electrodes was driven by the following considerations:

- One of the electrode has to be transparent to make the light reach the sample and, at the same time, to show the proper features for acting like WE during electropolymerization experiments;
- Both the electrodes must have a work-function (WF) well-matched to the HOMO/LUMO frontier orbitals of the complexes under study.

This latter consideration is very important to the aim of measuring a photocurrent. Indeed, if the dark current in the sample is too high due to carrier injection from the electrodes, the improvement in current obtained when illuminating the sample cannot be recorded. Table 5.1 summarized the WFs and the energetic levels for the materials used:

| *Materials* | *HOMO (eV)* | *LUMO (eV)* | *WF (eV)* |
|---|---|---|---|
| *ITO* | | | **-4.8 *** |
| *Al* | | | **-4.1 / 4.2** |
| *Au* | | | **-5.1** |
| *Pd-2 ; Pt-2 complexes* | **- 5.2** | **- 2.1** | |

*Table 5.1- HOMO/LUMO levels of used complexes and WF of the chosen electrodes; *ITO WF heavily depends on the treatments to which it is undergoing.*

From these considerations, electrodes chosen for photoconductivity measurements were ITO an Al; moreover, to avoid holes injection form the ITO electrode, the photoconductivity measurements have been performed polarizing negatively the ITO electrode.

### 5.3.3 Photoconductivity measurement

Photoconductivity measurements were performed using a solid-state laser (λ = 532 nm, Torus, Laser Quantum) as a light source. The light intensity was about 1 mW/cm$^2$ (International Light Technologies, ITL1400 Radiometer Photometer), slightly different every time the setup was changed when switching samples, and it was used to normalize the calculated photoconductivity values, according to Equations 5 and 6:

$$Photoresponce = \sigma_{photo} / I_{light} \quad (5)$$

$$\sigma_{photo} = i_{photo} \cdot d / V \cdot S \quad (6)$$

The photocurrent ($i_{photo}$) was obtained from the difference between light and dark currents ($i_{light} - i_{dark}$) measured with a source-meter (Keithley, 6517A), also used to apply a potential difference (V) to the electrodes. $I_{light}$ is the light intensity used to irradiate the sample, *d* is

the electropolymerized film thickness, and *S* the illuminated area of the sample between the two electrodes. For the measurements of photocurrent as a function of light intensity, neutral density filters were used to tune the laser light intensity.

### 5.3.4 Mobility measurement: SCLC method

Samples for mobility characterization through the Space-Charge-Limited Current (SCLC) consist in a thin film of organic semiconductor sandwiched between two electrodes. This technique requires one charge-injecting contact from one side (Ohmic contact) of the cell and one charge-blocking contact at the other side. When this condition holds, the measured current at a given applied voltage is only limited by the bulk mobility (transport-limited) of the material, instead of being injection-limited. Considering the energies of the frontier orbitals of the materials, ITO (on which the electropolymerized film is deposited) and Al or Au were chosen as electrodes (see Table 5.1). In all cases, the electron injection is avoided due to the high mismatch between the metal work-functions and the LUMO levels of the compounds. In this method, a typical current-voltage curve consists of a linear region at low voltage and a nearly quadratic region at higher voltage; this latter is referred to be the SCLC regime. At low applied voltages, the current is a linear function of the applied voltage (Ohmic resistive behavior) and depends simultaneously on two unknown parameters: the volume density of free charges and the charge mobility, as indicated in Equation 7:

$$i_{lin} = Ane\mu^{V_{lin}}\!/_{d} \qquad (7)$$

where A is the area of the sample between the two electrodes, n is the density of charges, e is the electric charge carried from an electron, μ is the sample charge mobility, $V_{lin}$ is the applied voltage in the Ohmic regime and d is the sample thickness. In the SCLC region, instead, the current depends only on the charge mobility and on other measurable characteristics of the sample, such as the dielectric constant and the geometry of the cell

(A and d). Hence, when this regime has been reached, a measurement of the currents allows for the determination of the mobility. It can be shown that the space-charge-limited current can be described by the Mott-Gurney Equation 8:

$$i_{SCL} = \frac{9}{8}\frac{A\varepsilon_0\varepsilon_r\mu V_{SCL}{}^2}{d^3} \tag{8}$$

where, $\varepsilon_0$ is the vacuum permittivity, $\varepsilon_r$ is the material relative dielectric constant, and $V_{SCL}$ the applied voltage. The voltage at which the slope of the i-V curves changes from linear to quadratic (the threshold voltage $V_T$) can be given by Equation 9:

$$V_T = \frac{8ned^2}{9\varepsilon_r\varepsilon_0} \tag{9}$$

The measured value of the mobility (from Equation 5) can be used in Equation 4 to obtain *n* (charge density) which, in turn, can be used in Equation 6 to obtain $V_T$. This step is very important because the matching between calculate and experimental $V_T$ indicates a reliable mobility measurement. These measurements have been conducted with a source meter (Keithley, 6517A) while the dielectric constant of the materials has been measured with an LCR meter (HP 4284A precision LCR meter) to measure the capacitance of each sample. From this value, it is possible to use Equation 10 to calculate the dielectric constant as:

$$\varepsilon_r\varepsilon_0 = \frac{C \cdot d}{A} \tag{10}$$

# CHAPTER 6:
# CONCLUSIONS AND PERSPECTIVES

The development of high efficiency organic solar cells could represent an effective alternative to inorganic-based solar conversion systems due to the abundance of materials, the theoretically infinite possibilities of synthesizing compounds with desired optical and electrical properties, the easy processability techniques for lowering the costs of production and ensuring a widespread availability of PV technology. The introduction of the BHJ concept, together with the development of new materials (as active and buffer layers) and the possibility to improve the absorption characteristics of organic layers using light managing techniques and plasmonic effects could represent strategies for improving the power conversion efficiency of OSCs, acting on different aspect of the functioning of these devices.

The first part of this work describes the preparation and characterization of novel photoconductive metallo-polymers to employ as anode buffer layers to replace PEDOT:PSS in normal configuration solar cells. This was done in order to verify if the use of an intrinsic photoconductor (*i.e*. a semiconductor that becomes more electrically conductive due to the absorption of light) as a buffer layer (ABL) could induce improvements on the power conversion efficiency due to its enhanced conductivity and charge transport properties to the electrodes. These polymers were prepared through an optimized electropolymerization process of the corresponding monomeric complexes (Pd(II) or Pt(II) as metal centers, 2-phenyl-pyridine and a Shiff base containing the electropolymerizable triphenylamino-group as the ligands) and are characterized by a higher photoresponsivity respect to the starting complexes. Moreover, through electropolymerization, thin polymeric films can be directly deposited on the ITO surface, leading to an improvement of the stability of this electrode/ABL interface. The first realized solar devices containing these organometallic polymers as ABL have shown wettability (respect to the active layer used) and resistivity problems, leading to poor $J_{sc}$, FF and $V_{oc}$. These results are mainly due to the low hole mobility measured for the electropolymerized thin films and to the still non-

optimized active layer film formation above these thin films, an aspect on which further work is necessary.

In the second part on this thesis, an innovative way of enhancing solar cell absorption is described. Indeed, the possibility of exciting plasmonic responses in a multilayers hyperbolic metamaterial (HMM) can offer the possibility of engineering the absorption band of the resulting structure to achieve the desired absorption performances, over a broad wavelength range and, above all, in a spectral region where organic materials usually cannot absorb the solar radiation. The HMM structure proposed here consists in BHJ/Al alternating layers of sub-wavelength dimensions, characterized by an enhanced absorption from the visible to the near-IR (900 nm) spectral range. The beneficial contribution of these plasmonic thin layers has been evident even with a single Al/BHJ hyperbolic bilayer, for which a complete optical (ellipsometry) characterization was carried out. This one-hyperbolic-bilayer Al/BHJ solar cell has shown enhanced power conversion performances with respect to the control devices, obtained with equivalent thickness for the BHJ layer but with a “bulk” thickness for the aluminum electrode (around 200 nm, for which plasmonic effects are negligible). $V_{oc}$ and FF, rather than $J_{sc}$, have shown the major increased values, contributing to the enhanced device efficiency. Other experimental work is in progress, with the aim to better understand the phenomena behind this enhanced power conversion efficiency. Measurements of EQE and acquisition of the J-V curves at several angles of incidence of light will be necessary. Preliminary optical results based on experimental and simulated data on the two-bilayer system have shown that this structure behaves as a Type-II HMM (from 500 nm to 900 nm) and confirmed the high absorption of the designed HMM. These results are very encouraging towards the aim of obtaining an HMM-solar device. Future work should be focused on the electrical characterization of this multilayers arrangement, to investigate the charge transport mechanism.

While working in the photovoltaic applications of HMMs, a series of experimental observations were performed that offered the opportunity to investigate, as side projects, several interesting phenomena. The first one regards the possibility to excite Bulk Plasmon Polariton modes in Ag/BHJ HMMs. These particular modes, first observed by Ferrell and Berreman, from whom they are named, support a very high absorption resonance. The presence of this absorption in the constructed HMM was verified and further studies are

being carried out to probe the possibility to use this absorption for power conversion enhancement in solar cell applications. The second one, instead, regards the possibility to further increase the tunability of a HMM using a specifically conceived dielectric layer based on an unsintered, sol-gel $TiO_2$ matrix doped with poly(vinylpyrrolidone) and a dye. The possibility of achieving a thermal control over the physical and optical properties of such a material opened the opportunity of a thermal tuning of the effective medium properties of the corresponding Ag/TPD HMM, paving the way for several practical application.

In conclusion, in this thesis two possible strategies for improving OSC efficiency, based on two critical aspects of a solar cell, are proposed. The first one involves the use of novel photoconductive material (whose conductivity improves under light exposure) coupled with a smart deposition technique (that enhances the stability of ITO/ABL interface). The latter is based on a HMM-solar cell architecture engineered to enhance the performances of OSCs, increasing the device absorption. The results presented here, even though in some cases not final, represent a sound basis for future developments.